

**Fabrication, Characterization and Cellular Interactions of Keratin
Nanomaterial Coatings for Implantable Percutaneous Prosthetics**

Alexis Raven Trent

Dissertation submitted to the faculty of the Virginia Polytechnic Institute
and State University in partial fulfillment of the requirements for the degree
of

Doctor of Philosophy

In

Materials Science and Engineering

Mark E. Van Dyke, Chair

Earl J. Foster

Aaron S. Goldstein

Abby R. Whittington

March 14, 2018
Blacksburg, Virginia

Keywords: Biomimetic interface, medical device, protein surface
modification

Fabrication, Characterization and Cellular Interactions of Keratin Nanomaterial Coatings for Implantable Percutaneous Prosthetics

Alexis R. Trent

Abstract

This work explores the feasibility of using keratin nanomaterials (KN) as a biomimetic interface for percutaneous prosthetics. Percutaneous implants suffer from complications due to the foreign body response. This reaction can create implant failure through epithelial down-growth, cell necrosis, infection, or mechanical tearing. These failure mechanisms have created the necessity for surface modifications on percutaneous implants so that stronger, longer-lasting connections to the skin can be realized. In these studies, we investigate KN as a surface coating on titanium substrates to simulate a bone-anchored, percutaneous prosthetic attachment device.

In aim 1, we use silane coupling chemistry to facilitate the attachment of KN to titanium in order to create a stable coating. This was further examined using surface characterization techniques such as atomic force microscopy (AFM), x-ray photoelectron spectroscopy (XPS), water contact angle, and time-of-flight secondary ion mass spectroscopy (ToF SIMS). The results suggested that homogenous, uniform KN coatings on titanium were produced. Cell adhesion assays were also completed, where focal adhesion complexes were identified on these substrates. Degradation assays were also completed in order to observe the mechanical and biochemical integrity of the coatings in simulated in vivo conditions.

In aim 2, recombinant human keratins (rhK) were created and subsequently used to form dimers similar to the KN confirmed by size exclusion chromatography in aim 1. Both, rhK and KN, were then used to make similar keratin coatings. A study comparing the keratin extracted under reductive conditions from human hair fibers and the rhK was conducted. Coating topographies, cell adhesion immunochemistry, and phenotypic expression of attached cells were compared on these substrates. The results confirmed rhK is able to create a coating similar to that of extracted KN, but with rhK possibly having improved structure in terms of a homogeneous material composition.

Aim 3 investigated the mechanical strength of integrin-mediated attachment to extracted KN and rhK substrates. Two cell types were examined on the substrates, keratinocytes and dermal fibroblasts. The data suggests that cells on KN and rhK substrates had similar adhesion strength, but rhK offers the advantage of modifications at the amino acid level that may further improve cell adherence and long-term stability.

Lastly, the same silane-KN coating methodology was used on a polymeric substrates to demonstrate the feasibility of using a keratin biomimetic coating on other medical devices made from or coated with polymeric materials, such as neural electrodes, continuous glucose monitors, and catheters. Future investigation of KN coatings on polymers will need to undergo cellular adhesion studies.

Overall, this work demonstrated that KN and rhK can create coatings for percutaneous and other medical devices. The studies for percutaneous implant coatings have created the

foundation for recently undertaken animal studies, and for future investigations that may lead to the clinical translation of novel prosthetic attachment technologies.

Fabrication, Characterization and Cellular Interactions of Keratin Nanomaterial Coatings for Implantable Percutaneous Prosthetics

Alexis R. Trent

General Audience Abstract

Implantable medical devices face numerous complications when interfacing with soft tissue, and are plagued by negative responses from host tissue. One such class devices is percutaneous osseointegrated prosthetics (POP). POP consist of a bone anchored titanium post that extrudes through the skin and attaches to an external prosthetic. Compared to the traditional socket interface, POPs offer better stability, limb functionality, and osseoperception for both upper and lower prosthetic limbs. Although the POP surgery technique is well established, the main disadvantage to this technology remains the titanium (Ti) - skin interface. Some of the complications that can arise include epithelial downgrowth, mechanical tearing, and infection. Various types of coatings, surface structure, and antibiotic release technologies have been used to coat Ti in an effort to mitigate POP's associated obstacles, but these methods have failed to translate into published clinical studies and mainstream medical use.

One potential solution may be to mimic an interface already found in the human body, the fingernail-skin interface, which is infection-free and mechanically stable. The same keratins that make up the cortex of human hair fibers are found in the fingernail. These cortical human hair keratins can be extracted and purified, and fingernail-specific dimeric complexes coated onto Ti surfaces using silane coupling chemistry. Keratin has been used

in other studies for its cell adhesion and differentiation properties, and it has been suggested that the Leu-Asp-Val (LDV) amino acid motif is the primary site responsible for cellular attachment.

In the present work, keratins extracted from human hair fibers and recombinant keratin nanomaterials (KN) were used to create biomimetic coatings on silanized Ti surfaces. These coatings were characterized and investigated for surface topography, elemental composition, cell adhesion motifs, and cell adhesion. Both keratin substrates showed the ability to create uniform coatings that retain a protein conformation that exhibits cell adhesion motifs. The coatings exhibit the ability to support cell adhesion of both epithelial and connective tissue cells. Application of fluid shear stress was used to test the mechanical adhesion strength of cells on keratin coatings. The structure, biochemical stability and sustained cellular adhesion of these coatings support keratin's capacity to provide a stable interface between POPs and skin. Side-by-side studies of extracted and recombinant keratins reveals that the recombinant form of these materials may provide distinct advantages for their use in POP devices.

Overall, this study confirmed that a uniform, silane-coupled keratin coating was feasible. We demonstrated the substrates contain a biological function in terms of cellular adhesion and phenotypic changes in skin-relevant cells. These results support the biomimetic function of keratin on silanized Ti, which may provide a suitable coating to translate percutaneous medical device coating applications toward clinical use.

Dedication

To anyone who has ever felt or been told they do not fit the engineering mold, but proved to themselves and others they belonged, and to the encouraging support teams that helped them achieve their goals.

Acknowledgements

When I began graduate school, I knew it would be a trying time, but I was not expecting all the difficult times that I would endure. I was naïve but ready to tackle this degree which carried so much prestige. My first semester, I knew I had bit off more than I could chew, but the colleagues, faculty, and staff surrounding me always provided me with an encouraging platform. After my first meeting with my advisor, Dr. Mark Van Dyke, I knew I wanted to be in his lab, but completing my lab rotations created a further appreciation for the type of advisor he is. I have learned so much from him in life and academically. His emphasis on being thorough, possessing integrity, and being tough but fair has laid the groundwork for how I want to present myself professionally. Van Dyke's quirky anecdotes and home improvements stories reminded me of my parents in California creating a home away from home. I thank him for taking a chance on me, encouraging me to continue when I had hit various roadblocks in my tenure, and being my guidance through this degree. I would also like to thank my committee members Dr. Johan Foster, Dr. Aaron Goldstein, and Dr. Abby Whittington for helping me through this process and asking me insightful questions, which truly made me think and progressed my academic success.

To Dr. Ed Smith, you stuck with our Initiative for Maximizing Student Development (IMSD) cohort even though we complained every class, had our own academic tribulation, and downright attitudes with you, you managed to stick it out and always be our advocate. I did not always agree or listen, but I always appreciated your effort, tenacity, and being

the push we did not want but needed, in order to keep going. Also, thanks for always finding me money! –From, the original rascal.

Dr. Jack Lesko and Dr. Catherine Amelink, New Horizons was one of my first communities and was needed in my early years. The one-one meetings with both of you was vital in navigating graduate school. Whenever I asked for something or needed support, you never failed me and I thank you both for that.

TeAirra Brown, to my one of my first friends here, to my Delta Sigma Theta soror, having you made the transition from A&T so much easier. We could be real and we had so much fun that first year, I am glad I went to that graduate school cookout when we first discovered we were going to be friends.

Jamelle Simmons, we have too many stories to write-down. You might be the best-worst influence I have had in graduate school. You are always unapologetically you. I will miss our Taphouse conversations and complaining sessions over drinks.

Michele Waters, to my fellow struggle life partner and kooky, dancing, singing labmate. We had fun together, stressed out together, and have gotten to our wits end, but we did it all together! Thanks for being there as a springboard for my craziness and egging me on.

Marc Thompson, Nils Potter, Undergrad Aaron Guiffe, and Scott Saverot, I feel you guys held the lab together, doing everything Michele and I were always too tired or just were

too lazy to do. There have been some fun times, between long conversations during rat surgeries to lab outings. I know you guys will hold down the lab in the coming years.

Kyle Brown, Kegan Sowers, Michelle Ton, Kevin Tong- thank you for helping me along the way and along me to guide you through your undergraduate research journey.

Jasmine Hayes, to my craziest friend at Virginia Tech, I have so many memories with you and stories to tell, I will leave it at that.

Marissa Lang, to all the Lefty's cheesecake we consumed and bottles of wine, I thank you for your kindness and being a listening ear. I cannot wait to see us in a couple years, living our best lives.

Materials Science and Engineering (MSE-Adowa, Andre, Rob, and Coffee and Donuts), this department always was welcoming to me and Adowa, Andre, and Rob always made sure I was prepared to navigate my next academic step in my graduate career.

Justine Riddick, my right hand during this process, the woman who encourages me and listens to all my woes in every aspect of my life. To the late nights of video chats while doing work together to helping me stay sane, I thank you.

To friends and family near and far, I wish I could have seen and talked to you more, but thanks for being understanding and loving during this process.

To my parents Albert and Regina Trent, you have always been supportive of letting me do what I think is best for me, and I truly appreciate that. I hope I did not scare you with my phone calls (and sometimes tears) through this process, just know your voices provided reassurance that whatever I was going through was temporary.

Aaron P. White, to my love and future husband, who has been my rock during this experience. You took the bulk of the emotional rollercoaster I was on and knew every trial, tribulation and triumph I went through. When I felt lost and stressed, you would always lead me back on track. You even made the extra weight of living apart seem easy and worked so hard to make me feel supported. Thank you so much for everything you have poured into me over this experience and the last seven years. I love you.

Table of Contents

Abstract.....	ii
General Audience Abstract.....	v
Dedication	vii
Acknowledgements	viii
Table of Contents	xii
List of Figures.....	xv
List of Tables	xviii
Chapter 1. Introduction into Soft Tissue-Medical Device Interactions	1
1.1 Introduction	2
1.2 Integrin-mediated Extracellular Matrix Adhesion	5
1.3 Focal Adhesion Complex Formation	7
1.4 Implantable Biomaterials Interaction with Surrounding Tissue.....	8
1.5 Soft Tissue and Central Nervous System Device Interfaces.....	12
1.6 Surface Modifications to Improve Biocompatibility	14
1.7 Keratin Biomaterials	16
1.8 Conclusion	17
1.9 References	19
Chapter 2. Development and Characterization of a Biomimetic Coating for Percutaneous Devices.....	24
2.1 Abstract	25
2.2 Introduction	26
2.3 Methods	29
2.3.1 Keratin Extraction	29
2.3.2 Automated Western Blot System (Capillary Electrophoresis Immunoassay)	30
2.3.3 Size Exclusion Chromatography (SEC).....	30
2.3.4 Silane Coupling and Protein Deposition	31
2.3.5 Atomic Force Microscopy (AFM)	32
2.3.6 X-ray Photon Spectroscopy (XPS)	32
2.3.7 Contact Angle	32
2.3.8 Enzyme Degradation.....	33
2.3.9 Adhesion Motif Detection.....	33
2.3.10 Cell culture.....	33
2.3.11 Focal Adhesion Immunocytochemistry	34
2.3.12 Detection of Smooth Muscle Actin (SMA) in Fibroblasts	34
2.3.13 Detection of Involucrin in HaCaTs.....	35
2.3.14 Statistics	35
2.4 Results.....	36
2.4.1 Western Blot	36
2.4.2 XPS	37
2.4.3 AFM	38
2.4.4 Contact Angle	39
2.4.5 Enzyme Degradation.....	40
2.4.6 Adhesion Motif Detection.....	42

2.4.7	Focal Adhesion Immunocytochemistry	45
2.4.8	SMA and Involucrin Analysis.....	49
2.5	Discussion	49
2.6	Conclusions	53
2.7	Acknowledgements	53
2.8	References	54
Chapter 3. A Comparative Study of Recombinant and Extracted Human Hair		
Keratins		58
3.1	Abstract	59
3.2	Introduction	60
3.3	Materials and Methods	63
3.3.1	Gene Design and Cloning of Recombinant K31 and K81	63
3.3.2	Protein Expression and Purification of Recombinant Proteins	63
3.3.3	Keratin Gel Electrophoresis and Western Blot	64
3.3.4	Dialysis.....	65
3.3.5	Extraction of Natural Keratin Proteins.....	65
3.3.6	Size Exclusion Chromatography.....	66
3.3.7	Dynamic light scattering	67
3.3.8	Transmission Electron Microscopy	67
3.3.9	Silane Coupling and Protein Deposition	67
3.3.10	Time of Flight Secondary Ion Mass Spectrometry (ToF-SIMS).....	68
3.3.11	Atomic Force Microscopy (AFM).....	69
3.3.12	Cellular Motif Identification.....	69
3.3.13	Cell Static Adhesion Immunocytochemistry	69
3.3.14	Involucrin Detection	70
3.3.15	Smooth Muscle Actin Detection.....	71
3.3.16	Statistics.....	71
3.4	Results and Discussion	72
3.4.1	Keratin SDS-PAGE and Western Blot.....	72
3.4.2	SEC and DLS	74
3.4.3	TEM	79
3.4.4	ToF SIMS.....	80
3.4.5	AFM	82
3.4.6	Cellular Motif Identification	83
3.4.7	Cellular Adhesion Immunocytochemistry	85
3.4.8	Involucrin and Smooth Muscle Actin Detection.....	87
3.5	Conclusions	89
3.6	Acknowledgements	90
3.7	References	91
3.8	Supplementary Figures	97
Chapter 4. Application of Fluid Shear Stress on Skin Cells to Characterize		
Cellular Attachment on Keratin Nanomaterial Substrates		
4.1	Abstract	100
4.2	Introduction	101
4.3	Methods	103
4.3.1	Keratin Extraction	103
4.3.2	Silane Coupling and Protein Deposition	104
4.3.3	Cell culture	104

4.3.4	Shear Assay and Focal Adhesion Immunocytochemistry.....	105
4.3.5	Automated Western Blot System (Capillary Electrophoresis Immunoassay)	106
4.3.6	Statistics	106
4.4	Results and Discussion	106
4.4.1	Shear Assay and Focal Adhesion Immunocytochemistry.....	106
4.4.1.1	Fibroblasts.....	106
4.4.1.2	HaCaT	112
4.4.2	Modes of Failure	117
4.4.3	Automated Western Blot System (Capillary Electrophoresis Immunoassay)	119
4.5	Conclusions	120
4.6	Acknowledgements	121
4.7	References	122
Chapter 5.	Investigation of Keratin Nanomaterials as Coatings for Polymeric Medical Device Applications.....	125
5.1	Abstract	126
5.2	Introduction	127
5.3	Methods	128
5.3.1	Keratin Extraction	128
5.3.2	Protein Deposition.....	129
5.3.3	Atomic Force Microscope.....	129
5.3.4	Statistics	129
5.4	Results and Discussion	130
5.5	Conclusion	132
5.6	Acknowledgments.....	132
5.7	References	133
Chapter 6.	Conclusions, Limitations, and Future Work.....	135
6.1	Overall Project Conclusion.....	136
6.2	Characterization of Extracted Keratin Nanomaterials Biomimetic Coating	136
6.3	Exploration of Recombinant Keratin Nanomaterials Biomimetic Coating.....	137
6.4	Importance of Research and Future Work.....	137

List of Figures

Figure 1.1. Examples of soft tissue-medical device interactions. A) Percutaneous Osseointegrated Prosthetics (POPs), B) Continuous Glucose Monitoring, and C) Neural Prosthetics.	4
Figure 1.2. Integrin Activation. Adapted from Srichai et al. ²⁶	7
Figure 1.3. Failure Modes of Percutaneous Devices. (A) Marsupialization (B) Permigration (C) Avulsion (D) Infection (E) Desired Outcome. This figure was adapted from Von Recum ⁴⁰	11
Figure 1.4. Glial Encapsulation schematic adapted by Grill et al. ⁴⁸	13
Figure 2.1. Western Blot and SEC. (A) Graphical representation of the electrophoresis results produced by the WES system (left) and SEC (right). Keratose has a peak approximately at 20 kDa, with a continued plateau until 150 kDa and kerateine has a gradual increase starting at 50kDa that drops off at 175kDa. These data are indicative of a high molecular weight keratin dimer at approximately 112kDa, as well as aggregates of dimers in the case of KTN. KTN contains a higher ratio of keratin nanomaterial (dimerized keratin) to protein fragments than KOS. (B) Based on the retention time for BSA (molecular weight of 66.5 kDa), KOS displays a peak in the 40-50 kDa range, whereas KTN ranges between 65-100kDa with a small shoulder between 40-50kDa.	36
Figure 2.2. XPS. Elemental percentages from XPS analysis of substrates for nitrogen (A) and titanium (B). For all graphs, significance is only shown against pure Ti where * signifies $p \leq 0.05$, ** signifies $p \leq 0.01$, and *** signifies $p \leq 0.001$	37
Figure 2.3. AFM. A) Rendered images of substrate topography. B) Graphical representations of RMS from AFM data. C) Graphical representation of the contact angle and significance is only shown against pTi, where * signifies $p \leq 0.05$, ** signifies $p \leq 0.01$, and *** signifies $p \leq 0.001$	38
Figure 2.4. Enzyme Degradation Assay. Percent of nitrogen (A) and titanium (B) by XPS on test substrates treated with enzyme solutions for up to 16 weeks.	40
Figure 2.5. Motif Sites. (A) Images of antibody-conjugated fluorophores attached to test substrates, binary images were created in Image J for better visualization and the scale bar represents 50 μ m. (B) Graphical representation of the number of motif sites.	43
Figure 2.6. Fibroblast Focal Adhesion and SMA Immunocytochemistry. (A) Red (Actin), green (vinculin), blue (nucleus) are represented for fibroblast focal adhesion on the listed substrates. SMA antibody is represented with green and the nucleus is represented with blue. (B) Graphical representation of actin and vinculin at 3 hours incubation as stained area/cell. Scale bars represent 50 μ m.	46
Figure 2.7. HaCaT Focal Adhesions and Involucrin Immunocytochemistry. (A) Red (Actin), green (vinculin), and blue (nucleus) are shown to identify HaCaT adhesion on the listed substrates. Involucrin antibody is represented with green and the nucleus is represented with blue in the far right column. (B) Graphical representation of actin and vinculin at 3 hours of incubation as stained area/cell. Scale bars represent 50 μ m.	48

Figure 2.8. SMA and Involucrin. (A) A graphical representation of area/cell for SMA fluorescence. (B) A graphical representation of area/cell for SMA fluorescent.....	49
Figure 3.1. Comparison of purified recombinant and extracted keratins a) picture of purified recombinant (1) and extracted (2) solutions b) SDS-PAGE fractions: M-marker, 1-rhK31, 2-rhK81, 3-Extracted KTN c) Western blot with K31 antibody and d) Western blot with K81 antibody.....	73
Figure 3.2. Chromatogram of recombinant (blue) and extracted (black) keratin in 8 M urea obtained from SEC. Red numbers correspond to peak labels listed in table 1.	77
Figure 3.3. DLS from a) recombinant keratin urea series b) extracted keratin urea series and c) recombinant (solid line) and extracted (dotted line) keratin samples in 0 M urea.....	78
Figure 3.4. TEM images of recombinant (a-b) and extracted (c-d) keratin proteins. Scale bars are (a) 500 nm and (b-d) 300 nm. All images are stained with 2% uranyl acetate.	80
Figure 3.5. A) Keratin substrates were independently ranked from highest intensity '1' to lowest intensity '7' for each amino acid listed in 3.5B. Rankings for each substrate were then accumulated. If a substrate has 15 amino acids with the rank '1' the quantity will be 15. Some amino acids in the ToF-SIMS have multiple positive fragments, each fragments was used. A large '1' quantity signifies the highest intensity for relevant amino acids. B) Amino acids chosen to be analyzed are represented in this table, to be considered the amino acid mole percent for either K31 or K81 must exceed 6%.	80
Figure 3.6. A) Rendered images of substrates examined by AFM. B) RMS roughness values of substrates. Significance shown is iKTN against all remaining experimental groups, there is additional significance between iRhK and Au. Significance is identified by * for $p \leq 0.05$, ** for $p \leq 0.01$, and *** for $p \leq 0.001$. *** ≤ 0.001	83
Figure 3.7. A) Cellular motifs identified using fluorescent spheres, binary images were created in Image J for better visualization and the scale bar represents 50 μ m. B) Number of cellular motifs on substrates.	84
Figure 3.8. A) HaCaT cells focal adhesions represented by red (Actin), green (vinculin), blue (nucleus). B) Area of Actin staining quantified by ImageJ (n=5). C) Circularity observed by Image J is graphical represented (n=5). Significance is identified by * for $p \leq 0.05$, ** for $p \leq 0.01$, and *** for $p \leq 0.001$. *** ≤ 0.001 . Scale bars represent 50 μ m.	86
Figure 3.9. A) Fibroblasts focal adhesions represented by red (Actin), green (vinculin), blue (nucleus). B) Area of Actin staining quantified by ImageJ. C) Circularity observed by Image J is graphical represented. Circularity ranges from zero to one, where one indicates a perfect circle. Significance is identified by * for $p \leq 0.05$, ** for $p \leq 0.01$, and *** for $p \leq 0.001$. *** ≤ 0.001 . Scale bars represent 50 μ m.....	87
Figure 3.10. A) Involucrin. A digitized Western blot lane view from the ProteinSimple Wes instrument for involucrin including Ca 2+ induced HaCaT cells, which represent the positive control. B) Smooth Muscle Actin. Digitized Western blot for smooth muscle actin in fibroblasts.....	88
Figure 3.11 Average distance between cellular motifs.....	97

Figure 4.1. Representative images of fibroblasts at 6 hours. A) Static conditions represent 0 dyne/cm ² , while dynamic represents 10 dynes/cm ² . Focal adhesions are identified by red (actin), green (vinculin), and blue (nucleus). B) Graph of the area of actin per cell. The significance is shown by *≤ 0.05 and **≤0.01 within substrates and between substrates under the same shear conditions. Scale bars represent 50 μm.	107
Figure 4.2. Representative images of fibroblasts at 24 hours. A) Static (S) conditions represent 0 dyne/cm ² , while dynamic (D) represents 10 dynes/cm ² . Focal adhesions are identified by red (actin), green (vinculin), and blue (nucleus). B) Graph of the area of actin per cell. No significance identified. Scale bars represent 50 μm.	109
Figure 4.3. Representative images of fibroblasts at 72 hours. A) Static (S) conditions represent 0 dyne/cm ² , while dynamic (D) represents 10 dynes/cm ² . Focal adhesions are identified by red (actin), green (vinculin), and blue (nucleus). B) Graph of the area of actin per cell. No significance identified. Scale bars represent 50 μm.	111
Figure 4.4. Representative images of HaCaT cells at 6 hours. A) Static (S) conditions represent 0 dyne/cm ² , while dynamic (D) represents 10 dynes/cm ² . Focal adhesions are identified by red (actin), green (vinculin), and blue (nucleus). B) Graph of the area of actin per cell. No significance identified. Scale bars represent 50 μm.	112
Figure 4.5. Representative images of HaCaT cells at 24 hours. A) Static (S) conditions represent 0 dyne/cm ² , while dynamic (D) represents 10 dynes/cm ² . Focal adhesions are identified by red (actin), green (vinculin), and blue (nucleus). B) Graph of the area of actin per cell. The significance is shown by *≤ 0.05 and **≤0.01 within substrates and between substrates under the same shear conditions. Scale bars represent 50 μm.	114
Figure 4.6. Representative images of HaCaT cells at 72 hours. A) Static (S) conditions represent 0 dyne/cm ² , while dynamic (D) represents 10 dynes/cm ² . Focal adhesions are identified by red (actin), green (vinculin), and blue (nucleus). B) Graph of the area of actin per cell. No significance identified. Scale bars represent 50 μm.	115
Figure 4.7. Modes of Failure after shear exposure. Modes of Failure under dynamic conditions (10 dynes/cm ²) for HaCaT and fibroblast cells. Scale bars represent 50 μm.	117
Figure 4.8. Western Blot of K6, K10, K16, and B-Actin. HaCaT cells were seeded for 72 hours and exposed to static (0 dynes/cm ²) and dynamic (10 dynes/cm ²), cells were probed for K6, K10, K16, and B-Actin using the Wes TM Western blot instrument.	119
Figure 5.1 The topography of KN on parylene C substrates.	131
Figure 5.2. Graphical representation of KN RMS	131

List of Tables

Table 2.1: Significance of RMS shown in the graph in Figure 2.3B. Significance notation is as follows * signifies $p \leq 0.05$, ** signifies $p \leq 0.01$, *** signifies $p \leq 0.001$, and ns signifies $p \geq 0.05$.	39
Table 2.2. Degradation Regression for Nitrogen.	41
Table 2.3. Degradation Regression for Titanium.	41
Table 2.4: Significance of the number of motif sites. Significance notation is as follows * signifies $p \leq 0.05$, ** signifies $p \leq 0.01$, *** signifies $p \leq 0.001$, and ns signifies $p \geq 0.05$.	43
Table 2.5: Significance of the median distance of motif sites. Significance notation is as follows * signifies $p \leq 0.05$, ** signifies $p \leq 0.01$, *** signifies $p \leq 0.001$, and ns signifies $p \geq 0.05$.	44
Table 3.1. Estimated oligomeric states from SEC analysis.	75
Table 3.2. Hydrodynamic radius of species present in solution at decreasing urea concentrations.	78
Table S3.3. Significance for the averages of motif distance. The * signifies $p \leq 0.05$, ** signifies $p \leq 0.01$, *** signifies $p \leq 0.001$, and ns signifies $p \geq 0.05$.	97
Table S3.4. Significance for the averages of motif sites. The * signifies $p \leq 0.05$, ** signifies $p \leq 0.01$, *** signifies $p \leq 0.001$, and ns signifies $p \geq 0.05$.	98

Chapter 1. Introduction into Soft Tissue-Medical Device Interactions

Alexis R. Trent

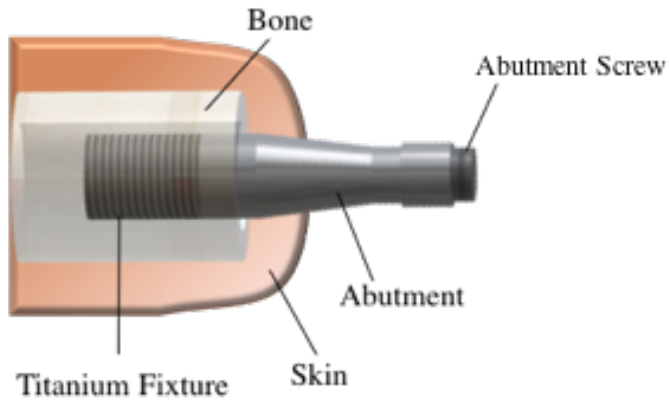
1.1 Introduction

Generating a cohesive connection between native tissue and a foreign medical device is a large area of focus in biomaterials. Mimicking tissues' biological makeup, mechanical strength, and structural components are primary approaches for biomaterials development and is the ultimate goal of biomimetic materials. However, it may not be necessary to compose an entire device of the biomimetic material as only the interface will contact the biologic environment. Organic and synthetic materials alike are used to create surfaces and interfaces that elicit limited foreign body response. The foreign body response is characterized by the sequenced development of acute inflammation, chronic inflammation, granulation tissue formation, and fibrous encapsulation^{1,2}. Percutaneous implants are a specific class of medical devices and pass through the skin, extending both outward away from the skin as well as inward, toward and in intimate contact with underlying, sometimes deeply underlying, tissues. Examples of such devices include catheters, sensors, drain tubes, and prosthetics. The body's adverse reaction to these devices can obstruct their intended function resulting in device failure, or become infected because they offer a bypass of the protective layer of the skin to adventitious bacteria. For this reason, potential improvements are constantly being investigated to optimize biocompatibility at the material-tissue interface.

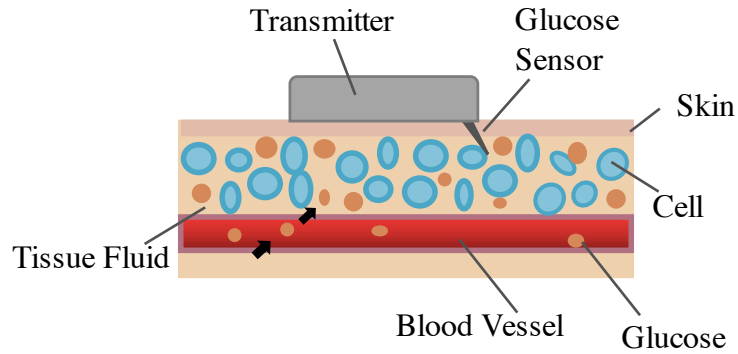
Surface modifications to implants can be accomplished through a variety of means, such as protein and adhesive peptide coatings³⁻⁷, changes in topography^{8,9}, mechanical stiffness¹⁰, and the inclusion of antibacterial drug components^{11,12}. These methods have been investigated to provide improved tissue-material interactions and induce intentional biologic and morphology changes in cells within the surrounding tissue. Implants that are designed for use in various parts of the human body and different tissues such as bone, cartilage, epithelial, and central nervous

tissue, have adopted some of these approaches with varying degrees of success. Long term surgical implantation of dental implants, vascular stents, and osseointegrated devices have already been well established, but soft and central nervous tissue still present difficulties that can create complications in practice, and prevent progression of these technologies toward the clinic.

(A) Percutaneous Osseointegrated Prosthetics



(B) Continuous Glucose Monitoring



(C) Neural Prosthetics

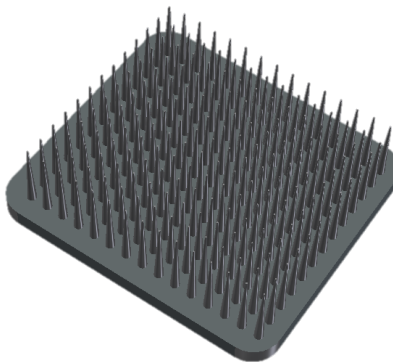


Figure 1.1. Examples of soft tissue-medical device interactions. A) Percutaneous Osseointegrated Prosthetics (POPs), B) Continuous Glucose Monitoring, and C) Neural Prosthetics.

1.2 Integrin-mediated Extracellular Matrix Adhesion

Understanding primary factors of soft tissue enables researchers to create suitable medical devices for particular applications. The extracellular matrix (ECM) is a primary component of organs and tissues to which cells maintain mechanically stable connections. ECM is an acellular, fibrous material that contains an essential structural framework as well as biological factors that contribute to cell adhesion, differentiation, and homeostasis^{13,14}. ECM varies in composition and mechanical characteristics depending on where it resides in the body. ECM's main components are glycosaminoglycans (GAG), proteoglycans, collagens, elastin, and fibronectin¹³. GAGs are linear polysaccharides containing repeating disaccharides that provide turgor to ECM due to its hydrophilic nature^{13,15}. Proteoglycans are molecules with GAG covalently bound to a core protein and provide a gel-like consistency but maintain ion diffusivity¹⁶. Proteoglycans basic structure allow for a diverse range of proteins and GAGs to attach to each other. Collagens, fibronectin, elastin, laminin, and other similar proteins are also found in ECM and contribute to tensile strength, cellular attachment, and its fibrous structure¹⁴⁻¹⁸.

ECM contains amino acid sequences or short peptides that are specific to cells' transmembrane receptors (e.g. integrins) and act as ligands. These "motifs" in collagen (e.g. DGEA, GFOGER), elastin (e.g. VAPG), fibronectin (e.g. RGD, KQAGDV, REDV, LDV, and PHSRN), laminin (e.g. IKLLI, LRE, LRGDN, PDGSR, IKVAV, LGTIPG, and YIGSR), and keratin (e.g. LDV)¹⁹⁻²² allow for cell-ECM mechanical attachment and signal propagation from outside to inside the cell. This relationship is sometimes what biomaterials try to emulate by incorporating native proteins or adhesion motifs within their structure, and in some cases are designed to modulate the wound healing process and tissue reconstruction.

Integrins and syndecans are transmembrane proteins that provide a modality for cells to adhere to ECM. Although cells primarily adhere through integrin mediated attachments, syndecans are transmembrane proteoglycans that attach to ligands and growth factors through GAG chains, and are helpful when ligands are sparse and distant from the membrane due to inactivation²³. Integrins are transmembrane heterodimer proteins that are comprised of α and β subunits and bind to specific ECM cellular motifs^{24,25}. There are at least 24 unique integrins formed by 18 α and 8 β subunits. Each integrin generally has a short cytoplasmic tail, a transmembrane domain, and an exterior domain that links to the ligand presented by the ECM. Integrin-ligand binding is postulated to occur through at least two mechanisms. In the first case, the α subunit contains approximately a 200 long amino acid section, otherwise classified as the I-domain. This I-domain contains a metal-dependent site that bind to cations. Integrin activation occurs through ligand binding, which alters the coordination of the metal ion, causing the I-domain to transition from a closed, dormant state to an open, activated state, leading to further integrin activation. In the second case, the α subunit does not possess the I-domain, but the β subunit supports binding by possesses a domain similar in composition and metal-ion dependence to the I-domain²⁶. This allows access for bidirectional communication that can regulate focal adhesion formation, cell morphology, migration, and differentiation²⁶.

Integrin activation or inside-out signaling occurs when the cell induces the integrin to transition from an inactivated bend state to a straightened activated state. The proteins talin and kindlin are an integral part in integrin activation. Talin is an actin-binding protein that binds to the β subunit of an integrin receptor. Ezrin, radixin, and moesin also crosslink actin to the plasma membrane via FERM domains that attach to the cytoplasmic tail of the integrin²⁷. Kindlin is another protein that contains the FERM domain and jointly with talin, regulates integrin affinity

^{26,27}. Outside-in signaling occurs via ligands binding to integrin extracellular domains, which bind to adapter proteins within the focal adhesion complex, and further propagate biochemical signals into and throughout the cell. Biomaterials have tried to exploit outside-in signaling by creating a surface on devices to which cells will form focal adhesions.

1.3 Focal Adhesion Complex Formation

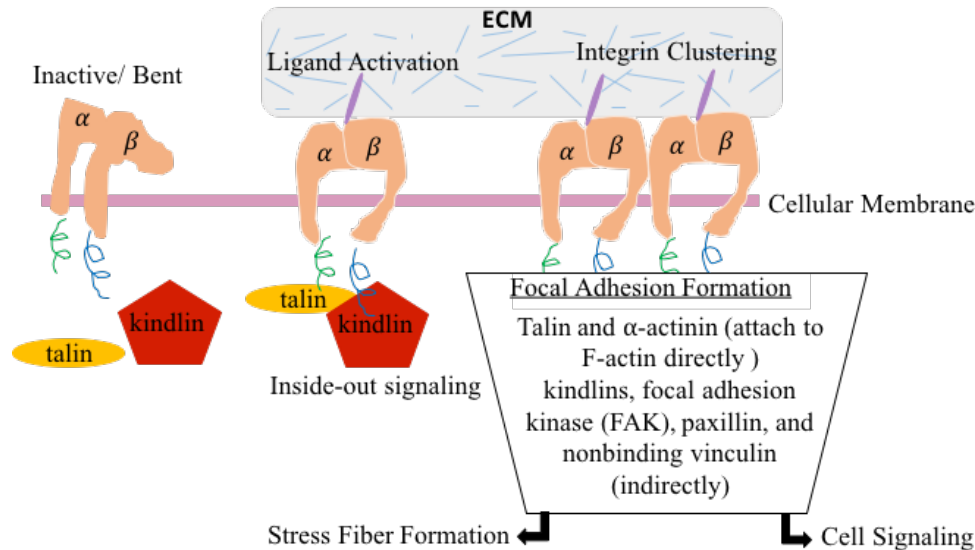


Figure 1.2. Integrin Activation. Adapted from Srichai et al.²⁶.

The formation of focal adhesion complexes is heavily reliant on integrin-ligand connection, integrin activation, and specifically outside-in signaling. Integrins attach to ligands in ECM which lead to integrin clustering as well as stress fiber and actin filament reorganization. This progression is dynamic and iterative, consisting of a multitude of proteins. Proteins bound to integrins can attach to F-actin directly (talin and α -actinin) and indirectly (kindlins, focal adhesion kinase (FAK), paxillin, and nonbinding vinculin) to assist in filament and focal adhesion maturation²⁶. Integrins activate FAK, which autophosphorylates Tyrosine (Tyr) to create a binding site for Src, this can offset other activations leading to Rho GTPases pathways²⁸. Through outside-

in signaling Rho GTPases molecules such as Rho, Rac, and cell division cycle 42 (CDC42) regulate cytoskeletal and adhesion assembly. RhoA's initiation promotes myosin II activation further by initiating focal adhesion maturation and stability through tension and protein conformation remodeling. Rac signaling is associated with the leading edge lamellipodia initiation, while CDC42 activates filopodia^{29,30}.

Rac and CDC42 of these molecules induces protrusions through actin polymerization by starting the Arp2/3 complex²⁵. This process forms focal adhesion complexes, which provide robust and stable cell-substrate attachments. Beside biochemical cues, integrins act as mechanosensors for mechanotransduction in which cells experience mechanical stimuli that translates into biological cascades within the cell. This can include cell differentiation, morphology, motility, and overall cell behavior^{31,32}. For certain biomaterial applications, it is critical to create responses for cells through both mechanical and biological cues to induce the appropriate responses for the desired function.

1.4 Implantable Biomaterials Interaction with Surrounding Tissue

Implantable medical devices were established in 1958 with the implantation of the first pacemaker³³. Biocompatible materials have been used for artificial heart valves, vascular grafts, and orthopedic prostheses to name a few, all which have various material requirements³⁴. Polymers, metals, and ceramics have been explored as biomaterials. Design considerations for biomaterials include surface energy, surface topography, biological, chemical and mechanical gradients, material stiffness, toxicity, permeability, and degradation capabilities. Polymeric biomaterials are popular because of the ability to lower their surface energy and increase wettability with an oxygen plasma treatment, which has been shown to reduce bacterial adhesion and allow for specific protein attachment^{35,36}. Polymers are used for a range of devices such as

catheters, intraocular lenses, vascular grafts, heart valves, and soft tissue augmentation. Metals and alloys are used for orthopedic applications because of the capability to alter their mechanical qualities though fatigue resistance, tensile strength, corrosion resistance, flexibility, and ductility. Ceramics are characteristically used in joint replacements because of their hardness and wear resistance. To assist with binding tissues such as bone, hydroxyapatite, calcium phosphates and bioactive glasses have been used³⁷. When medical devices are implanted subcutaneously or percutaneously long-term, the body can respond adversely. Complications that occur in these types of tissue-material interactions include inflammation, infection, granulation tissue formation, encapsulation, and immunoreactivity. These adverse effects contribute to the foreign body response.

Medical device or biomaterial implantation begins the foreign body response. One of the first events that occurs in the process is protein from the surrounding extracellular space adsorbs to the implant surface, the rate and amount being dependent on the biomaterial surface chemistry. With biomaterials and medical devices that are in contact with blood, platelets and leukocytes adhere and begin a cascade of signaling to initiate clotting and inflammation. This newly adsorbed surface dictates the responses from foreign body-related cells such as monocytes, macrophages, and foreign body giant cells. The onset of inflammation is characterized by macrophage and monocyte recruitment to the injury site via chemokines and chemoattractants produced by platelets¹. Once present, macrophages recruit more cells to the wound site. Monocytes and macrophages express various integrins containing β_1 , β_2 , β_3 , namely $\alpha_4\beta_1$, $\alpha_5\beta_1$, $\alpha_6\beta_1$, which all attach to ECM proteins such as fibronectin and laminin where $\alpha_v\beta_3$ binds to the arginine-glycine-aspartic acid (RGD) motif³⁸. Macrophage intracellular signaling is modulated by integrin-mediated adhesion and is characterized by podosomes, which consist of an actin core surrounded

by critical focal adhesion proteins that manage actin polymerization³⁹. Once adhered, macrophages form cell-cell interactions to create foreign body giant cells. These cells respond to signaling pathways through ECM, but can also react due to the presence of cytokines. If the material does not contain cell adherent proteins, macrophages will undergo apoptosis and this pathway can assist to reduce persistent infections³⁹.

Without an appropriate biomaterial coating, this inflammatory response can continue in an iterative loop, leading to other complications affecting medical devices and implants. For percutaneous devices, the main modes of failure are epithelial downgrowth (e.g. marsupialization), permigration, which is the necrosis of cells within porous structures, infection, and avulsion (e.g. mechanical tearing)⁴⁰ (**Figure 1.3**). Fibrous encapsulation is formed by granulation tissue, which surrounds the device in fibrous tissue and scar¹. In normal soft tissues, the wound healing and inflammatory response leads to granulation tissue and reepithelialization or new tissue formation. For healthy tissue, fibrin or blood clot is formed by platelets and cytokines. Soon after, neutrophils and monocytes migrate to the wound area. Neutrophils are recruited to debride and rid the injury site of bacteria. These cells are then phagocytized by macrophages along with any other remaining bacterial organisms⁴¹. Fibroblasts and macrophages start to replace the fibrin clot and form new granulation tissue, which in skin serves as a substrate for keratinocytes. Keratinocytes migrate to the wound site and angiogenesis begins to provide vascularization. This granulation tissue forms a new substrate for the keratinocytes to migrate, mature, and differentiate on as they start the transformation to create the stratified layers of the skin⁴². Ultimately, inflammatory cells leave the site or undergo apoptosis while the wound becomes healed and remodeled with differentiated keratinocytes⁴³.

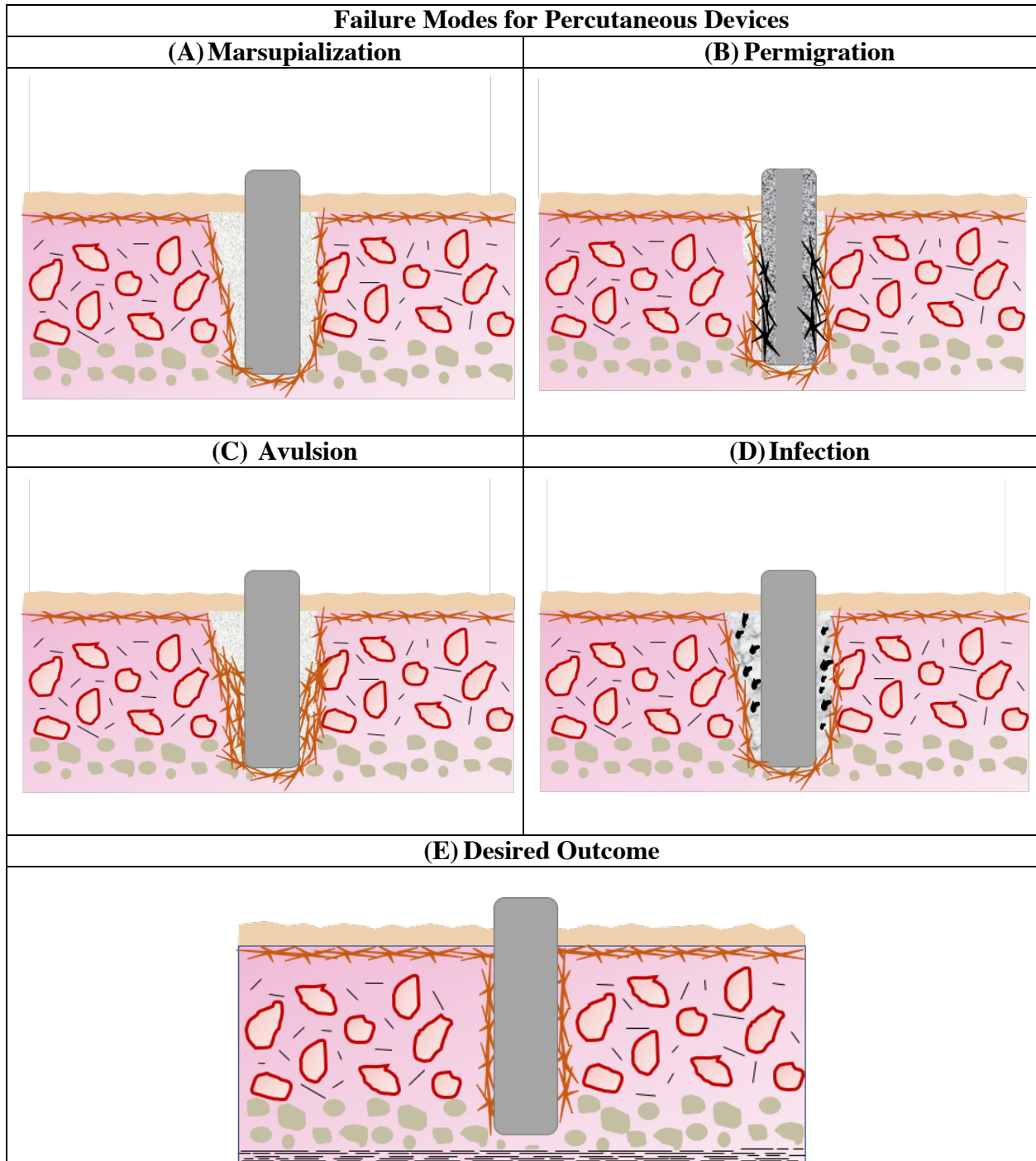


Figure 1.3. Failure Modes of Percutaneous Devices. (A) Marsupialization (B) Permigration (C) Avulsion (D) Infection (E) Desired Outcome. This figure was adapted from Von Recum⁴⁰.

Wound healing in the central nervous system (CNS) tissue slightly differs from other soft tissue because of the cells specific to that region. Similar to soft tissue, the process of inflammation

occurs in CNS tissue with the formation of a blood clot with the associated chemoattractants released by platelets, leading to the recruitment of leukocytes and activation of microglia. Neurons only contribute to 25% of the CNS tissue⁴⁴ and is accompanied by other resident cells such as microglia, astrocytes and vascular cells. Neutrophils are activated by cytokines and provide excavation of bacteria in the wound site by producing antimicrobial substances. Neutrophils undergo apoptosis within 48 hours if the wound is cleared^{45,46}. Macrophages produce cytokines and continue to clean foreign material from the wound³⁸. Microglia work in conjunction with macrophages and are phagocytic cells in the CNS tissue that become activated when there is debris present⁴⁶. The normal function of astrocytes delivers secretions to promote neuron development and support neurons mechanically, chemically, and electrically^{46,47}. Astrocytes can be identified partially by the upregulation of glial fibrillary actin protein⁴⁴ and they have been seen to facilitate proinflammatory and anti-inflammatory factors such as nitric oxide, which causes neurodegeneration⁴⁶. Axons in CNS tissue do not regenerate like peripheral cells do, but instead the CNS tissue surrounds the wounded area causing the initiation of gliosis. Glial scarring is suggested to create a barrier between damaged and healthy tissue from the adjacent CNS tissue in order to limit additional inflammatory response⁴⁴. Glial scarring can be compared to fibrous encapsulation present in soft tissue and can create medical device failure.

1.5 Soft Tissue and Central Nervous System Device Interfaces

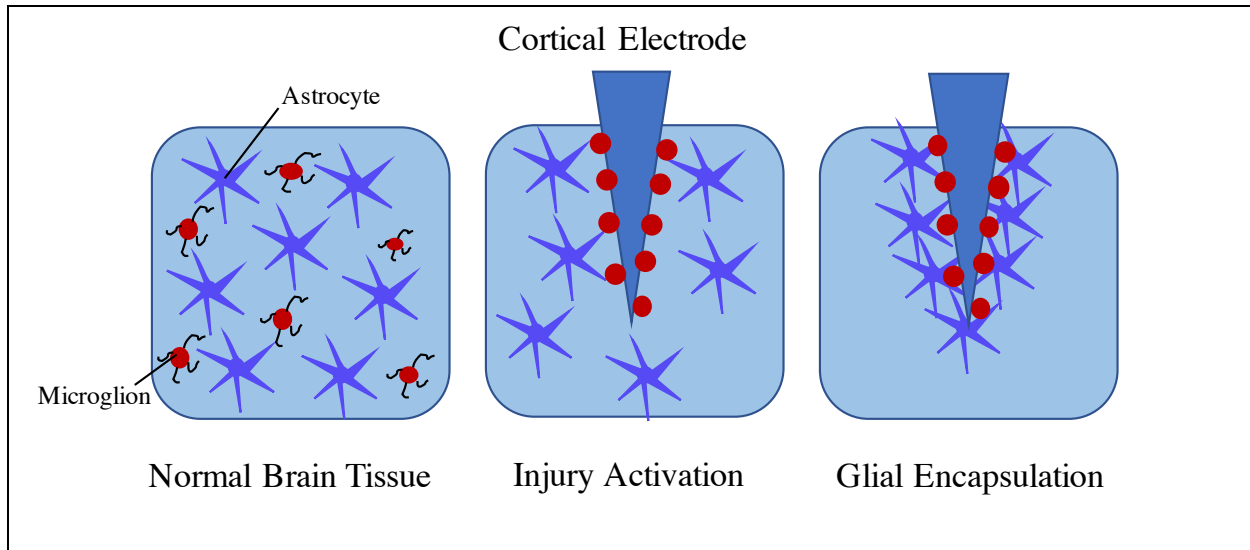


Figure 1.4. Glial Encapsulation schematic adapted by Grill et al.⁴⁸

Neural interface devices are used as intercortical implants for the treatment of neurological diseases, neuroprosthetics, and brain-computer interfaces to control external prosthetics. These devices suffer similar adverse reactions as percutaneous devices. Neural interface devices can take the form of an array of electrodes, used to transmit/receive electrical signals to/from brain cells. Glial scarring occurs as a consequence of electrode implantation because the CNS tissue recognizes the array as a foreign body and glial cells attempt to surround the implant and dissociate the array from healthy, undisturbed brain tissue, similar to the encapsulation process that occurs within skin tissue. Glial scarring obstructs diffusion, increases impedance, and lengthens the distance between electrodes and neurons, hampering the function of the devices⁴⁴. Parylene C has been used to encapsulate electrodes and to aid in biocompatibility, act as an insulator, and provide a chemically and biologically inert interface⁴⁹, but it still does not aid in eliminating glial scarring.

Glucose sensors and indwelling catheters have been used to administer therapeutics and monitor glucose levels while distributing drugs into the body. Glucose sensors have been investigated as a modality to provide continuous glucose monitoring for type 1 diabetic patients,

which helps improve regulation of glucose and reduce the complications of the disease^{50,51}. *In vitro* studies have shown maintenance of glucose sensing for 3 months, but *in vivo* an additional coating is needed between the implant tubing and soft tissue⁵². Hydrogel films⁵³, modified poly(vinyl chloride) membranes⁵⁴, and sol-gel based coatings⁵⁵ have been implemented to help with the soft tissue-glucose sensor interface, but have shown no success in clinical applications. Indwelling catheters used for cancer treatments and dialysis are usually made of silicone with cuffs to anchor the device. Infections are a primary complication that patients endure, but skin necrosis and extravasation are secondary reactions as well⁵⁶⁻⁵⁸. Efforts to coat catheter tubing to combat infection and thrombogenicity have been attempted, but have not been heavily explored for the skin-tubing interface^{58,59}. Limited experimental investigations into surface coatings and topography have attempted to address these challenges and sustain long-term use, but have shown only limited success.

1.6 Surface Modifications to Improve Biocompatibility

Methods to enhance soft tissue-device interfaces include physicochemical, morphological, and biochemical modification. One example is to coat with organic or synthetic peptides that mimic adhesive ECM proteins. Laminin has been investigated as a protein coating; in this study, laminin was silanized to titanium and was seen to promote a greater number of stable focal adhesions⁶⁰. Jansen et al. performed *in vivo* experiments where implants were implanted into the dorsum and tibias in guinea pigs for up to 7 weeks, and the craniums and tibia of rabbits up to 8 months with hydroxyapatite-coated titanium^{61,62}. In the dorsum epithelium, the downgrowth was more than half the length of the external post and the internal flange showed fibrous encapsulation at 5 weeks. The cranium implants healed with limited complications, partially due to the low mechanical stress, but in all tibia implants, approximately 25% failed due to marsupialization or

avulsion^{61,62}. In another study, collagen type I was immobilized on a titanium and cells were allowed to adhere *in vitro*. HaCaT human keratinocytes cells showed the strongest adhesion on the collagen type I coating, where the addition of an RGD peptide bound to collagen showed no significance advantage⁶³. However, in another similar study, collagen-coated titanium implants showed fibrous encapsulation at the soft tissue interface in rats, it can be postulated that material flexibility can influence soft tissue response and reduce focal adhesion stress fibers, where stiffer materials provide a more suitable tissue response^{64,65}, possibly explaining inconsistencies between the studies.

Porous titanium has been implemented to aid in tissue and cell integration. The size of pores has been shown to have a significant effect on the skin integration of percutaneous implants. In a study conducted in rats for 3 and 6 weeks, it was discovered that skin integration was better in smaller (40-100 μm) pores compared to large pores (100-160 μm). Porous titanium rods were inserted in rats' backs, but not attached to bone, for up to 6 weeks. During the study, the authors postulated that the pore size (40-100 μm) promoted less extrusion than the larger pores, this may be due to less tissue migration through smaller pores causing a slower extrusion process in comparison⁸.

Implants with grooved surfaces have also been investigated for their effect on soft-tissue interfaces. When fibroblast and epithelial cells were exposed to titanium with 22 μm grooves on the surface, epithelial cells *in vivo* were shown to possess limited flexibility to migrate into the grooves, although fibroblasts were seen to migrate both *in vivo* and *in vitro*, and demonstrated the reduction of marsupialization in rats with parietal area titanium implants⁶⁶. In another study with nonporous (smooth) versus 30 μm micro-pitted surfaces, all smooth implants failed within 12 weeks from epithelial downgrowth in rats; 23% of the micro-pitted implants failed within 15 weeks

and one implant was intact at the study endpoint of 24 weeks⁹. Yet another study demonstrated that smooth percutaneous implants have a 7-fold increase of failure from infection while porous coatings inhibited infection, but did not eliminate it completely. Interestingly, this study also showed that all implants, porous, smooth or a combination thereof, showed some degree of marsupialization as well⁶⁷.

Percutaneous devices are vulnerable to contamination, with bacterial biofilms that are adhered to the medical device surface. A popular approach to combat infection includes antibacterial coatings. In an *in vitro* study, synthetic polymers were immobilized onto titanium alloys because of the antibacterial activity of quaternized poly(4-vinylpyridinium), the phosphate groups' biocompatibility. From this study, it was shown the poly(4-vinylpyridinium) aided in an antimicrobial effect in the presence of *Staphylococcus Epidermidis*. In this study, it was observed that human dermal fibroblasts are also able to adhere to the surface¹¹. In another approach, titanium alloys were spray coated with carbonated hydroxyapatite and further treated with antibiotics including gentamicin, amoxicillin, and cephalothin. Finally, biomaterials can be infused with antibiotics to enhance the antibacterial properties of substrates. Antibiotics that contained carboxyl groups increased efficacy of hydroxyapatite adherence and therefore had higher concentration of antibiotics^{12,68}. *Staphylococcus aureus* did not attach to an implant surface, while fibroblasts adhered and grew⁶⁹.

1.7 Keratin Biomaterials

Keratin has been used for medical applications since the 16th century. It was documented in the Ben Cao Gang Mu, a series of books on Chinese herbal medicine, that ground ash from human hair was used to expedite the wound healing process and aid in blood clotting⁷⁰. Keratins are categorized as intermediate filaments and are abundant in hair, fingernails, and skin. Hair

keratins are said to be “hard” keratins whereas epithelial keratins are “soft” keratins^{71,72}. Keratins have been used to aid in wound healing, drug delivery, hemostasis, peripheral nerve damage, and bone regeneration^{70,73–76}. Keratin is naturally derived, highly biocompatible, and can self-assemble into an organized structure allowing various cell types to adhere to it^{75,77–80}. It is postulated that the leucine-aspartic acid-valine (LDV) motif, which is a ligand for the integrin $\alpha4\beta1$ integrin, is the primary mode of attachment, but this has not been verified through published work^{70,81}. Although strong cell attachment is important, the skin-titanium interface must also withstand avulsion. Keratin’s ability to maintain contact with the implant due to its structured network can provide this boundary with efficient mechanical properties to withstand stresses.

Keratin extracts that are formed through oxidative processes are referred to as keratose (KOS); extracts formed through reductive chemistry are referred to as kerateine (KTN)⁸². Although both extracts originate from human hair fiber, they possess different chemical compositions and functions. KTN contains reactive thiol groups that allow it to crosslink with itself; sulfonic acid groups are formed in KOS extracts. The variation in keratin extracts affect polarity, water solubility, pH, and in vivo properties⁷². Cells can adhere to both KTN and KOS and need to be tested for cell adhesion and effects on cell phenotype. Regardless of the chemistry used to produce the extracts, the resulting keratin nanomaterial is comprised of the same proteins as fingernail, keratins K31 and K81^{72,83}.

1.8 Conclusion

Percutaneous and subcutaneous devices have numerous advantages in healthcare. There are many circumstances in which monitoring, sensing, delivering compounds, and implanting devices is facilitated by intimate integration with hard and soft tissues, and in particular in applications where devices must interface with several tissues as they may be anchored, pass through, and/or

protrude outside the patient. The multiple transitions present enormous challenges to device design and each tissue can be vastly different, with different cellular responses, mechanical and biochemical environments. Promising outcomes have been achieved for many devices, some of which are in current use, although performance improvements can be made and new devices are needed.

Surface enhancements have been employed in an attempt to improve tissue-implant interfaces and help eliminate the foreign body response while inducing normal wound healing responses. Although substantial efforts have been made, many investigations have been unable to translate clinically, resulting in continued limitations for patients using conventional technologies. Additional research aimed at soft tissue-implant interfaces may take inspiration from nature, where normal cell anchoring is facilitated by mechanisms such as integrin binding. Further studies that account for aspects of normal wound healing responses and tissue homeostasis may provide insight into novel and clinically relevant solutions.

1.9 References

1. Anderson, J. M., Rodriguez, A. & Chang, D. T. Foreign body reaction to biomaterials. *Semin. Immunol.* **20**, 86–100 (2008).
2. Valiathan, M. S. Material-tissue interface. *Bull. Mater. Sci.* **5**, 365–372 (1983).
3. Middleton, C. A., Pendegrass, C. J., Gordon, D., Jacob, J. & Blunn, G. W. Fibronectin silanized titanium alloy: a bioinductive and durable coating to enhance fibroblast attachment in vitro. *J. Biomed. Mater. Res. Part A* **83**, 1032–1038 (2007).
4. Reyes, C. D., Petrie, T. A., Burns, K. L., Schwartz, Z. & García, A. J. Biomolecular surface coating to enhance orthopaedic tissue healing and integration. *Biomaterials* **28**, 3228–3235 (2007).
5. Rammelt, S. *et al.* Coating of titanium implants with collagen, RGD peptide and chondroitin sulfate. *Biomaterials* **27**, 5561–5571 (2006).
6. Rammelt, S. *et al.* Coating of titanium implants with type-I collagen. *J. Orthop. Res.* **22**, 1025–1034 (2004).
7. Ferris, D. . *et al.* RGD-coated titanium implants stimulate increased bone formation in vivo. *Biomaterials* **20**, 2323–2331 (1999).
8. Farrell, B. J. *et al.* Effects of pore size, implantation time, and nano-surface properties on rat skin ingrowth into percutaneous porous titanium implants. *J. Biomed. Mater. Res. Part A* **102**, 1305–1315 (2014).
9. Chehroudi, B. & Brunette, D. M. Subcutaneous microfabricated surfaces inhibit epithelial recession and promote long-term survival of percutaneous implants. *Biomaterials* **23**, 229–237 (2002).
10. Engler, A. J., Sen, S., Sweeney, H. L. & Discher, D. E. Matrix elasticity directs stem cell lineage specification. *Cell* **126**, 677–689 (2006).
11. Calliess, T. *et al.* Antimicrobial surface coatings for a permanent percutaneous passage in the concept of osseointegrated extremity prosthesis. *Biomed. Tech. (Berl)*. **57**, 467–71 (2012).
12. Zhao, L., Chu, P. K., Zhang, Y. & Wu, Z. Antibacterial coatings on titanium implants. *J. Biomed. Mater. Res. Part B Appl. Biomater.* **91B**, 470–480 (2009).
13. Engel, J. & Chiquet, M. in *The Extracellular Matrix: an Overview* 1–39 (Springer Berlin Heidelberg, 2011). doi:10.1007/978-3-642-16555-9_1
14. Yamada, K. M. in *Cell Biology of Extracellular Matrix* 95–114 (Springer US, 1981). doi:10.1007/978-1-4613-0881-2_5
15. Schultz, G., Ladwig, G. & Wysocki, A. Extracellular matrix: review of its roles in acute and chronic wounds. *World wide wounds* (2005). at <<http://www.worldwidewounds.com/2005/august/Schultz/Test-ECM.html>>
16. Hascall, V. C. & Hascall, G. K. in *Cell Biology of Extracellular Matrix* 39–63 (Springer US, 1981). doi:10.1007/978-1-4613-0881-2_3
17. Linsenmayer, T. F. in *Cell Biology of Extracellular Matrix* 5–37 (Springer US, 1981). doi:10.1007/978-1-4613-0881-2_2
18. Franzblau, C. & Faris, B. in *Cell Biology of Extracellular Matrix* 65–93 (Springer US, 1981). doi:10.1007/978-1-4613-0881-2_4
19. Yamada, K. M. Adhesive recognition sequences. *J. Biol. Chem.* **266**, 12809–12812 (1991).

20. Zhu, J. Bioactive Modification of Poly(ethylene glycol) Hydrogels for Tissue Engineering. doi:10.1016/j.biomaterials.2010.02.044
21. Rahmany, M. B. & Van Dyke, M. Biomimetic approaches to modulate cellular adhesion in biomaterials: A review. *Acta Biomater.* **9**, 5431–5437 (2013).
22. Verma, V., Verma, P., Ray, P. & Ray, A. R. Preparation of scaffolds from human hair proteins for tissue-engineering applications. *Biomed. Mater.* **3**, 25007 (2008).
23. Morgan, M. R., Humphries, M. J. & Bass, M. D. Synergistic control of cell adhesion by integrins and syndecans. *Nat. Rev. Mol. Cell Biol.* **8**, 957–969 (2007).
24. Campbell, I. & Humphries, M. Integrin structure, activation, and interactions. *Cold Spring Harb.* (2011). at <<http://cshperspectives.cshlp.org/content/3/3/a004994.short>>
25. Parsons, J., Horwitz, A. & Schwartz, M. Cell adhesion: integrating cytoskeletal dynamics and cellular tension. *Nat. Rev. Mol. cell* (2010). at <<http://www.nature.com/nrm/journal/v11/n9/abs/nrm2957.html>>
26. Srichai, M. B. & Zent, R. in *Cell-Extracellular Matrix Interactions in Cancer* 19–41 (Springer New York, 2010). doi:10.1007/978-1-4419-0814-8_2
27. Frame, M. C., Patel, H., Serrels, B., Lietha, D. & Eck, M. J. The FERM domain: organizing the structure and function of FAK. *Nat. Rev. Mol. Cell Biol.* **11**, 802–814 (2010).
28. Giancotti, F. G. & Ruoslahti, E. Integrin signaling. *Science* **285**, 1028–32 (1999).
29. Tapon, N. & Hall, A. Rho, Rac and Cdc42 GTPases regulate the organization of the actin cytoskeleton. *Curr. Opin. Cell Biol.* **9**, 86–92 (1997).
30. Nobes, C. D. & Hall, A. Rho, rac, and cdc42 GTPases regulate the assembly of multimolecular focal complexes associated with actin stress fibers, lamellipodia, and filopodia. *Cell* **81**, 53–62 (1995).
31. Wells, R. G. The role of matrix stiffness in regulating cell behavior. *Hepatology* **47**, 1394–1400 (2008).
32. Reichelt, J. Mechanotransduction of keratinocytes in culture and in the epidermis. *Eur. J. Cell Biol.* **86**, 807–816 (2007).
33. Joung, Y.-H. Development of implantable medical devices: from an engineering perspective. *Int. Neurovol. J.* **17**, 98–106 (2013).
34. Klee, D. & Höcker, H. in *Biomedical Applications Polymer Blends* 1–57 (Springer Berlin Heidelberg, 2000). doi:10.1007/3-540-48838-3_1
35. Schmalenberg, K. E., Buettner, H. M. & Urich, K. E. Microcontact printing of proteins on oxygen plasma-activated poly(methyl methacrylate). *Biomaterials* **25**, 1851–7 (2004).
36. Pinto, S. *et al.* Poly(dimethyl siloxane) surface modification by low pressure plasma to improve its characteristics towards biomedical applications. *Colloids Surfaces B Biointerfaces* **81**, 20–26 (2010).
37. Williams, D. F. On the mechanisms of biocompatibility. *Biomaterials* **29**, 2941–2953 (2008).
38. Berton, G. & Lowell, C. A. Integrin Signalling in Neutrophils and Macrophages. *Cell. Signal.* **11**, 621–635 (1999).
39. Linder, S., Hufner, K., Wintergerst, U. & Aepfelbacher, M. Microtubule-dependent formation of podosomal adhesion structures in primary human macrophages. *J. Cell Sci.* **113**, (2000).

40. von Recum, A. F. Applications and failure modes of percutaneous devices: a review. *J. Biomed. Mater. Res.* **18**, 323–336 (1984).
41. Martin, P. Wound healing--aiming for perfect skin regeneration. *Science* **276**, 75–81 (1997).
42. Raja, Sivamani, K., Garcia, M. S. & Isseroff, R. R. Wound re-epithelialization: modulating keratinocyte migration in wound healing. *Front. Biosci.* **12**, 2849–68 (2007).
43. Gurtner, G. C., Werner, S., Barrandon, Y. & Longaker, M. T. Wound repair and regeneration. *Nature* **453**, 314–321 (2008).
44. Polikov, V. S., Tresco, P. A. & Reichert, W. M. Response of brain tissue to chronically implanted neural electrodes. *J. Neurosci. Methods* **148**, 1–18 (2005).
45. Wilgus, T. A., Roy, S. & McDaniel, J. C. Neutrophils and Wound Repair: Positive Actions and Negative Reactions. doi:10.1089/wound.2012.0383
46. Stroncek, J. D. & Reichert, W. M. *Overview of Wound Healing in Different Tissue Types. Indwelling Neural Implants: Strategies for Contending with the In Vivo Environment* (CRC Press/Taylor & Francis, 2008). at <<http://www.ncbi.nlm.nih.gov/pubmed/21204404>>
47. Kimelberg, H., Jalonen, T. & Walz, W. in *Astrocytes: pharmacology and function* 193–222 (1993).
48. Grill, W. M., Norman, S. E. & Bellamkonda, R. V. Implanted Neural Interfaces: Biochallenges and Engineered Solutions. *Annu. Rev. Biomed. Eng.* **11**, 1–24 (2009).
49. Hassler, C., von Metzen, R. P., Ruther, P. & Stieglitz, T. Characterization of parylene C as an encapsulation material for implanted neural prostheses. *J. Biomed. Mater. Res. Part B Appl. Biomater.* **9999B**, NA-NA (2010).
50. Turner, R. F. B., Harrison, D. J., Rajotte, R. V. & Baltes, H. P. A biocompatible enzyme electrode for continuous in vivo glucose monitoring in whole blood. *Sensors Actuators B Chem.* **1**, 561–564 (1990).
51. David A. Gough,* Joseph Y. Lucisano, and P. H. S. T. Two-Dimensional Enzyme Electrode Sensor for Glucose. *Anal. Chem.* **57**, 2351–2357 (1985).
52. A. Kros. *Amperometric Biosensors Based on Conducting Nanotubes*. (University of Wijegan, 2000).
53. Quinn, C. A. P., Connor, R. E. & Heller, A. Biocompatible, glucose-permeable hydrogel for in situ coating of implantable biosensors. *Biomaterials* **18**, 1665–1670 (1997).
54. Reddy, S. M. & Vagama, P. M. Surfactant-modified poly(vinyl chloride) membranes as biocompatible interfaces for amperometric enzyme electrodes. *Anal. Chim. Acta* **350**, 77–89 (1997).
55. Kros, A. *et al.* Silica-based hybrid materials as biocompatible coatings for glucose sensors. *Sensors Actuators B Chem.* **81**, 68–75 (2001).
56. Minassian, V. A. *et al.* Longterm central venous access in gynecologic cancer patients. *J. Am. Coll. Surg.* **191**, 403–409 (2000).
57. Kock, H.-J., Pietsch, M., Krause, U., Wilke, H. & Eigler, F. W. Implantable Vascular Access Systems: Experience in 1500 Patients with Totally Implanted Central Venous Port Systems. *World J. Surg* **22**, 12–16 (1998).
58. Kurul, S., Saip, P. & Aydin, T. Totally implantable venous-access ports: local problems and extravasation injury. *Lancet. Oncol.* **3**, 684–92 (2002).
59. Galloway, S. & Bodenham, A. Long-term central venous access. doi:10.1093/bja/aeh109

60. Gordon, D. J., Bhagawati, D. D., Pendegrass, C. J., Middleton, C. A. & Blunn, G. W. Modification of titanium alloy surfaces for percutaneous implants by covalently attaching laminin. *J. Biomed. Mater. Res. Part A* **9999A**, NA-NA (2010).
61. Jansen, J. A., van der Waerden, J. P. & de Groot, K. Epithelial reaction to percutaneous implant materials: in vitro and in vivo experiments. *J. Invest. Surg.* **2**, 29–49 (1989).
62. Jansen, J. A., van der Waerden, J. P. & de Groot, K. Tissue reaction to bone-anchored percutaneous implants in rabbits. *J. Invest. Surg.* **5**, 35–44
63. Roessler, S. *et al.* Biomimetic coatings functionalized with adhesion peptides for dental implants. *J. Mater. Sci. Mater. Med.* **12**, 871–877 (2001).
64. Holgers, K.-M., Esposito, M., Källtorp, M. & Thomsen, P. in 513–560 (Springer, Berlin, Heidelberg, 2001). doi:10.1007/978-3-642-56486-4_16
65. Jansen, J. A., von Recum, A. F., van der Waerden, J. P. C. M. & de Groot, K. Soft tissue response to different types of sintered metal fibre-web materials. *Biomaterials* **13**, 959–968 (1992).
66. Chehroudi, B., Gould, T. R. L. & Brunette, D. M. A light and electron microscopic study of the effects of surface topography on the behavior of cells attached to titanium-coated percutaneous implants. *J. Biomed. Mater. Res.* **25**, 387–405 (1991).
67. Isackson, D., McGill, L. D. & Bachus, K. N. Percutaneous implants with porous titanium dermal barriers: An in vivo evaluation of infection risk. *Med. Eng. Phys.* **33**, 418–426 (2011).
68. Stigter, M., Bezemer, J., de Groot, K. & Layrolle, P. Incorporation of different antibiotics into carbonated hydroxyapatite coatings on titanium implants, release and antibiotic efficacy. *J. Control. Release* **99**, 127–137 (2004).
69. Harris, L. G., Tosatti, S., Wieland, M., Textor, M. & Richards, R. G. Staphylococcus aureus adhesion to titanium oxide surfaces coated with non-functionalized and peptide-functionalized poly(l-lysine)-grafted-poly(ethylene glycol) copolymers. *Biomaterials* **25**, 4135–4148 (2004).
70. Rouse, J. G. & Van Dyke, M. E. A review of keratin-based biomaterials for biomedical applications. *Materials (Basel)*. **3**, 999–1014 (2010).
71. Hill, P., Brantley, H. & Van Dyke, M. Some properties of keratin biomaterials: kerateines. *Biomaterials* **31**, 585–593 (2010).
72. de Guzman, R. C. *et al.* Mechanical and biological properties of keratose biomaterials. *Biomaterials* **32**, 8205–8217 (2011).
73. de Guzman, R. C. *et al.* Bone regeneration with BMP-2 delivered from keratose scaffolds. *Biomaterials* **34**, 1644–1656 (2013).
74. Aboushwareb, T. *et al.* A keratin biomaterial gel hemostat derived from human hair: evaluation in a rabbit model of lethal liver injury. *J. Biomed. Mater. Res. Part B Appl. Biomater.* **90**, 45–54 (2009).
75. Sierpinski, P. *et al.* The use of keratin biomaterials derived from human hair for the promotion of rapid regeneration of peripheral nerves. *Biomaterials* **29**, 118–128 (2008).
76. Van Dyke, M. E. Wound healing compositions containing keratin biomaterials. (2012).
77. Richter, J. R., de Guzman, R. C. & Van Dyke, M. E. Mechanisms of hepatocyte attachment to keratin biomaterials. *Biomaterials* **32**, 7555–7561 (2011).

78. Tachibana, A., Kaneko, S., Tanabe, T. & Yamauchi, K. Rapid fabrication of keratin–hydroxyapatite hybrid sponges toward osteoblast cultivation and differentiation. *Biomaterials* **26**, 297–302 (2005).
79. Van Dyke, M. E. & Teli, T. Stem cell differentiation using keratin biomaterials. (2013). at <<http://www.google.com/patents/US20130251690>>
80. Reichl, S. Films based on human hair keratin as substrates for cell culture and tissue engineering. *Biomaterials* **30**, 6854–6866 (2009).
81. Tachibana, A., Furuta, Y., Takeshima, H., Tanabe, T. & Yamauchi, K. Fabrication of wool keratin sponge scaffolds for long-term cell cultivation. *J. Biotechnol.* **93**, 165–170 (2002).
82. Crewther, W. G., Fraser, R. D. B., Lennox, F. G. & Lindley, H. The chemistry of keratins. *Adv. Protein Chem.* **20**, 191–346 (1965).
83. Perrin, C., Langbein, L. & Schweizer, J. Expression of hair keratins in the adult nail unit: an immunohistochemical analysis of the onychogenesis in the proximal nail fold, matrix and nail bed. *Br. J. Dermatol.* **151**, 362–371 (2004).

**Chapter 2. Development and Characterization of a
Biomimetic Coating for Percutaneous Devices**

Alexis Trent¹, Mark E. Van Dyke^{2}*

Department of Materials Science and Engineering, Virginia Tech, Blacksburg, VA 24060

Department of Biomedical Engineering and Mechanics, Virginia Tech, Blacksburg, VA

24060

(Submitted for Publication)

*Corresponding author email: mvandyk5@vt.edu

2.1 Abstract

Percutaneous medical devices pass through the skin and typically have exterior and interior components. More specifically, percutaneous osseointegrated prosthetics (POP), which consist of a metallic post attached to the bone that extends outward through the skin to connect to an external prosthesis, have become a clinically relevant option to replace the typical socket-residual limb connection. These devices create several challenges including epidermal downgrowth, increased infection risk, and mechanical tearing at the skin-implant interface. To remedy these issues, biomimetic surfaces and coatings have been developed to create an infection-free and cohesive boundary between POPs and skin. The fingernail is a prime example of a natural system with a skin interface that is both mechanically and biologically stable. The human fingernail is composed predominantly of hard keratins, which are intermediate filament-forming proteins also found in hair fibers. Keratins have been investigated as a biomaterial for coatings, hydrogels, films, and scaffolds. Exploiting keratins' previously demonstrated tissue compatibility to create a biomimetic coating for POPs that can imitate the junction of the human fingernail and skin is the goal of this work. Here we investigate keratin nanomaterials' ability to form coatings for percutaneous devices. Results suggest a silane-coupled keratin layer can create uniform coatings and maintain biological function while withstanding weeks of enzyme degradation. Our experimental data provides justification to further explore keratin nanomaterials for POP coatings that may stabilize the implant-skin interface.

Keywords: Keratin, percutaneous, osseointegrated, prosthetic, biomimetic, coating, biomaterial, nanomaterial, fingernail, skin, interface, implant, medical device

2.2 Introduction

Percutaneous medical devices are intended to pass through the skin and typically have exterior and interior components. Examples of percutaneous devices include catheters, artificial limbs, glucose sensors, and dental implants^{1,2}. Implant encapsulation, infection, and necrosis are a few adverse reactions observed with these devices,¹ mediated by unwanted responses from the skin. Methods to improve the skin-implant interface have been previously attempted and include altering physicochemical, morphological, and biochemical aspects of the device's surface in order to negate the foreign body response. In the case of indwelling catheters and glucose sensors, surface modifications including drug-eluting coatings and biocompatible polymers have been investigated to aid in resistance to infection³ and reduce fibrosis and inflammation.

In prosthetic limb attachment, amputees place residual limbs in a socket-type interface, which is attached to the prosthesis. Unfortunately, there are many disadvantages of the socket interface including pain caused by poor socket fit, skin irritation, improper loading, lack of mobility, and instability^{4,5}. Each year approximately 160,000 people undergo amputation. These patients include military personnel, who are typically affected by high velocity explosions and ballistics, and civilians, who are affected by automobile accidents, gunshot wounds, and complications from diabetes⁶. The number of people living with an amputation is expected to increase from the 1.6 million in 2005 to 3.6 million in 2050⁷.

Recently, percutaneous osseointegrated prosthetics (POP), bone-anchored posts that protrude through the skin to attach to an external prosthesis, have been recognized for improving amputees' functionality, mechanical stability, osseoperception, and quality of life^{4,8-12}. Haptics and neural sensory advances to POP and other prostheses represent technologies that allow the perception of touch and neural-control of artificial limbs, which further improves the lives of

amputees^{13,14}. Although these advances are being explored, the interface between the POP and skin remains an underlying challenge to the progression of this field.

The surgical implantation method for lower limb POPs has been well established using a two-step surgical procedure to reduce internal and external complications, but current biomaterial grade titanium, which is used as a typical material for POP, has not achieved long-term success^{9,12,15}. Complications include marsupialization, or a combination of fibrous encapsulation and epidermal downgrowth, infection, permigration, or necrosis that occurs within porous implants, avulsion, or a combination thereof^{1,16}. To address these issues, different modifications have been applied to the titanium surface in an effort to create a cohesive junction with the skin¹⁷.

Biomimetic surfaces, surface topography, and antibacterial coatings are some of the potential ways to approach the creation of a stable interface. Extracellular matrix (ECM) is a three-dimensional matrix that provides biochemical cues and structure that supports cell adhesion, migration, and biological function within organs and tissues¹⁸⁻²⁰. Most efforts for coating percutaneous implants have been made by coating titanium with ECM proteins and adhesive peptides, but this research has focused mainly on bone regeneration at the internal titanium-bone boundary and not the skin. In published studies, type-I collagen and hydroxyapatite have been shown to increase bone formation around implants and aid in bone attachment^{21,22}. At the implant-skin interface, these coatings only slightly inhibited epithelial downgrowth but did not prevent it. Similarly, modifying a titanium rod with the coating of arginine-glycine-aspartic acid (RGD) peptide increased bone thickness *in vivo* and coatings with the peptide GFOGER have shown increased bone formation^{23,24}. The ECM protein laminin, a component of the basement membrane, was coated via silane coupling to a titanium alloy in an effort to increase adhesion of skin cells, which resulted in smaller cells with a greater density of focal adhesions versus non-coated surfaces

²⁵. Other concepts have consisted of inorganic coatings, functionalized polymer coatings, ceramic coated titanium alloys, and negative pressure wound therapy, as various attempts to limit epithelial downgrowth and aid in osseointegration, but further limitations, such as infection and inflammation, halted the success of these methods ²⁶⁻²⁸. Again, these approaches focused primarily on the titanium-bone interface, not the skin, leaving the skin-implant interface as a persistent obstacle in POP technology.

More recently, the titanium surface structure has been manipulated to include pores or microgrooves, and this has been observed to improve skin integration and inhibit downgrowth or marsupialization to a limited extent ²⁹. Successful adhesion to the skin was found to be dependent on the size of pores. At smaller pore sizes, cells did not readily migrate into the pores, but at larger pore sizes the cells experience permigration ²⁹⁻³².

To counteract increased infection risk, antibacterial coatings have also been employed. Sol-gels, polymers, and organic coatings with controlled release of antibiotics and gases such as nitrogen monoxide have been investigated as approaches to resist bacterial adhesion ^{33,34}. These methods have shown some benefit in addressing the drawbacks associated with the POP-skin interface, but to date, there is no published literature that describes successful clinical translation of these or similar methods. Further investigation must be undertaken to develop an approach that creates a skin-implant interface for POPs that can achieve long-term success in a user population.

A potential solution is a skin-POP interface engineered to emulate the fingernail-skin junction - an infection free and mechanical stable interface that is intimately connected to the skin. Fingernails, hair, animal wool, and hooves are all composed of the intermediate filament protein keratin and are considered natural percutaneous “devices” ³⁵. Keratin has been used in various medical applications dating back to the 16th century ³⁶ and has more recently shown versatility and

applicability as a biomaterial. Human trichocytic (i.e. “hard”) keratins K31, K34, K81, and K85 have been identified in extracts of human hair fibers³⁷ and are also found in the human nail³⁸. Using keratins extracted from human hair fibers to coat metal implant surfaces and mimic the nail may serve as a method of robust skin cell on-growth. The goal of this study is to investigate extracted keratin’s ability to form a robust coating on the surface of titanium and present a surface for skin cell adhesion. The common methodology of silane coupling chemistry was used to attach different forms of purified keratin nanomaterials to titanium substrates, which were characterized by atomic force microscopy, x-ray photon spectroscopy, and contact angle. Durability of the coatings was assessed by performing degradation experiments in simulated tissue environments. Adhesion of dermal fibroblasts and keratinocytes was performed, wherein focal adhesion and cytoskeletal maturity were investigated.

2.3 Methods

2.3.1 Keratin Extraction

Keratins were isolated as a nano-scale complex (“keratin nanomaterial”) of type I and type II keratin monomers using a proprietary process³⁹. Briefly, human hair fibers were treated with either peracetic acid (keratose or KOS) or thioglycolate (kerateine or KTN) solutions to affect disulfide bond cleavage through oxidative and reductive chemistry respectively. Subsequent extraction of cortical proteins was performed using buffer solution containing 100mM of 2-amino-2-(hydroxymethyl)-1,3-propanediol, which was subsequently clarified of suspended solids by centrifugation, followed by filtration. Keratin nanomaterial (KN) was isolated from the crude extract using tangential flow filtration against buffer using a 100 kDa nominal low molecular weight cutoff membrane in a custom-built, recirculating system. After multiple wash cycles to

remove low molecular weight peptides and processing chemicals, the solution was concentrated and freeze dried.

2.3.2 *Automated Western Blot System (Capillary Electrophoresis Immunoassay)*

The keratin protein K31 was identified in KOS and KTN samples using an automated Western blot technique (Wes Simple Western Analysis, ProteinSimple, San Jose, USA). An initial sample concentration of 3 mg/ml of KTN or KOS was created using the ProteinSimple kit with slight modification. The preparation of the Fluorescent 5X Master Mix and Biotinylated Ladder were prepared without the addition of dithiothreitol (DTT), which was replaced with UltraPure Distilled Water (ThermoFisher, Waltham, MA, USA). Keratin solutions were combined with the 5X Fluorescent solution for a final concentration of 0.4 $\mu\text{g}/\mu\text{l}$. Neither the samples nor the ladder were denatured by heating. Primary Antibody K31 (Progen Biotechnik, Germany) was diluted 1:50 with the ProteinSimple Antibody Diluent and the secondary antibody, Rabbit anti-Guinea Pig IgG (H+L), HRP (ThermoFisher, Waltham, MA, USA) was diluted 1:100. Along with Luminol-Peroxide Mix and Wash Buffer, solutions were placed in their respective locations according to the Wes Plating system, run and analyzed with ProteinSimple's Compass software.

2.3.3 *Size Exclusion Chromatography (SEC)*

SEC was conducted on samples dissolved at a concentration of 0.2mg/mL in mobile phase. The SEC system consisted of a Dionex Ultimate 3000 quaternary analytical pump, Rheodyne manual injection loop, and Ultimate 3000 UV/Vis detector. The mobile phase, flowing at 1mL/min, was 10mM dibasic sodium phosphate/100mM sodium chloride at pH 7.4, and a BioBasic SEC-1000 column, 7.8mm x 150mm, 5 μm particle size (ThermoFisher, Waltham, MA, USA), was used. Detection was at 280nm and data collected using a laptop computer running

Chromleon v6.8 chromatography software. The system was standardized against bovine albumin.

2.3.4 Silane Coupling and Protein Deposition

Titanium coated glass microscope slides (Deposition Research Lab Inc. CO, USA) were cut into 0.8 cm by 0.8 cm substrates, which were cleaned in 100% ethanol (EtOH) and wiped with a Kimwipe to remove any heavy debris. Different silane couplings were chosen to observe affects to KN deposition. Silane solutions consisted of 5 % 3-Aminopropyltriethoxysilane (APTES; TCI America, Portland, OR, USA) dissolved in 95:5 EtOH: H₂O solution (v/v), 5% Glycidoxypropyltrimethoxysilane (GPTES; Acros Organics, Geel, Belgium) dissolved in 95:5 EtOH: H₂O solution (v/v), 10 % 3-Mercaptopropyltriethoxysilane (MPTES; TCI America, Portland, OR, USA) dissolved in 100% EtOH (v/v) or 10% 3- Isocyanatopropyltriethoxysilane (ICPTES; Acros Organics, Geel, Belgium) dissolved in 100% EtOH (v/v). The titanium substrates were placed in silane solution that was filtered through a 0.2µm pore size membrane, followed by constant and gentle agitation at room temperature (RT) for 3 hours. Once removed, the substrates were rinsed with 100% ethanol three times, rinsed with ultrapure water, and dried at 110°C for 30 minutes. Silane treated slides were coated with either 1% keratose (KOS; w/v) dissolved in 10 mM sodium phosphate at pH 7.4, or 1% keratine (KTN; w/v) dissolved in 10 mM sodium phosphate at pH 7.4 by overnight incubation. Human fibronectin (FN; Corning, Corning, NY, USA) was coated for a surface concentration of 5 µg/cm² in phosphate buffered saline (PBS) and bovine collagen I (COL; Corning, Corning, NY, USA), which is only used for the degradation assay, was coated at 5 µg/cm² in 0.01N HCl concentration on silane treated slides. Both FN and COL were incubated for 1 hour at RT. For gold substrates, no silane coupling was used and a 1% (w/v) KTN solution was incubated over the substrate overnight. For all coatings, excess protein solution was

removed and the substrates rinsed with ultrapure water three times. All substrates were uncovered and air dried under a biological hood, then exposed to ultraviolet light (UV) for sterilization for 1 hour prior to further use.

2.3.5 *Atomic Force Microscopy (AFM)*

Dry samples were observed in a Veeco BioScope II (Oyster Bay, NY) under tapping mode in ambient conditions. A silicon tip (Nanosensors, Switzerland) with curvature of less than 10 nm and a force constant from 10 -130 N/m was used. Each experimental group consisted of three analyzed substrates, where five 2 μm by 2 μm spot sizes were evaluated on each sample using the Nanoscope program; this totaled 15 spot sizes for each experimental substrate. Surface roughness was analyzed with root mean squared (RMS), which defines the variation of height from the mean of data and is more sensitive to peaks and valleys than an average roughness value. Topography was rendered with the Bruker Nanoscope software.

2.3.6 *X-ray Photon Spectroscopy (XPS)*

XPS analysis was conducted with a PHI Quantera SXM, equipped with a monochromatic X-ray source (Al K-alpha anode) operating at 15kV and 280W. The spot analyzed was 200 μm with an approximate base pressure of 10^{-8} Pa. A 5° angle was used between the electron analyzer and sample, and elements were quantified using the MultiPak software.

2.3.7 *Contact Angle*

The wettability of the experimental substrates was determined by contact angle at 25°C using a Model 100-00-115 (Rame-Hart Inc.) goniometer. A micropipette was used at 2 $\mu\text{l/s}$ to create a droplet of water and the contact angle measured after 10 seconds. Three samples were analyzed per coating with five readings taken per sample, and the average of the 15 readings was recorded as the experimentally determined value.

2.3.8 *Enzyme Degradation*

Keratinase (Sigma Aldrich, St. Louis, MO), Collagenase Type I (Worthington Biochemical Corporation, Lakewood, NJ, USA), Elastase (Worthington Biochemical Corporation, Lakewood, NJ, USA), and Matrix metalloproteinase 9 (MMP-9; EMD Millipore, Billerica, MA, USA) were diluted to 0.15U/mL in PBS and sterile filtered. Substrates were covered with 1 mL enzyme solution or PBS for 1 day, 7 days, 4 weeks, 8 weeks, and 16 weeks at 37°C. For the 16-week time point, another 1 mL of enzyme solution or PBS was added at 8 weeks. At the end point, enzyme solution was aspirated and substrates rinsed three times with ultrapure water. The substrates were analyzed with XPS after each enzyme timepoint.

2.3.9 *Adhesion Motif Detection*

FluoSpheres Carboxylate-Modified 1 μm diameter microspheres (ThermoFisher, Waltham, MA, USA) were passively attached to Recombinant Human Integrin alpha 4 beta 1 protein ($\alpha 4\beta 1$; R&D Systems, Minneapolis, MN, USA) and Recombinant Human Integrin alpha 2b beta 3 protein ($\alpha \text{IIb} \beta 3$; R&D Systems, Minneapolis, MN, USA), overnight at RT while being shaken continuously without exposure to light. Then, each substrate was covered with a 1 mL solution that contained 1.0×10^8 of the antibody-coated fluorescent beads. After 3 hours at RT, the bead solution was aspirated and the substrates rinsed three times with ultrapure water. The substrates were then imaged on a Zeiss Observer.A1 microscope at 10X. Image J was used to quantify the number of spheres and a custom Matlab code was used to determine the distances between the spheres.

2.3.10 *Cell culture*

Human neonatal primary dermal fibroblast (PCS-201-010) were obtained from ATCC (Manassas, VA, USA) and grown in RPMI 1640, L-Glutamine, with no sodium pyruvate (Gibco

Life Technologies Carlsbad, CA, USA). 10 % fetal bovine serum (FBS; Gibco Life Technologies Rockville, MD, USA) and 1% penicillin streptomycin (P/S) were added to supplement the growth media. Human keratinocytes HaCaT cells (Catalog #T0020001) were obtained from AddexBio Technologies (San Diego, CA, USA) and cultured in Dulbecco's Modified Eagle's Medium (DMEM; ThermoFisher, Waltham, MA, USA), with 10% FBS, 1% P/S and 1.5mM sodium pyruvate (ThermoFisher, Waltham, MA, USA). All cells were split 1 to 3 every 2-3 days and incubated at 37°C, 5% CO₂.

2.3.11 Focal Adhesion Immunocytochemistry

Fibroblast and HaCaT cells were seeded at 10,000 cells/cm² in a 40 µl droplet onto the substrates and incubated at 37°C for 30 minutes, 1 hour, and 3 hours, then fixed with 4% paraformaldehyde. Cells were permeabilized for 5 minutes with 0.1% Triton X-100 in 1X PBS, washed twice with wash buffer (0.05% Tween-20 in 1X PBS), and blocked with 1% bovine serum albumin (BSA; Sigma Aldrich St. Louis, MO) in 1X PBS for 30 minutes at RT. Focal adhesions (F-actin and vinculin) were stained with the FAK 100 kit according to the manufacture's protocol (EMD Millipore, Billerica, MA, USA). Dilutions of antibodies were as follows: primary antibody Anti-Vinculin (1:350), the secondary Alexa Flour 488 (1:300), Phalloidin (1:350) and DAPI (1:1000). A Zeiss Imager A1m microscope was used to image the cells at 20X.

2.3.12 Detection of Smooth Muscle Actin (SMA) in Fibroblasts

Fibroblasts were seeded at 10,000 cells/cm² in a 40 µl droplet placed onto the substrates and incubated at 37°C for 3 hours. After incubation, cells were fixed with 4% paraformaldehyde, then permeabilized for 5 minutes with 0.1% Triton X-100 in 1X PBS, washed twice with wash buffer (0.05% Tween-20 in 1X PBS), and blocked with 1% BSA in 1X PBS for 30 minutes at RT. The primary antibody, alpha-SMA (1:200) in 1% BSA, was incubated overnight at 4°C. Cells were

washed with wash buffer three times then the Alexa Flour 488 (ThermoFisher, Waltham, MA, USA) was applied as the secondary antibody (1:400) for 1 hour at RT. 4', 6-diamidino-2-phenylindole (DAPI; 1:1000) was then used to stain cell nuclei at RT. A Zeiss Imager A1m microscope was used to image the cells at 20X.

2.3.13 *Detection of Involucrin in HaCaTs*

HaCaT cells were seeded at 10,000 cells/cm² in a 40 μ l droplet onto the substrates and incubated at 37°C for 3 hours, 1 day, and 7 days. After incubation, cells were fixed with 4% paraformaldehyde, then permeabilized for 5-10 minutes with 0.1% Triton X-100 in 1X PBS, washed twice with wash buffer (0.05% Tween-20 in 1X PBS), and blocked with 1% BSA in 1X PBS for 30 minutes at RT. The primary antibody, involucrin (ThermoFisher, Waltham, MA, USA) (1:200) in 1% BSA, was incubated for 1 hour at RT. Cells were washed with wash buffer three times, then the Alexa Flour 488 (ThermoFisher, Waltham, MA, USA) was applied as the secondary antibody (1:400) for 30 minutes at RT. DAPI (1:1000) was then used to stain cell nuclei at RT. A Zeiss Imager A1m microscope was used to image the cells at 20X.

2.3.14 *Statistics*

Replicates of ≥ 3 were used in all experiments. All graphical data are reported as mean \pm one standard deviation. All graphical images used Graph Pad Prism for either one-way or two-way analysis of variance (ANOVA), with Tukey's or Bonferroni as the posthoc test for significance, respectively, with $\alpha \leq 0.05$. Image J and Photoshop (Adobe, San Jose, CA) were used for image processing and analysis.

2.4 Results

2.4.1 Western Blot

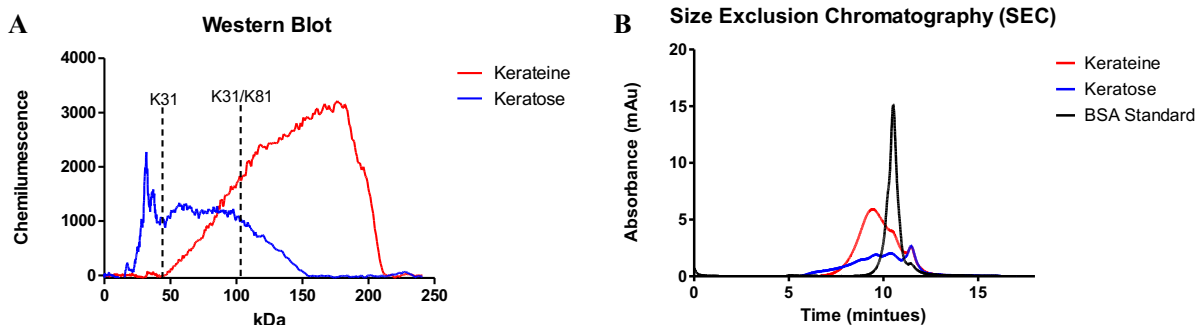


Figure 2.1. Western Blot and SEC. (A) Graphical representation of the electrophoresis results produced by the WES system (left) and SEC (right). Keratose has a peak approximately at 20 kDa, with a continued plateau until 150 kDa and kerateine has a gradual increase starting at 50kDa that drops off at 175kDa. These data are indicative of a high molecular weight keratin dimer at approximately 112kDa, as well as aggregates of dimers in the case of KTN. KTN contains a higher ratio of keratin nanomaterial (dimerized keratin) to protein fragments than KOS. (B) Based on the retention time for BSA (molecular weight of 66.5 kDa), KOS displays a peak in the 40-50 kDa range, whereas KTN ranges between 65-100kDa with a small shoulder between 40-50kDa.

Based on previous studies, human hair fiber extracts contain large amounts of K31 monomer and an antibody to this protein can be used to indicate the presence of human keratins in a sample³⁷. K31 antibody in the KOS sample is apparent in the WesTM analysis starting at ca. 37kDa and extending until ca. 150kDa, with a long tail between 100 and 150kDa (**Figure 2.1A**). Conversely, KTN shows less K31 staining at low molecular weight, peaking at ca. 175kDa and tailing off rapidly at ca. 210kDa. These data are consistent with the SEC chromatogram (**Figure 2.1B**), which shows a bimodal distribution of molecular weights for KOS, with a broad range of high molecular weight material from 7.5 to 10 minutes, followed by a low molecular weight peak at ca. 1.5 minutes, beyond the BSA standard at 10.5 minutes. KTN shows higher molecular weight content, with little material in the low molecular weight range below BSA (i.e. 66K Da).

2.4.2 XPS

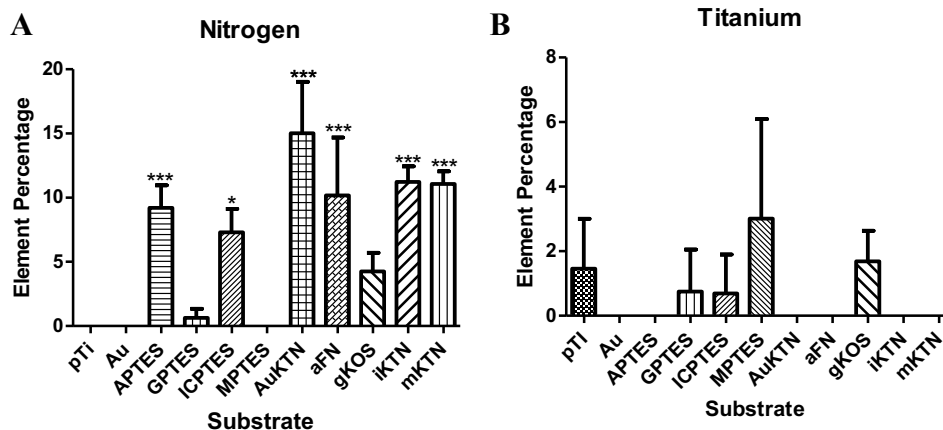


Figure 2.2. XPS. Elemental percentages from XPS analysis of substrates for nitrogen (A) and titanium (B). For all graphs, significance is only shown against pure Ti where * signifies $p \leq 0.05$, ** signifies $p \leq 0.01$, and *** signifies $p \leq 0.001$.

Elemental analysis by XPS demonstrates the presence of the intended coating, with nitrogen serving as a surrogate for protein (**Figure 2.2**). KTN has a high affinity for gold, owing to its sulfhydryl functionality, and shows the highest signal for nitrogen; the corresponding titanium signal is masked by the protein layer. KTN on gold serves as a standard to which other coatings can be compared. As expected, strong nitrogen signals are evident from the nitrogen-containing silane coatings (i.e. APTES, ICPTES), as well as all protein coatings. KOS demonstrated the weakest signal. MPTES's titanium signal contains a large standard deviation with the raw percentages ranging from 0%, 2.87%, and 6.16%, which may suggest a non-uniform coating. The titanium signal is most effectively masked by the KTN coatings, with no apparent reduction after coating with KOS.

2.4.3 AFM

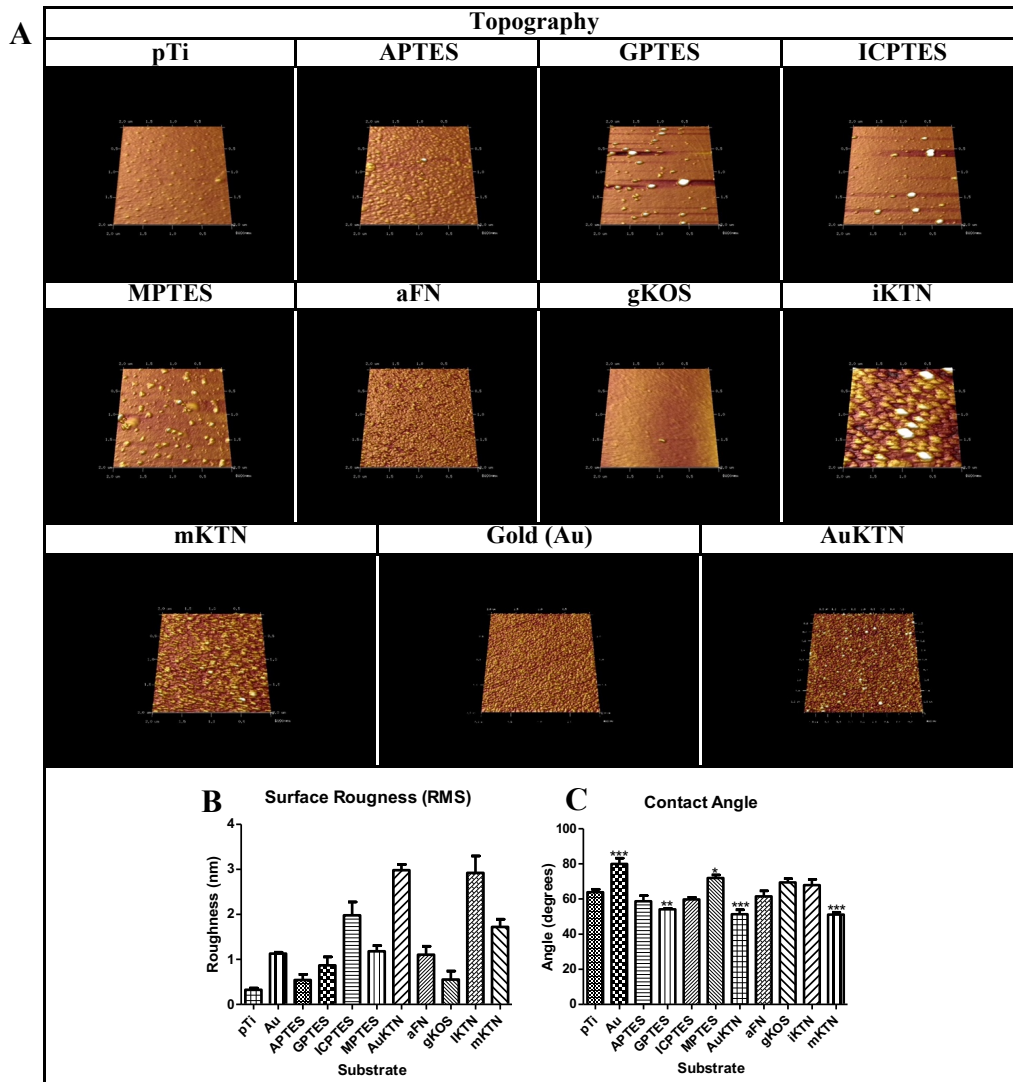


Figure 2.3. AFM. A) Rendered images of substrate topography. B) Graphical representations of RMS from AFM data. C) Graphical representation of the contact angle and significance is only shown against pTi, where * signifies $p \leq 0.05$, ** signifies $p \leq 0.01$, and *** signifies $p \leq 0.001$.

AFM Surface Roughness Significance Table											
	pTi	Au	APTES	GPTES	ICPTES	MPTES	AuKTN	aFN	gKOS	iKTN	mKTN
pTi		**	ns	ns	***	***	***	*	ns	***	***
AuKTN	***	***	***	***	***	***		***	***	ns	***
aFN	*	ns	ns	ns	***	ns	***		ns	***	*
gKOS	ns	*	ns	ns	***	*	***	ns		***	***
iKTN	***	***	***	***	***	***	ns	***	***		ns
mKTN	***	*	***	***	ns	ns	***	*	***	***	

Table 2.1: Significance of RMS shown in the graph in Figure 2.3B. Significance notation is as follows * signifies $p \leq 0.05$, ** signifies $p \leq 0.01$, *** signifies $p \leq 0.001$, and ns signifies $p \geq 0.05$.

Figure 2.3A shows a visual rendering of the topography captured from the AFM analysis of representative samples; **Figure 2.3B** shows the corresponding surface roughness. AuKTN, iKTN, and mKTN are significantly rougher than pTi, whereas gKOS is not significantly different. In general, KTN surfaces show more regular structure than the KOS substrate, with the possible exception of iKTN. Several defects are apparent in the silane only coatings, which appear altered by the protein coatings.

2.4.4 Contact Angle

All of the substrates averaged below 90° , which is considered to be hydrophilic. The measured angles do not vary significantly from each other, but several differ from pure titanium as indicated.

2.4.5 Enzyme Degradation

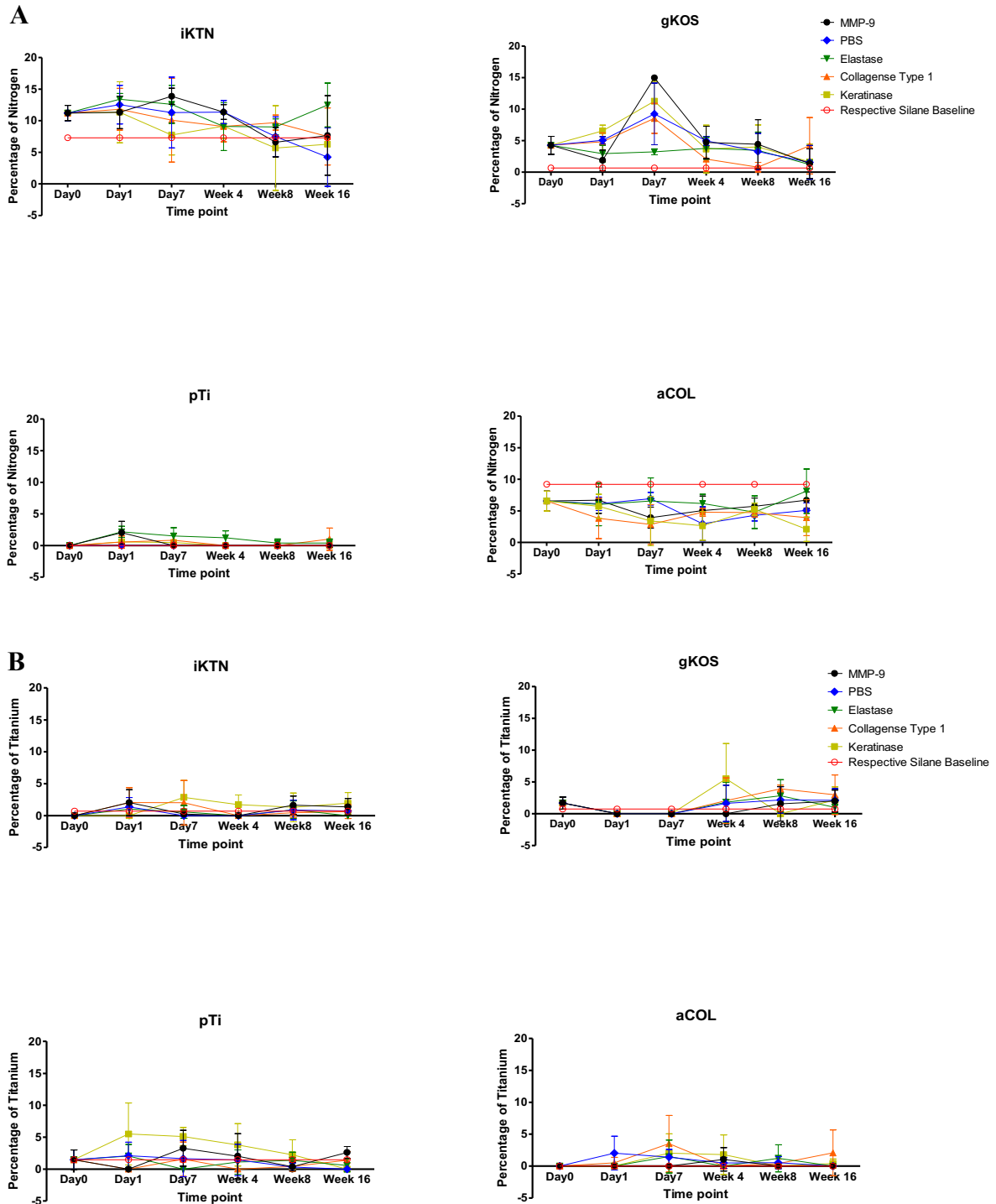


Table 2.2. Degradation Regression for Nitrogen.

Nitrogen						
		Keratinase	Collagenase Type 1	Elastase	PBS	MMP-9
aCOL	slope	-0.02501	-0.004646	0.01065	-0.01441	0.007063
Slope is not significant p=0.3841						
gKOS	slope	-0.0493	-0.2211	-0.01884	-0.04152	-0.04558
Slope is not significant p=0.6669						
iKTN	slope	-0.04224	-0.03127	-0.004683	-0.07018	-0.04756
Slope is not significant p=0.2109						
pTi	slope	-0.003298	0.003979	-0.008486	-	-0.00704
Slope is not significant p=0.3882						

Table 2.3. Degradation Regression for Titanium.

Titanium						
		Keratinase	Collagenase Type 1	Elastase	PBS	MMP-9
aCOL	slope	-0.003446	0.006161	-0.001384	-0.01001	-0.0006619
Slope is not significant p=0.9083						
gKOS	slope	0.008215	0.02598	0.007553	-0.00499	-0.003549
Slope is not significant p=0.8378						
iKTN	slope	0.009552	-0.006582	-0.003091	0.003386	0.007165
Slope is not significant p=0.7126						
pTi	slope	-0.0358	0.002647	-0.005078	-0.01716	0.006474
Slope is not significant p=0.090806						

Degradation of the coatings was assessed by removing samples from enzyme solution and quantifying elemental content by XPS. In general, signals are low in all samples but there are obvious differences between the nitrogen (i.e. indicates protein present) and titanium (i.e. indicates no protein present) signals (**Figure 2.4**), suggesting that the coatings were not completely removed by the enzyme. It could be postulated that a compact protein coating could foster these results. Only one KTN substrate was observed and mKTN was eliminated due to the high variation in MP TES silane for the XPS analysis. aCOL was substituted for aFN because of its specific enzyme

cleavage points common to enzymes found in the skin. A method was used that normalizes aCOL, gKOS and iKTN's slope to pTi's slope, then comparatively ranking substrates within an enzyme category for each element from highest to lowest degradation, then combining nitrogen and titanium rankings and further ranking substrates from highest to lowest. From this system, the data suggest that gKOS degrades the fastest, followed by iKTN, then aCOL under the experimental conditions employed.

2.4.6 Adhesion Motif Detection

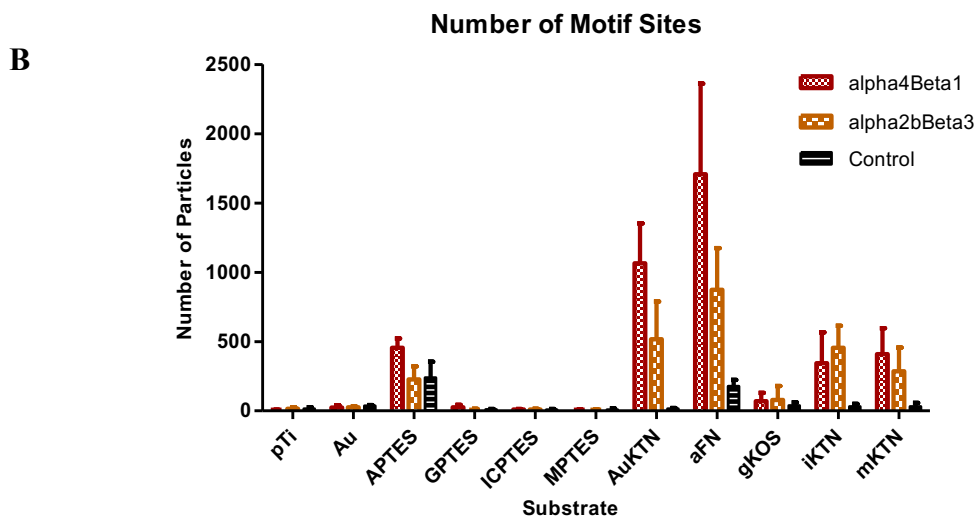
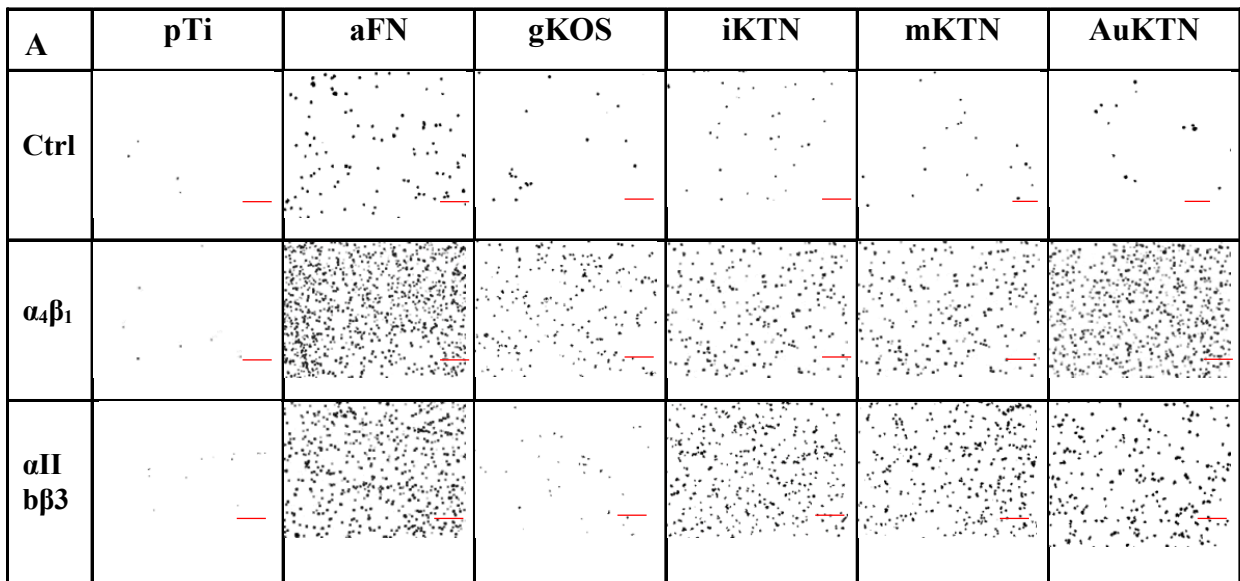


Figure 2.5. Motif Sites. (A) Images of antibody-conjugated fluorophores attached to test substrates, binary images were created in Image J for better visualization and the scale bar represents 50 μ m. (B) Graphical representation of the number of motif sites.

Table 2.4: Significance of the number of motif sites. Significance notation is as follows * signifies $p \leq 0.05$, ** signifies $p \leq 0.01$, *** signifies $p \leq 0.001$, and ns signifies $p \geq 0.05$.

Substrate	Particle Attachment	pTi	Au	APTES	GPTES	ICPTES	MPTES
pTi	Control (No Antibody)		ns	ns	ns	ns	ns
	$\alpha 4\beta 1$		ns	**	ns	ns	ns
	$\alpha IIb\beta 3$		ns	ns	ns	ns	ns
aFN	Control	ns	ns	ns	ns	ns	ns
	$\alpha 4\beta 1$	***	***	***	***	***	***
	$\alpha IIb\beta 3$	***	***	***	***	***	***
AuKTN	Control	ns	ns	ns	ns	ns	ns
	$\alpha 4\beta 1$	***	***	***	***	***	***
	$\alpha IIb\beta 3$	ns	**	ns	***	***	***
gKOS	Control	ns	ns	ns	ns	ns	ns
	$\alpha 4\beta 1$	ns	ns	*	ns	ns	ns
	$\alpha IIb\beta 3$	ns	ns	ns	ns	ns	ns
iKTN	Control	ns	ns	ns	ns	ns	ns
	$\alpha 4\beta 1$	*	ns	ns	ns	*	*
	$\alpha IIb\beta 3$	**	**	ns	**	**	**
mKTN	Control	ns	ns	ns	ns	ns	ns
	$\alpha 4\beta 1$	**	*	ns	*	*	*
	$\alpha IIb\beta 3$	ns	ns	ns	ns	ns	ns

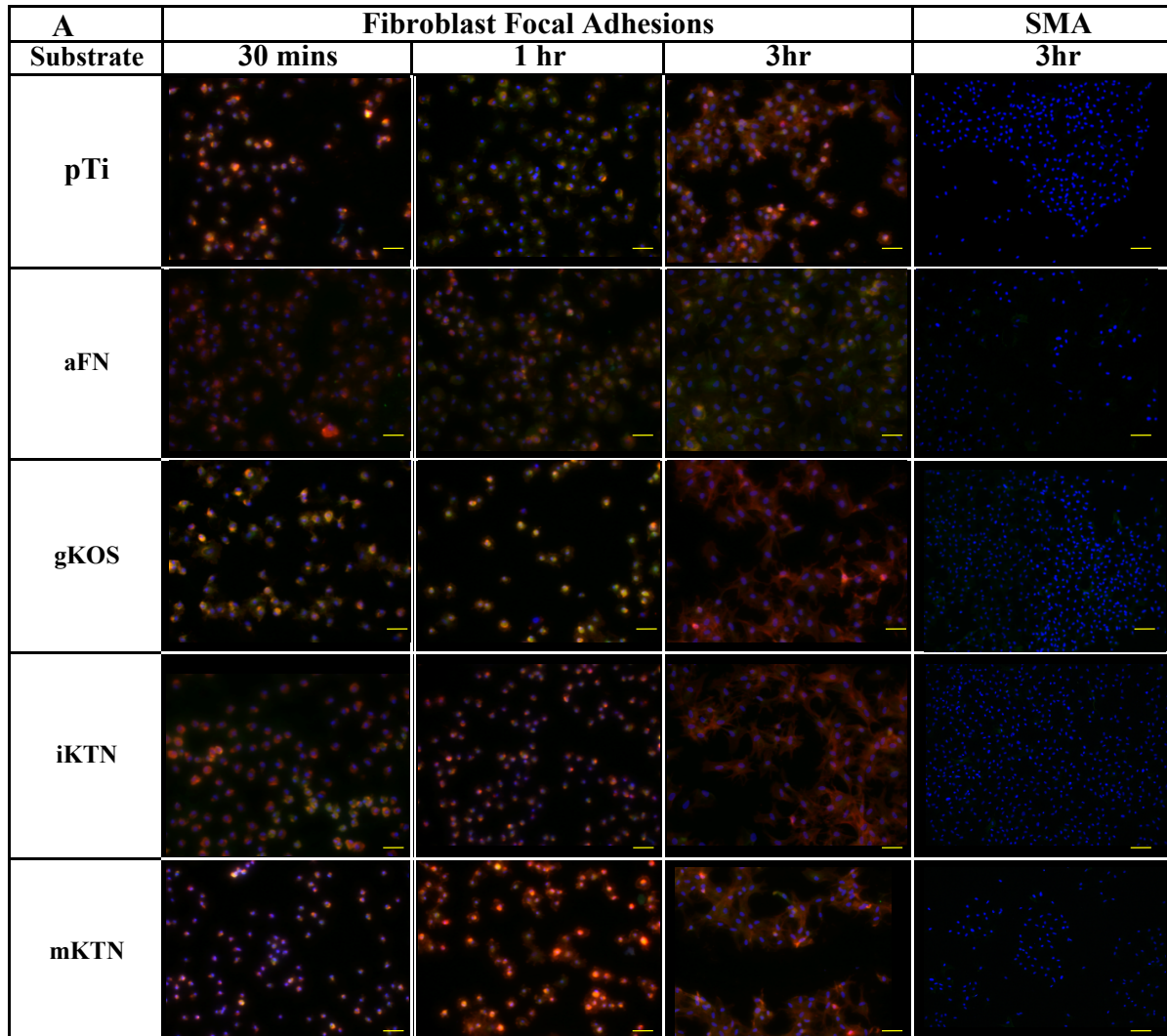
Table 2.5: Significance of the median distance of motif sites. Significance notation is as follows * signifies $p \leq 0.05$, ** signifies $p \leq 0.01$, *** signifies $p \leq 0.001$, and ns signifies $p \geq 0.05$.

Substrate	Particle Attachment	pTi	Au	APTES	GPTES	ICPTES	MPTES
pTi	Control (No Antibody)		ns	**	ns	*	ns
	$\alpha 4\beta 1$		**	***	ns	ns	ns
	$\alpha IIb\beta 3$		ns	ns	ns	ns	ns
aFN	Control	**	ns	ns	**	***	***
	$\alpha 4\beta 1$	***	**	ns	***	***	***
	$\alpha IIb\beta 3$	ns	*	ns	**	**	**
AuKTN	Control	ns	ns	ns	ns	***	ns
	$\alpha 4\beta 1$	***	*	ns	***	***	***
	$\alpha IIb\beta 3$	ns	ns	ns	*	**	*
gKOS	Control	ns	ns	ns	ns	***	ns
	$\alpha 4\beta 1$	***	ns	ns	**	**	***
	$\alpha IIb\beta 3$	ns	ns	ns	ns	ns	ns
iKTN	Control	ns	ns	ns	ns	**	ns
	$\alpha 4\beta 1$	***	ns	ns	***	***	***
	$\alpha IIb\beta 3$	ns	*	ns	**	**	*
mKTN	Control	ns	ns	*	ns	**	ns
	$\alpha 4\beta 1$	***	*	ns	***	***	***
	$\alpha IIb\beta 3$	ns	ns	ns	*	*	*

Keratin contains the adhesion motif leucine-aspartic acid-valine (LDV)⁴⁰, which has been postulated to be the primary source of integrin-mediated adhesion. To investigate the presence of integrin binding ligands on KN coatings, fluorescent spheres were passively attached to human recombinant $\alpha 4\beta 1$ and $\alpha IIb\beta 3$ integrin proteins and the number of punctate adhesions quantified and compared to that for the silane coupling layer used with that particular keratin (Table 3 & 4). Images show the number of adhered spheres (**Figure 2.4A**), which was quantified for each substrate and is shown in the graph (**Figure 2.4B**). Images showing punctate fluorescence suggest that binding motifs are present and concentrated to specific locations, and controls of spheres with no antibody demonstrate that the binding is specific for a given integrin. $\alpha 4\beta 1$ adheres significantly

to both KTN and aFN coatings, but not the KOS when compared to their underlying silane layer. Notably, α Ib β 3, an integrin not known for binding to keratins, adheres both to aFN and KTN substrates. Again, there is not an appreciable binding to KOS.

2.4.7 Focal Adhesion Immunochemistry



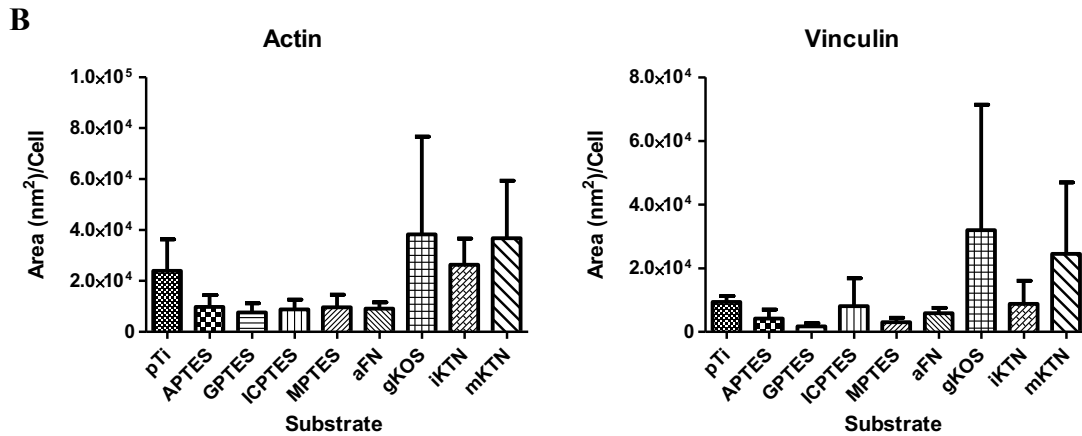
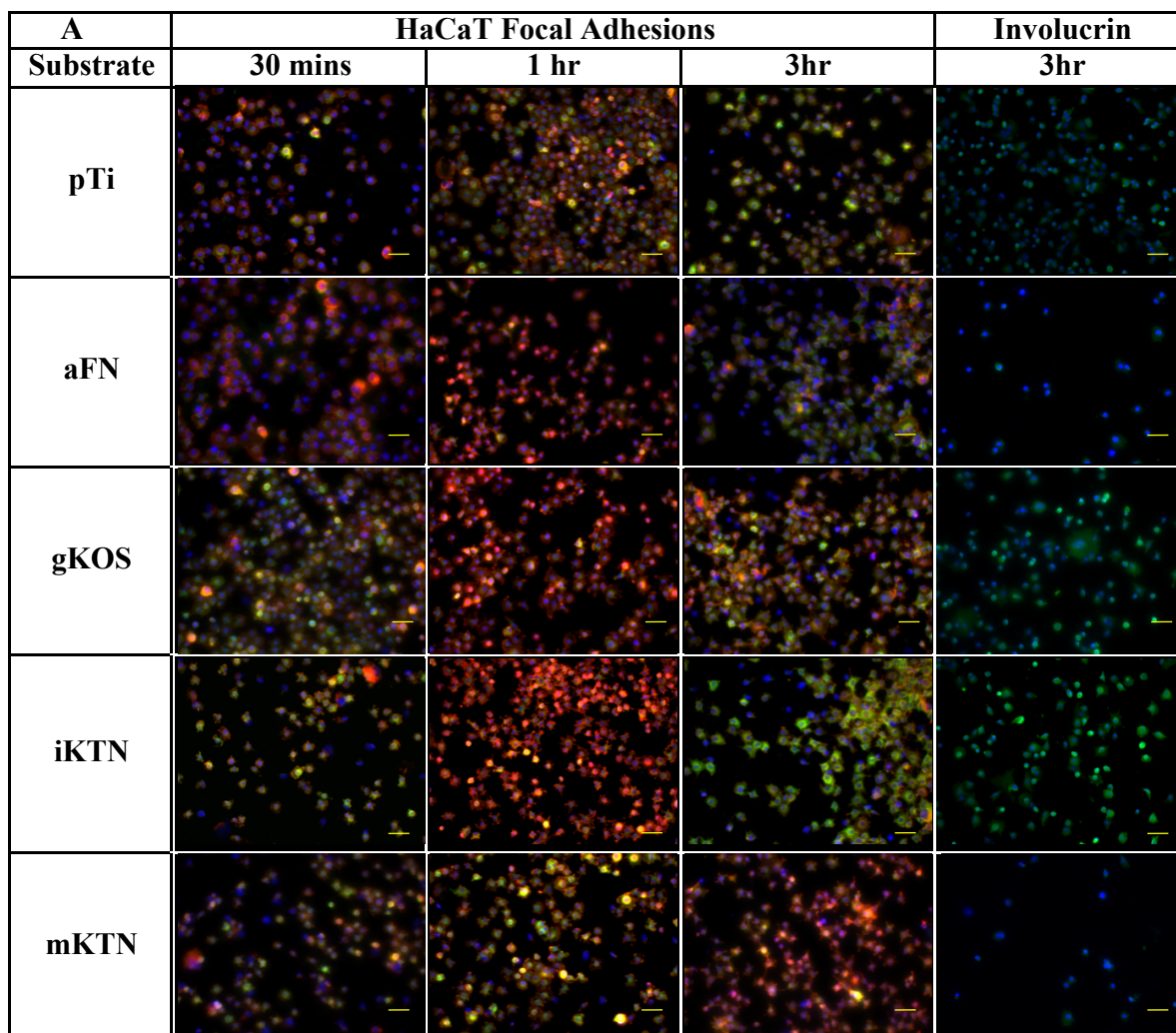


Figure 2.6. Fibroblast Focal Adhesion and SMA Immunocytochemistry. (A) Red (Actin), green (vinculin), blue (nucleus) are represented for fibroblast focal adhesion on the listed substrates. SMA antibody is represented with green and the nucleus is represented with blue. (B) Graphical representation of actin and vinculin at 3 hours incubation as stained area/cell. Scale bars represent 50 μm .

Cellular focal adhesions were examined to give observation to the underlying surfaces biocompatibility. At the 30-minute time point, fibroblasts appear to have a rounded shape on all substrates (**Figure 2.6**). There are subtle differences in the area per cell when observing actin and vinculin via ImageJ, but this data confirms cells will initially adhere to plain titanium, silane couplings, and keratin coated substrates. At one hour, cells on aFN and silane coupling have become enlarged and demonstrate a flattened morphology, whereas cells on iKTN are starting to develop filopodia and are spreading. Cells at the 3-hour time point are fully spread, but due to the media free conditions, the cell densities on all substrates have decreased because cells were no longer provided the proper nutrients. On all keratin substrates, the cell morphology is branched compared to the silane coatings, pTi, and aFN where cells are in a polygonal shape. Interestingly, the topographies in **Figure 2.6A** for gKOS, mKTN, and iKTN are all significantly different from

each other but result in similar branched cell morphologies. The fibroblasts demonstrate diffuse focal adhesion protein localization and seem dominated by actin fibers.



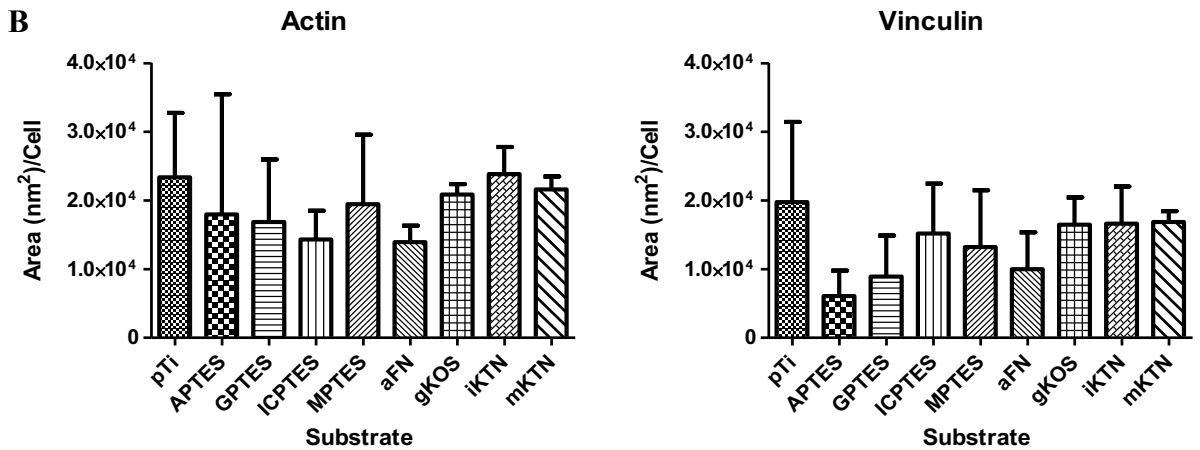


Figure 2.7. HaCaT Focal Adhesions and Involucrin Immunocytochemistry. (A) Red (Actin), green (vinculin), and blue (nucleus) are shown to identify HaCaT adhesion on the listed substrates. Involucrin antibody is represented with green and the nucleus is represented with blue in the far right column. (B) Graphical representation of actin and vinculin at 3 hours of incubation as stained area/cell. Scale bars represent 50 μm .

HaCaT cells adhered well to all substrates, but there does appear to be differences in staining intensity, localization, and shape (Figure 7). For 30 minutes and one hour of incubation, all substrates display punctate adhesions, but gKOS, iKTN, and mKTN are still punctate at the 3-hour time point. Although the body of the HaCaT cells is more rounded compared to fibroblasts, they still exhibit branched filopodia on the keratin substrates.

2.4.8 SMA and Involucrin Analysis

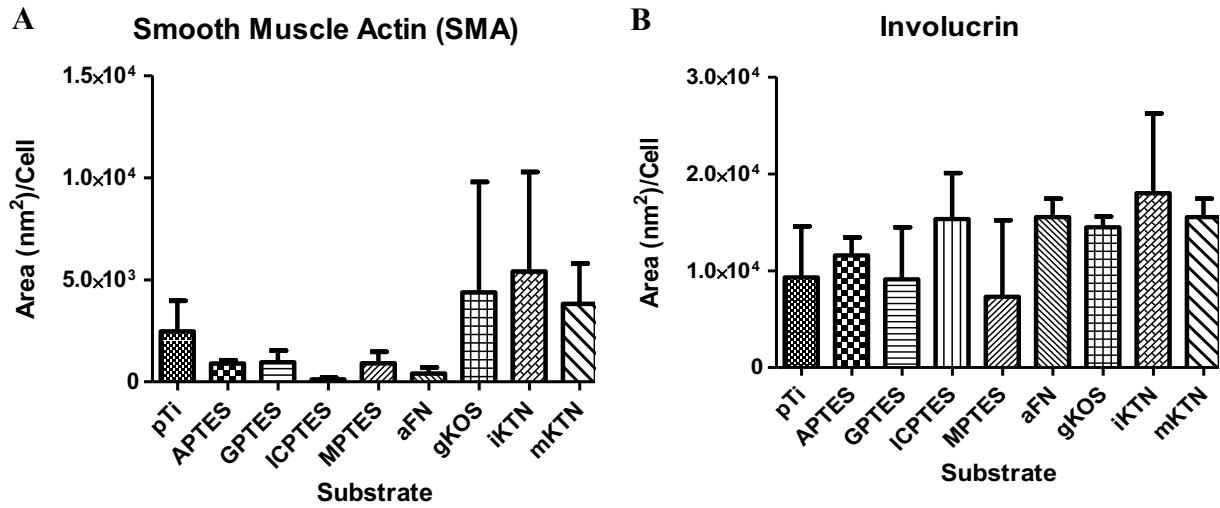


Figure 2.8. SMA and Involucrin. (A) A graphical representation of area/cell for SMA fluorescence. (B) A graphical representation of area/cell for SMA fluorescent.

There is only slight staining of SMA in fibroblasts on all substrates at all time points (Figure 2.6 & 2.8), suggesting that the cells have not shown any indication of becoming myofibroblast. HaCaT cells on iKTN substrate had the largest area per cell of positive involucrin staining, closely followed by gKOS and mKTN substrates, suggesting a lack of a wound healing response on these substrates.

2.5 Discussion

POPs have the potential to advance prosthetic care due to their improved biomechanical loading⁴, increased quality of life for patients⁴¹, and enhancement of gait for the patient¹⁰. Although POP technology shows promise, adverse reactions to POPs restrict their ability to serve as the standard of care for prosthesis attachment. The skin-titanium and other soft tissue percutaneous interfaces are strongly influenced by the foreign body response, wherein chronic inflammation, cell proliferation, and fibrous encapsulation are prevalent and lead to failure^{42,43}. These negative outcomes can lead to repeated infections, weak cell attachment, which can lead to interface tearing

under mechanical loading, and ultimately, implant removal. The introduction of various technologies to mitigate failures have consisted of adhesive peptides or ECM coatings^{21,23,25}, antibacterial coatings^{34,44}, and porous coatings with varying pore size to increase cell attachment to titanium implants^{29,30,32}. The primary focus of these investigations is to create an interface that allows for an attenuated inflammatory response, improved biocompatibility and strengthened cellular attachment, but limited success had been achieved by current endeavors.

Not only can POP technology potentially improve amputees' quality of life, but recent interest in the brain-computer interface has led to further discussion about soft tissue-implant interfaces specifically for neural prosthetics. While developments within the electrical engineering arena have made some strides in neural prosthetics and other brain implant function^{13,14}, the interface between neuronal cells and percutaneous implants is similarly challenging⁴⁵. Experiences with soft tissue integration have proven challenging for continuous glucose sensors and indwelling catheters as well, as a general lack of sustainable cell adhesion to medical device surfaces limits advancement on a number of fronts.

Antibacterial coatings have attempted to reduce infections both through passive and active antibiotic release. However, coatings proved to be short-lived⁴⁴ and only intended for immediate postoperative use. These coatings have created an unintended antibiotic resistance in the host and are usually only developed to provide efficacy against a narrow spectrum of bacterium, which is not ideal for clinical application⁴⁴. Keratin-chitosan films⁴⁶ and other keratin derived biomaterials have displayed antibacterial qualities^{47,48}. Capitalizing on keratin's innate antimicrobial and self-assembly ability may potentially allow keratin coatings to have increased stability and effectiveness over a clinically meaningful time frame.

To assess the coating techniques, such as XPS and AFM provide information about the state of the keratin coating once deposited on a silane. Sulfur is a defining element for keratin, but cysteines only represents 2-5% of keratin⁴⁹. Nitrogen is an element that exist in a large quantity in all proteins and therefore is used to identify the presence of protein on the substrates. In this context, **Figure 2.2A** it is shown that all protein coatings are significantly different from pTi except gKOS. Both iKTN and mKTN are significantly different than their respective silane whereas gKOS and aFN are not. The Ti data in **Figure 2.2B** shows iKTN, gKOS, and aFN have no trace of the Ti observed, however gKOS does. This could suggest that the gKOS coating is not completely uniform or the coating is too thin to be fully detected by the XPS's and cannot adequately be analyzed with this instrument.

To that end, ECM and other protein systems have been crosslinked to help improve mechanical stability against degradation while maintaining a natural capacity for cell adhesion. Glutaraldehyde (GA) is an effective protein crosslinker used to enhance coating stability. GA crosslinked Cultrex[®] basement membrane extract was investigated as a continuous glucose sensor coating compared to non-crosslinked Cultrex[®]. Crosslinked Cultrex[®] demonstrated an extended lifespan for up to three weeks, but only delayed the start of the foreign body response, which appeared after the coating was depleted⁵⁰. A GA crosslinked collagen and chitosan scaffold persisted for 28 days *in vivo* and resisted collagenase *in vitro* for 50 hours with less than 10% degraded, but further long-term studies have yet to be explored⁵¹. In an effort to avoid the toxicity from GA crosslinking but improve mechanical stability, UV photo-crosslinked dextran and collagen-based hydrogel were investigated⁵². Although initial bench tests were promising, the approach proved unsuccessful when the hydrogels were implanted *in vivo*. In the present study, KN coatings exhibited long-term stability in the presence of varying enzymes for longer than 28

days, despite the enzyme concentration being supraphysiologic. One advantage that keratins may have over conventional protein coatings is that humans do not produce keratinases, and other tissue turnover enzymes are only modestly effective.

Still, other approaches have focused on cell adhesion, as opposed to drug delivery and degradation resistance, and may hold the most potential for success as long-term cell attachment has been validated as a significant contributing factor to a stable interface. The use of adhesive peptides sequences has been investigated to promote integrin-mediated cell adhesion. In an *in vitro* study where RGD peptide was bound to a collagen used for coating, results showed no increase in HaCaT cell attachment, with the investigators noting high integrin selectivity as a potential mode of failure⁵³. Other uses of adhesive peptides focused on osseointegration, bone formation, and bone cell differentiation^{23,27} leaving a gap in research for soft tissue-implant integration. Keratin films and coatings previously showed a high degree of cell adhesion, which is assumed to be mediated through the LDV motif^{40,54}, but cells with no specificity to the LDV adhesive peptide have also been observed to adhere⁵⁵. KN coatings showed similar results to fibronectin with suitable cell adhesion for fibroblast and keratinocytes. Comparable cell adhesion to fibronectin was not anticipated but the lack of a statistically significant difference suggests our KN coatings are at least comparable to one well-known cell adhesive protein.

The natural mineral, hydroxyapatite⁵⁶, and ECM proteins such as collagen²¹ and laminin²⁵ have also been used as coatings and demonstrated increased cell adhesion over bare titanium substrates. However, these coatings showed detrimental skin overgrowth and the studies did not include functional cellular assays that would demonstrate skin homeostasis. Along with cell adhesion, HaCaT cells on KN coatings expressed involucrin, an early marker of keratinocyte

terminal differentiation, providing evidence the cells are trending toward a keratinized skin envelope.

2.6 Conclusions

In humans, keratin provides a robust interface between the fingernail and skin. Our initial attempt to exploit this phenomenon by using extracted/purified keratin to coat titanium and attach skin component cells proved successful in that the coating appeared robust in a simulated supraphysiologic environment and provided for cell attachment through focal adhesion formation, which appeared to foster a quiescent biologic response. These findings provide support for undertaking animal studies in which the response of skin to a keratin coated titanium implant can be more closely investigated under more clinically-relevant conditions.

2.7 Acknowledgements

The authors would like to thank the following funding sources: Department of Defense Congressionally Directed Medical Research Programs (CDMRP), grant number W81XWH-15-1-0343; and Virginia Tech-Initiative for Maximizing Student Development (IMSD), grant number R25GM072767-10. We also thank Dr. Alan Esker and Candace Wall for access and training on the goniometer. We provide thanks to undergraduates Kevin Tong, Aaron Giuffre, and Kyle Brown for assisting on this project. In addition, we thank Stephen McCartney and Jay Tuggle for training on the AFM and XPS respectively, and access to the Nanoscale Characterization and Fabrication Lab (NCFL). The authors are also thankful to the Van Dyke lab group, in particular Michele Waters, Marc Thompson, and Nils Potter for their assistance, and our grant collaborators, Dr. Sujee Jeyapalina, and Brian Bennett at the University of Utah for assistance in implementing the HaCaT cell assays, involucrin staining technique, and providing the HaCaT cells.

2.8 References

1. von Recum, A. F. Applications and failure modes of percutaneous devices: a review. *J. Biomed. Mater. Res.* **18**, 323–336 (1984).
2. Gerritsen, M. Problems associated with subcutaneously implanted glucose sensors. *Diabetes Care* (2000). at <http://go.galegroup.com/ps/i.do?p=AONE&sw=w&issn=01495992&v=2.1&it=r&id=G ALE%7CA59650593&sid=googleScholar&linkaccess=fulltext>
3. Fisher, L. E. *et al.* Biomaterial modification of urinary catheters with antimicrobials to give long-term broadspectrum antibiofilm activity. *J. Control. Release* **202**, 57–64 (2015).
4. Mak, A. F. T., Zhang, M. & Boone, D. A. State-of-the-art research in lower-limb prosthetic biomechanics-socket interface. *J Rehabil Res Dev* **38**, 161–173 (2001).
5. Hagberg, K. & Brånemark, R. One hundred patients treated with osseointegrated transfemoral amputation prostheses—rehabilitation perspective. *J Rehabil Res Dev* **46**, 331–344 (2009).
6. Pezzin, L. E., Dillingham, T. R., MacKenzie, E. J., Ephraim, P. & Rossbach, P. Use and satisfaction with prosthetic limb devices and related services. *Arch. Phys. Med. Rehabil.* **85**, 723–729 (2004).
7. Ziegler-Graham, K., MacKenzie, E. J., Ephraim, P. L., Travison, T. G. & Brookmeyer, R. Estimating the Prevalence of Limb Loss in the United States: 2005 to 2050. *Arch. Phys. Med. Rehabil.* **89**, 422–429 (2008).
8. Sullivan, J., Uden, M., Robinson, K. P. & Sooriakumaran, S. Rehabilitation of the trans-femoral amputee with an osseointegrated prosthesis: The United Kingdom experience. *Prosthet. Orthot. Int.* **27**, 114–120 (2003).
9. Tsikandylakis, G., Berlin, Ö. & Brånemark, R. Implant Survival, Adverse Events, and Bone Remodeling of Osseointegrated Percutaneous Implants for Transhumeral Amputees. *Clin. Orthop. Relat. Res.* **472**, 2947–2956 (2014).
10. Farrell, B. J., Prilutsky, B. I., Kistenberg, R. S., Dalton, J. F. & Pitkin, M. An animal model to evaluate skin–implant–bone integration and gait with a prosthesis directly attached to the residual limb. *Clin. Biomech.* **29**, 336–349 (2014).
11. Holt, B. M. *et al.* Pig dorsum model for examining impaired wound healing at the skin-implant interface of percutaneous devices. *J. Mater. Sci. Mater. Med.* **24**, 2181–2193 (2013).
12. Juhnke, D.-L., Beck, J. P., Jeyapalina, S. & Aschoff, H. H. Fifteen years of experience with Integral-Leg-Prosthesis: Cohort study of artificial limb attachment system. *JRRD* **52**, (1999).
13. Tyler, D. J. Neural interfaces for somatosensory feedback. *Curr. Opin. Neurol.* **28**, 574–581 (2015).
14. Schiefer, M., Tan, D., Sidek, S. M. & Tyler, D. J. Sensory feedback by peripheral nerve stimulation improves task performance in individuals with upper limb loss using a myoelectric prosthesis. *J. Neural Eng.* **13**, 16001 (2016).
15. Jansen, J. A., Paquay, Y. G. C. J. & van Der Waerden, J. P. C. M. Tissue reaction to soft-tissue anchored percutaneous implants in rabbits. *J. Biomed. Mater. Res.* **28**, 1047–1054 (1994).
16. Heaney, T. G., Doherty, P. J. & Williams, D. F. Marsupialization of percutaneous

- implants in presence of deep connective tissue. *J. Biomed. Mater. Res.* **32**, 593–601 (1996).
17. Holgers, K.-M., Esposito, M., Källtorp, M. & Thomsen, P. in 513–560 (Springer, Berlin, Heidelberg, 2001). doi:10.1007/978-3-642-56486-4_16
 18. Shekaran, A. & García, A. J. Extracellular matrix-mimetic adhesive biomaterials for bone repair. *J. Biomed. Mater. Res. Part A* **96**, 261–272 (2011).
 19. Parsons, J. T., Horwitz, A. R. & Schwartz, M. A. Cell adhesion: integrating cytoskeletal dynamics and cellular tension. *Nat. Rev. Mol. Cell Biol.* **11**, 633–643 (2010).
 20. Palecek, S. P., Loftus, J. C., Ginsberg, M. H., Lauffenburger, D. A. & Horwitz, A. F. Integrin–ligand binding properties govern cell migration speed through cell–substratum adhesiveness.
 21. Rammelt, S. *et al.* Coating of titanium implants with type-I collagen. *J. Orthop. Res.* **22**, 1025–1034 (2004).
 22. Jansen, J. A., Van Der Waerden, J. P. C. M. & De Groot, K. Wound-healing phenomena around percutaneous devices implanted in rabbits. *J. Mater. Sci. Mater. Med.* **1**, 192–197 (1990).
 23. Ferris, D. . *et al.* RGD-coated titanium implants stimulate increased bone formation in vivo. *Biomaterials* **20**, 2323–2331 (1999).
 24. Reyes, C. D., Petrie, T. A., Burns, K. L., Schwartz, Z. & García, A. J. Biomolecular surface coating to enhance orthopaedic tissue healing and integration. *Biomaterials* **28**, 3228–3235 (2007).
 25. Gordon, D. J., Bhagawati, D. D., Pendegrass, C. J., Middleton, C. A. & Blunn, G. W. Modification of titanium alloy surfaces for percutaneous implants by covalently attaching laminin. *J. Biomed. Mater. Res. Part A* **9999A**, NA-NA (2010).
 26. Sovak, G., Weiss, A. & Gotman, I. Osseointegration of Ti6Al4V alloy implants coated with titanium nitride by a new method. *Bone Joint J.* **82–B**, (2000).
 27. Petrie, T. A. *et al.* The effect of integrin-specific bioactive coatings on tissue healing and implant osseointegration. *Biomaterials* **29**, 2849–2857 (2008).
 28. Mitchell, S. J., Jeyapalina, S., Nichols, F. R., Agarwal, J. & Bachus, K. N. Negative pressure wound therapy limits downgrowth in percutaneous devices. *Wound Repair Regen.* **24**, 35–44 (2016).
 29. Chehroudi, B. & Brunette, D. M. Subcutaneous microfabricated surfaces inhibit epithelial recession and promote long-term survival of percutaneous implants. *Biomaterials* **23**, 229–237 (2002).
 30. Farrell, B. J. *et al.* Effects of pore size, implantation time, and nano-surface properties on rat skin ingrowth into percutaneous porous titanium implants. *J. Biomed. Mater. Res. Part A* **102**, 1305–1315 (2014).
 31. Chehroudi, B., Gould, T. R. L. & Brunette, D. M. A light and electron microscopic study of the effects of surface topography on the behavior of cells attached to titanium-coated percutaneous implants. *J. Biomed. Mater. Res.* **25**, 387–405 (1991).
 32. Chehroudi, B., Gould, T. R. L. & Brunette, D. M. The role of connective tissue in inhibiting epithelial downgrowth on titanium-coated percutaneous implants. *J. Biomed. Mater. Res.* **26**, 493–515 (1992).
 33. Calliess, T. *et al.* Antimicrobial surface coatings for a permanent percutaneous passage in the concept of osseointegrated extremity prosthesis. *Biomed. Tech. (Berl).* **57**, 467–71

- (2012).
34. Zhao, L., Chu, P. K., Zhang, Y. & Wu, Z. Antibacterial coatings on titanium implants. *J. Biomed. Mater. Res. Part B Appl. Biomater.* **91B**, 470–480 (2009).
 35. Grosse-Siestrup, C. & Affeld, K. Design criteria for percutaneous devices. *J. Biomed. Mater. Res.* **18**, 357–382 (1984).
 36. Zhen, L. & Mu, B. *Ben Cao Gang Mu. Jilin, China* (The Time Literature & Art Press, 2005). at https://scholar.google.com/scholar?hl=en&q=Zhen%2C+L.S.+Ben+Cao+Gang+Mu+2005&btnG=&as_sdt=1%2C47&as_sdt=>
 37. de Guzman, R. C. *et al.* Mechanical and biological properties of keratose biomaterials. *Biomaterials* **32**, 8205–8217 (2011).
 38. Perrin, C., Langbein, L. & Schweizer, J. Expression of hair keratins in the adult nail unit: an immunohistochemical analysis of the onychogenesis in the proximal nail fold, matrix and nail bed. *Br. J. Dermatol.* **151**, 362–371 (2004).
 39. Van Dyke, M. & Rahmany, M. Keratin Nanomaterials and Methods of Production. (2015). at <https://www.google.com/patents/US20170051027>
 40. Tachibana, A., Furuta, Y., Takeshima, H., Tanabe, T. & Yamauchi, K. Fabrication of wool keratin sponge scaffolds for long-term cell cultivation. *J. Biotechnol.* **93**, 165–170 (2002).
 41. Hagberg, K., Häggström, E., Uden, M. & Brånemark, R. Socket versus bone-anchored trans-femoral prostheses: hip range of motion and sitting comfort. *Prosthet. Orthot. Int.* **29**, 153–163 (2005).
 42. Anderson, J. M., Rodriguez, A. & Chang, D. T. Foreign body reaction to biomaterials. *Semin. Immunol.* **20**, 86–100 (2008).
 43. Affeld, K., Grosshauser, J., Goubergits, L. & Kertzsch, U. Percutaneous devices: a review of applications, problems and possible solutions. *Expert Rev. Med. Devices* **9**, 389–399 (2012).
 44. Stavrakis, A. I. *et al.* In Vivo Efficacy of a “Smart” Antimicrobial Implant Coating. *J. Bone Joint Surg. Am.* **98**, 1183–9 (2016).
 45. Polikov, V. S., Tresco, P. A. & Reichert, W. M. Response of brain tissue to chronically implanted neural electrodes. *J. Neurosci. Methods* **148**, 1–18 (2005).
 46. Tanabe, T., Okitsu, N., Tachibana, A. & Yamauchi, K. Preparation and characterization of keratin-chitosan composite film. *Biomaterials* **23**, 817–825 (2002).
 47. Sundaram, M. & Banu, A. N. A Study on Anti Bacterial Activity of Keratin Nanoparticles from Chicken Feather Waste Against Staphylococcus aureus (Bovine Mastitis Bacteria) and its Anti Oxidant Activity. *Eur. J. Biotechnol. Biosci.* **~ 1**, 1–5 (2015).
 48. Park, M. *et al.* Novel preparation and characterization of human hair-based nanofibers using electrospinning process. *Int. J. Biol. Macromol.* **76**, 45–48 (2015).
 49. Strnad, P., Usachov, V., Debes, C., Gräter, F. & Parry, D. Unique amino acid signatures that are evolutionarily conserved distinguish simple-type, epidermal and hair keratins. *J Cell Sci* (2011). at <http://jcs.biologists.org/content/124/24/4221.short>
 50. Klueh, U., Ludzinska, I., Czajkowski, C., Qiao, Y. & Kreutzer, D. L. Crosslinked basement membrane-based coatings enhance glucose sensor function and continuous glucose monitoring *in vivo*. *J. Biomed. Mater. Res. Part A* (2017). doi:10.1002/jbm.a.36206

51. Ma, L. *et al.* Collagen/chitosan porous scaffolds with improved biostability for skin tissue engineering. *Biomaterials* **24**, 4833–4841 (2003).
52. Zhang, Y., Zhang, X., Xu, L., Wei, S. & Zhai, M. Radiation cross-linked collagen/dextran dermal scaffolds: effects of dextran on cross-linking and degradation. *J. Biomater. Sci. Polym. Ed.* **26**, 162–180 (2015).
53. Roessler, S. *et al.* Biomimetic coatings functionalized with adhesion peptides for dental implants. *J. Mater. Sci. Mater. Med.* **12**, 871–877 (2001).
54. Reichl, S. Films based on human hair keratin as substrates for cell culture and tissue engineering. *Biomaterials* **30**, 6854–6866 (2009).
55. Burnett, L. R. *et al.* Hemostatic properties and the role of cell receptor recognition in human hair keratin protein hydrogels. *Biomaterials* **34**, 2632–40 (2013).
56. Jansen, J. A., van der Waerden, J. P. & de Groot, K. Tissue reaction to bone-anchored percutaneous implants in rabbits. *J. Invest. Surg.* **5**, 35–44

Chapter 3. A Comparative Study of Recombinant and Extracted Human Hair Keratins

Rachael N. Parker^{1,}, Alexis Trent^{2,*}, Kristina L. Roth¹, Mark E. Van Dyke³, Tijana Z. Grove¹*

1. Department of Chemistry and Macromolecules Innovation Institute, Virginia Tech,
Blacksburg, VA 24060
2. Department of Materials Science and Engineering, Virginia Tech, Blacksburg, VA 24060
3. Department of Biomedical Engineering and Mechanics, Virginia Tech, Blacksburg, VA 24060

(Manuscript in Preparation)

*Authors contributed equally to this work

3.1 Abstract

Natural biopolymers have found success in tissue engineering and regenerative medicine applications. Their intrinsic biocompatibility and biological activity make them well suited for biomaterials development. Specifically, keratin-based biomaterials have shown success in regenerative medicine applications including bone regeneration, wound healing, and nerve regeneration. However, studies of structure-function relationships in keratin biomaterials have been hindered by the lack of homogeneous preparations of materials extracted and isolated from natural sources such as wool and hair fibers. The use of recombinant DNA technology and protein expression presents a potential solution to overcome challenges associated with sample heterogeneity due to the extraction of biopolymers from natural sources. Here we present a side-by-side comparison of natural and recombinant human hair keratin proteins K31 and K81. Human trichocytic keratin biopolymers K31 and K81 were individually expressed in *E. coli* and purified to homogeneity using a combination of metal affinity chromatography and size-exclusion chromatography, resulting in homogeneous solutions. We have used size exclusion chromatography and dynamic light scattering to investigate initial stages of self-assembly in extracted vs. recombinant keratins. When combined, the recombinant proteins (i.e. rhK31 and rhK81) assemble into characteristic intermediate filament-like fibers. Coatings made from natural and recombinant dimers were also compared side-by-side and investigated for coating characteristics and cell adhesion.

KEYWORDS: human hair keratin, biomaterials, recombinant protein, self-assembly, biomimetic coating

3.2 Introduction

Biopolymeric scaffolds for tissue engineering and regenerative medicine have garnered much interest over the past few decades¹⁻¹¹. Natural biopolymers offer several advantages over traditional implant materials and synthetic polymer-based scaffolds. Natural biopolymeric scaffolds are often constructed from proteins found in the extracellular matrix (ECM) and other native tissues, which contributes to their biocompatibility and minimizes undesirable immune responses. Furthermore, many natural biopolymers have inherent self-assembly properties, functional cell binding motifs, and other important regulatory functions, such as control over cell migration and proliferation that provide them with intrinsic biological activity^{6,10,12-16}. Conversely, synthetic polymers provide excellent structural support, but lack the intrinsic biological activity¹⁷ and often elicit an unwanted foreign body response¹⁸. Additionally, synthetic polymers often require chemical modifications in order to improve their biocompatibility and impart biological functions for subsequent use as biomaterials. Functionalization of these scaffolds has proven difficult^{19,20} as it is challenging to control the degree of functionalization and the spatial organization of functional groups^{21,22}. Therefore, natural biopolymers are promising alternatives as biomaterials for regenerative medicine due to their inherent characteristics (e.g. self-assembly, cell binding)²³.

When designing biomaterials for regenerative medicine and tissue engineering, certain criteria should be considered²⁴. First, biomaterials need to provide adequate mechanical and structural support. Second, the ability to facilitate and control cellular adhesion, migration, proliferation and differentiation is essential for successful biomaterial use²⁵. Lastly, materials that degrade over time and resorb into the body allow for temporary implants. The ability to control the rate of degradation further enhances the utility of the material as the degradation rate can be

tailored to the body's healing process²⁶. Biopolymers such as elastin^{16,27}, collagen¹², keratin²⁸, and silk²⁹ have all been used for preparation of biomaterials. These biopolymers are characterized by their hierarchical structures and exquisite and tunable mechanical properties^{15,27,30,31}. Furthermore, important biological functions, including the ability to promote cellular attachment through specific cell-binding motifs in their primary amino acid sequences, induction of cell proliferation, as well as regulation of cellular differentiation and protein synthesis can be imparted in the process of biomaterial design^{27,32-34}.

In the past decade keratin biomaterials have demonstrated utility as a suitable scaffold for tissue engineering and regenerative medicine³⁵⁻⁴⁷. The inherent self-assembly of keratin biopolymers into fibrous nanostructures allows for processing keratins into materials with preferred mechanical properties. Furthermore, keratins' biological and regulatory functions enhance its biocompatibility and provide useful bioactivity. For example, it has been proposed that keratin biopolymers contain cell binding motifs, specifically the leucine-aspartic acid-valine (LDV) motif³⁰, and participate in regulation of protein synthesis, cell growth, and proliferation^{48,49}. Consequently, keratin has been employed in bone regeneration⁵⁰, wound healing⁵¹, and nerve regeneration⁵² applications. A notable example of keratin-based materials demonstrated its utility as a scaffold for bone regeneration through the delivery of recombinant human bone morphogenetic protein 2 (rhBMP-2) via a keratin hydrogel system⁵⁰. Another recent application of keratin-based scaffolds is in drug delivery. Ham et al.⁵³ used human hair keratins to fabricate hydrogels with controlled degradation profiles to allow for delivery of recombinant human insulin-like growth factor 1. However, despite the apparent utility of keratin biomaterials, structure-property relationship investigations have been mired by the lack of homogeneous biopolymer preparations. During extraction from natural sources such as hair and wool fibers, natural keratins

are subject to extensive processing conditions that can lead to biopolymer damage. Additionally, the quality of the materials is highly source dependent. The harsh processing methods required for keratin extraction may result in protein damage leading to alterations in network assembly and undesirable immune response despite the biocompatibility of the biopolymer. Furthermore, major biopolymer components, K31 and K81, co-purify with low molecular weight constituents such as melanin and keratin associated proteins (KAPs).

We have recently reported cloning, expression, and purification of recombinant human hair keratin 31 (K31) and keratin 81 (K81)⁵⁴. K31 and K81 have been identified as the major components of extracted hair keratin materials,⁵⁵ which fall into the category of “hard” keratins. Hard keratins are found in epidermal appendages, such as hair, skin, and nails⁵⁶. The defining feature of hair keratins comes from their high cysteine content, which contain 5% or more cysteine residues⁵⁷. This is a stark contrast to epithelial or “soft” keratins, which contain less than 1% of cysteines⁵⁷. Consequently, hard keratins form more rigid structures, compared to the loose bundles formed by soft keratins, which result from extensive intermolecular disulfide bonds formed during assembly. Keratins extracted from natural sources are obtained either through oxidative extraction (so-called keratose or KOS) or through reductive extraction (so-called kerateine or KTN). In KOS samples, disulfide bonds are not reformed due to the conversion of the cysteine thiol groups to sulfonic acid. KTN, keratin isolated by reductive extraction retain thiol groups, can readily form disulfide crosslinks. As a result of this chemical difference, KOS materials are generally less mechanically stable than KTN materials as there are no covalent bonds formed in the material⁵³. Herein, we present the side-by-side comparison of the solution characterization of recombinant human hair keratins K31 and K81 (rhK31 and rhK81) to KTN. In addition, coatings made from

KTN nanomaterials and dimers of recombinant rhK31 and rhK81 were characterized and tested for their ability to adhere epithelial cells.

3.3 Materials and Methods

3.3.1 Gene Design and Cloning of Recombinant K31 and K81

Amino acid sequences for K31 and K81 were reverse translated to the resultant DNA sequence and optimized for *E. coli* codon usage. Synthetic genes corresponding to each protein sequence were synthesized by GeneWiz Inc. The gene sequence contained restriction sites for subsequent cloning into the expression vector pProExHtam. BamHI and HindIII, at the 5' and 3' ends, were employed to ligate the gene into the plasmid, following digestion and isolation of the gene from the commercial plasmid puc57. Enzymes were purchased from New England Biolabs (Ipswich, MA). In order to confirm successful cloning of each gene, sequencing was completed by the Virginia Tech Bioinformatics Institute, which confirmed the correct gene sequences were contained in the plasmids. The same procedure was followed for cloning of the K31 and K81 genes. Plasmid pProExHtam contains an N-terminal histidine affinity tag to be used for protein purification.

3.3.2 Protein Expression and Purification of Recombinant Proteins

Recombinant K31 and K81 were expressed using an *E. coli* expression system. The same procedures were followed for both proteins. First, the proteins were expressed in BL21 (DE3) *E. coli* cells. Luria Broth (LB) was used for cell cultures. Cells were grown overnight for 16 hours in 50 mL of media at 37°C with shaking at 250 rpm. LB media was then used to dilute the cells in a 1:100 ratio and cells were grown to an optical density (OD) of 0.6-0.8. Once OD had been reached, 1 mM isopropyl β -D-1-thiogalactopyranoside (IPTG) was used to induce protein expression, which was completed at 37°C for 4 hours. Cells were then harvested by centrifugation at 5,000

rpm for 15 minutes and subsequently resuspended in lysis buffer pH 8 containing 50 mM Tris HCl, 300 mM sodium chloride, and 1% Tween 20 and then stored at -80°C until purification. An inclusion body purification procedure adapted from Honda et al⁵⁸. was used to extract and purify rhK31 and rhK81. Cell pellets were thawed in a 37°C water bath followed by a 30 minute incubation with 10 mg/ml of lysozyme. Following this step, 10 mM MgCl₂, 1 mM MnCl₂, and 10 µg/mL of DNase were each added to the protein samples and incubated for an additional 30 minutes. Detergent buffer pH 8 consisting of 20 mM Tris HCl, 200 mM NaCl, 1% Triton X-100, and 2 mM EDTA was then added at an equivalent volume to the sample volume and mixed well before centrifuging for 15 at 5,000 rpm. Following removal of the supernatant, an additional 25 mL of detergent buffer was added to each sample, and the samples were again centrifuged. This procedure was repeated until a tight pellet of inclusion bodies was formed at which time 25 mL of extraction buffer was added. Extraction buffer consists of 10 mM Tris HCl, 2 mM EDTA, 8 M urea, 10 mM βME, and 1 protease inhibitor cocktail tablet at a pH of 8, and was used to resuspend the inclusion body pellet. The samples were then centrifuged for 1 hour at 16,000 rpm. The resultant supernatant containing the extracted keratin proteins was collected for further purification. rhK31 and rhK81 containing an N-terminal histidine affinity tag were purified using a standard Ni-NTA affinity purification procedure. All buffers used for the purification process also contained 8 M urea to keep proteins in their denatured form until further dialysis.

3.3.3 *Keratin Gel Electrophoresis and Western Blot*

Sodium dodecyl sulfate-polyacrylamide gel electrophoresis (SDS-PAGE) was used to separate purified protein prior to Western blot analysis. Samples were prepared in a 1:1 ratio of SDS buffer to protein and analyzed on a 10% acrylamide gel. Extracted KTN was diluted at 10mg/ml in sodium phosphate at pH 7.4, and recombinant proteins were prepared at 5 mg/mL.

The SDS-PAGE electrophoresis was run at 200 V for 40 minutes. Following SDS-PAGE, proteins were transferred onto nitrocellulose membranes at 0.35A for 2 hours. The membranes were blocked with 5% non-fat dry milk in Tris Buffer Saline with 0.25% Tween 20 (TBST) for 1 hour. Guinea pig anti-human keratin-31 (K31) and guinea pig anti-human keratin-81 (K81) antibodies (Progen Biotechnik, Heidelberg, Baden-Württemberg, Germany) were used as primary probes and were both diluted at 1:2000 in blocking buffer for 1 hour. The membranes were washed three times with TBST, submerged into a 1:3000 dilution of the rabbit anti-Guinea pig IgG-HRP (Life Technologies) secondary probe for 1 hour, then again washed three times with TBST. All incubation periods were conducted at room temperature. Pierce ECL Plus substrate (Thermo Fisher Scientific) mix was added to the membranes 3 minutes prior to been imaged in a Fujifilm LAS-3000 Imager (General Electric).

3.3.4 *Dialysis*

Following affinity purification and molecular weight verification by SDS-PAGE and MS analysis, rhK31 and rhK81 were individually dialyzed out of elution buffer pH 8 containing 300 mM NaCl, 50 mM Tris HCl, 300 mM imidazole, 10 mM β ME, and 8 M urea. In the first step of dialysis the protein was dialyzed against buffer pH 8 with 10 mM Na_2HPO_4 , 75 mM NaCl, 5 mM DTT, and 8 M urea. Four additional dialysis steps were completed with decreasing amounts of urea equal to 6, 4, 2, and 0 M. Each of the steps were completed at 3 hour intervals except for the last step, which was allowed to equilibrate overnight. Keratin proteins that were previously extracted and lyophilized were reconstituted and prepared following the same procedure.

3.3.5 *Extraction of Natural Keratin Proteins*

Natural keratins used for this study were extracted as previously described^{59,60}. Briefly, a sample of human Chinese hair was obtained from a commercial vendor and used as received. 100

grams of hair was placed into a 2 L solution of 0.5 M thioglycolic acid (TGA) adjusted to a pH of 10.5 and shaken at 100 rpm for 15 hours at 37°C. The hair was recovered by sieve and the extraction solution retained. The hair fibers were then placed in a solution of 4 L of 100 mM tris base and shaken at 100 rpm for 2 hours at 37°C. Hair was again recovered by sieve and placed in a freshly prepared 1 L solution of 0.5 M TGA adjusted to a pH of 10.5 and shaken at 100 rpm for 15 hours at 37°C. The resulting extraction solution was retained and the hair was then placed in 2 L of 100 mM tris and shaken at 100 rpm for 2 hours at 37°C. The hair was then recovered by sieve and discarded. The extraction solution was retained and pooled with extraction solutions obtained in previous steps to form a solution of crude keratin extract. The crude extract was clarified of particulate matter by centrifugation through a solids separator running at 30,000 rpm, followed by filtration through a filter membrane with a 20-25 µm average pore size. Keratin nanomaterials were obtained from this clarified crude keratin extract by ultrafiltration using a 100 kDa NLMWCO polysulfone, tangential flow filtration (TFF) cartridge. TFF was conducted with 10 volume washes against a buffer consisting of 10 mM disodium phosphate and 100 mM sodium chloride at pH 9.1, followed by 5 volume washes against purified water. The purified keratin nanomaterial solution was concentrated, titrated to pH 8.5, frozen and freeze dried to produce a keratin nanomaterial powder.

3.3.6 *Size Exclusion Chromatography*

A Dionex chromatography system with an Ultimate 3000 UV/Vis detector was used for size exclusion chromatography (SEC). Proteins were detected at 280 nm and analyzed with Chromeleon v6.8 chromatography software. Samples were analyzed following each step of the dialysis process. Each sample was passed through a 0.22 µm filter after a 3 hour equilibration

period in the appropriate dialysis buffer. The mobile phase used for each sample corresponds to the relevant dialysis buffer. Samples were analyzed with a flow rate of 0.5 mL/min.

3.3.7 *Dynamic light scattering*

Dynamic light scattering (DLS) was completed using a Malvern Zetasizer Nano-ZS to analyze the average particle size and size distribution of extracted and recombinant keratin biopolymers in solution. Prior to measurement, samples were filtered using a 0.22 μm filter. Each sample corresponds to steps during the dialysis process, and thus samples contain the corresponding buffer and urea concentration as described in the dialysis section. The Malvern software converts the intensity percent size distribution to volume percent using Mie theory.

3.3.8 *Transmission Electron Microscopy*

Using a Philips EM420 microscope with an accelerating voltage of 120 kV transmission, electron microscopy (TEM) analysis was performed on extracted and recombinant keratin biopolymers. Samples were prepared using 300 mesh carbon-coated grids purchased from Electron Microscopy Science. Following deposition of the sample on the grid, a 1 minute drying period was allowed before excess sample was removed. All samples were stained using 2% uranyl acetate, with a 30 second drying period. Excess stain was then removed and samples were allowed to air-dry for 24 hours prior to analysis.

3.3.9 *Silane Coupling and Protein Deposition*

Microscope slides coated with 5nm of titanium (Deposition Research Lab Inc. CO, USA) were cut into 0.8cm by 0.8cm substrates. These substrates were cleaned with 100% ethanol (EtOH) to remove nominal debris. These pieces were then immersed in silane solutions of 5 % 3-Aminopropyltriethoxysilane (a; APTES; TCI America, Portland, OR, USA) in 95:5 EtOH: H₂O solution (v/v) or 10% 3- Isocyanatopropyltriethoxysilane (i; ICPTES; Acros Organics, Geel,

Belgium) in 100% EtOH (v/v). The silane solution was filtered with a 0.2 μ m pore size, the substrates were then placed in gentle agitation for 3 hours, rinsed with 100% EtOH and rinsed with MilliQ water three times. The substrates were subsequently placed into an oven at 110°C for 30 minutes each.

Silane coated substrates were placed in either extracted KTN or dimerized rhK31 and rhK81 recombinant keratin (rhK) solutions at room temperature (RT) overnight. The KTN solutions were at a 1% concentration and dissolved in 10 mM sodium phosphate at pH 7.4; the rhK was at a concentration of approximately 1 mg/ml in distilled water. Other silane-coated substrates were immersed in human fibronectin (FN; Corning, Corning, NY, USA) at 5 μ g/ml in phosphate saline buffer (PBS) and bovine collagen I (COL; Corning, Corning, NY, USA), which was only used for elemental analysis, was coated at 5 μ g/cm² in 0.01N HCl on silane treated slides. Both FN and COL was coated for 1 hour. Gold substrates (not silane-coated) were coated in 1% KTN (w/v) in 10 mM sodium phosphate at pH 7.4 overnight at RT. All substrates were rinsed with MilliQ water, air dried, and exposed to ultraviolet (UV) light for 1 hour. In subsequent sections, the coatings are noted as iKTN for ICPTES-coupled KTN, AuKTN for gold-coupled KTN, iRhK for ICPTES-coupled recombinant dimer, aFN for APTES-coupled fibronectin, aCOL for APTES-coupled collagen, and pTi for plain titanium. From a previous study conducted in our lab, silane optimization was performed⁶⁰, silane coupling selection for FN and COL was used from published studies⁶¹⁻⁶³.

3.3.10 *Time of Flight Secondary Ion Mass Spectrometry (ToF-SIMS)*

ToF-SIMS analysis was conducted using a ION-TOF TOF.SIMS 5 (ION-TOF GmbH, Münster, Germany) instrument equipped with a Bi_n^{m+} (n = 1 - 5, m = 1, 2) liquid metal ion gun, Cs⁺ sputtering gun and electron flood gun for charge compensation. Both Bi and Cs columns were

angled at 45° with respect to the sample surface normal. Samples were analyzed under vacuum with a chamber pressure maintained below 5.0×10^{-9} mbar to avoid surface contamination. Three spots on each sample were analyzed.

3.3.11 *Atomic Force Microscopy (AFM)*

Dry substrates were examined in tapping mode on the Veeco BioScope II (Oyster Bay, NY) at RT. Five 2 μ m by 2 μ m spots were analyzed per substrate under a silicon tip (Nanosensors, Switzerland) with curvature of 10 nm and a force constant ranging between 10 -130 N/m. Surface roughness (RMS) and rendered images were created and analyzed through with the Bruker's Nanoscope software.

3.3.12 *Cellular Motif Identification*

FluoSpheres Carboxylate-Modified microspheres with a 1 μ m diameter (ThermoFisher, Waltham, MA, USA) were passively attached to recombinant integrins $\alpha 4\beta 1$ (R&D Systems, Minneapolis, MN, USA) and $\alpha 2\beta 3$ (R&D Systems, Minneapolis, MN, USA), under gentle agitation overnight at RT with no light exposure. A 1 mL solution containing 1.0×10^8 of the integrin-coated fluorescent beads was placed on substrates for 3 hours at RT. Samples were then rinsed three times with MilliQ water and observed under 10x using a Zeiss LSM 800 confocal microscope. A custom Matlab code was used to analyze the number spheres and distances between spheres for each image.

3.3.13 *Cell Static Adhesion Immunocytochemistry*

Human neonatal primary dermal fibroblast (PCS-201-010; ATCC, Manassas, VA, USA) were grown in RPMI 1640, L-Glutamine, with no sodium pyruvate (Gibco Life Technologies Carlsbad, CA, USA) with an additional 10 % fetal bovine serum (FBS; Gibco Life Technologies

Rockville, MD, USA) and 1% penicillin streptomycin (P/S) added. Human keratinocytes HaCaT cells (Catalog #T0020001; AddexBio Technologies, San Diego, CA, USA) were cultured in Dulbecco's Modified Eagle's Medium (DMEM; ThermoFisher, Waltham, MA, USA), with 10% FBS, 1% P/S and 1.5mM sodium pyruvate (ThermoFisher, Waltham, MA, USA). All cells were split 1 to 3 every 2-3 days and incubated at 37°C, 5% CO₂.

For immunochemistry assays, fibroblasts and HaCaT cells were seeded at 10,000 cells in a 40 µl in a serum free-droplet onto the substrates and incubated at 37°C for 3 hours, then fixed with 4% paraformaldehyde. Cells were permeabilized, washed, blocked, and focal adhesions (F-actin and vinculin) were stained with the FAK 100 kit according to the manufacture's protocol (EMD Millipore, Billerica, MA, USA). Dilutions of antibodies were as follows: primary antibody Anti-Vinculin (1:350), the secondary Alexa Flour 488 (1:300), Phalloidin (1:350) and DAPI (1:1000). Cells were imaged at 10x using a Zeiss LSM 800 confocal microscope.

3.3.14 *Involucrin Detection*

HaCaT cells were seeded at 10,000 cells/cm² in a 40 µl droplet onto the substrates and incubated at 37°C initially for 3 hours. After 3 hours, a 1 mL solution of media was added and replaced daily for 7 days. For a positive control, HaCaT cells were seeded in high calcium media (2.8mM Ca²⁺). After 7 days of culture, cells were removed using a cell scraper and RIPA buffer. Each whole cell lysate sample and capillary Western blot assay was prepared according to the manufacturer's instructions for the WesTM (ProteinSimple, San Jose, CA, USA). Briefly, cell lysates were prepared with 1 part 5x Fluorescent master mix and 4-part cell lysate, which could be diluted with 0.1x sample buffer, if needed. The ladder is provided but additional sample buffer and dithiothreitol (DTT) is added according to the preparation guideline. Biotinylated ladder and samples were denatured at 95°C for 5 minutes. Samples, blocking reagent, antibody diluent,

primary antibodies, secondary antibodies, streptavidin HRP, wash buffer, and Luminol-peroxide were placed in the provided ProteinSimple well plate. The manufacturer's anti-mouse secondary antibody was used in conjunction with both primary antibodies tested, which included the primary antibody, involucrin (Thermo Fisher, Waltham, MA, USA) (1:1000) and the secondary antibody goat anti-mouse IgG-HRP (1:5000) (Santa Cruz Biotechnology, Dallas, TX, USA). The well plate and one time use capillary insert are placed in the WesTM instrument, where the fully automated process begins. Upon completion, digital images and area peaks were analyzed in ProteinSimple's Compass software.

3.3.15 *Smooth Muscle Actin Detection*

Fibroblasts were seeded at 10,000 cells in a 40 μ l droplet onto the substrates and incubated at 37°C initially for 3 hours. After 3 hours, a 1 mL solution of media was added and replaced daily for 7 days. For the smooth muscle actin positive control, HeLa cells CCL-2 (ATCC, Manassas, VA, USA) were used on a tissue culture substrate. The same procedure for the Wes system, as described above for involucrin, was followed, except that antibodies used included primary antibody, alpha-SMA (1:500) and secondary antibody, goat anti-mouse IgG-HRP (1:5000) (Santa Cruz Biotechnology, Dallas, TX, USA).

3.3.16 *Statistics*

Replicates of ≥ 3 were used in all experiments. Graphs were created in either GraphPad Prism or Microsoft Excel and ANOVA was used for statistical analysis via GraphPad Prism Software. Image J and Photoshop (Adobe, San Jose, CA) were used for image processing and analysis.

3.4 Results and Discussion

Recombinant DNA technology and protein engineering are greatly influencing the next-generation biomaterials landscape. Recombinant protein-based biomaterials provide the structural and mechanical properties of their natural counterparts while offering the potential for creating materials with tunable sequences, and thus tailored and improved characteristics. Cellular binding motifs, degradation sites, and protein fusions exemplify some of the benefits afforded from recombinantly expressed biopolymers⁶⁴⁻⁶⁸. Indeed, many protein-based biomaterials, including silk^{65,69}, elastin^{67,70}, collagen^{71,72}, and resilin⁷³ have benefited from recombinant DNA technology. In addition to providing a path to increased structural and functional complexity of biomaterials, recombinant biopolymers are indispensable in structure-property relationships studies.

3.4.1 *Keratin SDS-PAGE and Western Blot*

In addition to K31 and K81, hair fibers contain different types of keratin proteins, including gamma-, alpha-, and beta-keratins⁴⁴. Beta-keratins provide protection to the hair fiber, gamma-keratins serve as a crosslinking agent and alpha-keratins function as the main structural component⁴⁴. As such, the desired component for fabrication of biomaterials is the alpha-keratins due to its important structural properties. However, through the extraction and purification process, it is often difficult to remove the other types of keratin proteins, as well as additional by-products, which results in a heterogeneous mixture following extraction and purification. On the other hand, recombinant protein are expressed and purified individually. The N-terminal histidine tag enables metal affinity purification allowing for efficient removal of all other proteins and by-products not containing the specific affinity tag. In **Figure 3. 1A** we first visually compare solutions of extracted and recombinant proteins. The purified recombinant protein solution is labeled “1” and the extracted protein solution is labeled “2”. The recombinant protein solution is clear while the

extracted solution, even after purification, appears brown. The observed color is from melanin not removed during purification, demonstrating the difficulty of removing compounds that may be tightly complexed to the larger keratin aggregates. In addition, SDS-PAGE analysis of the purified proteins further indicates the improved sample homogeneity of the recombinant keratins. In **Figure 3.1B**, lanes 1 and 2 represent affinity purified rhK31 (lane 1) and rhK81 (lane 2). A single protein band is present in each, showing that both recombinant proteins have been successfully purified with no observable by-products or unwanted contaminants. However, the extracted KTN sample in lane 3 has many protein components present, indicating either the difficulty in removing residual hair fiber components or protein degradation or both.

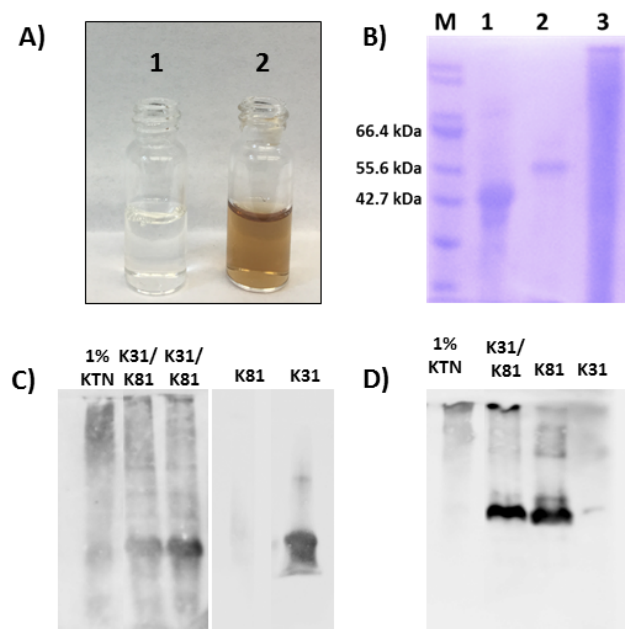


Figure 3.1. Comparison of purified recombinant and extracted keratins a) picture of purified recombinant (1) and extracted (2) solutions b) SDS-PAGE fractions: M-marker, 1-rhK31, 2-rhK81, 3-Extracted KTN c) Western blot with K31 antibody and d) Western blot with K81 antibody.

To verify the identity of the proteins observed in SDS-PAGE, we conducted a Western blot analysis, which confirmed that the predominant proteins in the recombinant materials preparations were K31 and K81 (**Figures 3.1C and 3.1D**, respectively), as expected. Interestingly, however, in the extracted sample, the stained bands correspond to higher molecular weights even under denaturing and reducing gel conditions. This suggests the existence of irreversible higher order oligomers in the extracted samples at the same solution conditions in which the recombinant sample is monomeric. The exception is the 1% KTN sample where a band corresponding to the molecular weight of monomeric K31 is observed (**Figure 1C**). Furthermore, not all bands present in SDS-PAGE of the KTN also appear in the Western blot, signifying the existence of additional proteins in the extracted sample. From the results obtained from SDS-PAGE and Western blot, it appears that recombinant protein production and purification methods provide starting materials of improved homogeneity over that of extracted keratins. However, when rhK31 and rhK81 are combined, bands corresponding to higher molecular weights than monomers appear in Western blots, analogous to extracted KTN sample. Thus, the recombinant heterodimer is capable of heteropolymerization and formation of higher order structures. To further investigate heteropolymerization of rhK31 and rhK81 we utilized SEC and DLS.

3.4.2 *SEC and DLS*

To prepare samples for SEC analysis, rhK31 and rhK81 were mixed in 8M urea buffer (Materials and Methods). KTN samples were resuspended in buffer of the same composition as the recombinant samples. SEC data obtained in buffer containing 8 M urea shows that both the extracted and recombinant keratin proteins contain structures that are larger than the K31/K81 heterodimer (**Figure 3.2**). Interestingly, the higher order oligomers are present in both samples even in the presence of a denaturant (urea) and reducing agent (DTT). It is important to note that

all samples are passed through a 0.22 μm filter before SEC analysis. Therefore, all structures larger than the filter cut-off will be excluded from this method of analysis.

While five peaks are observed in the recombinant sample chromatogram, the extracted heteropolymer chromatogram contains two broader peaks shifted toward shorter elution times (**Figure 3.2**). The estimated oligomeric states for each peak (labeled by the red numbers in the **Figure 3.2**) are shown in **Table 3.1**.

Table 3.1. Estimated oligomeric states from SEC analysis.

Peak #	rhK31/K81	KTN
1	Octamer	N/A*
2	Tetramer	Dimer
3	Dimer	----
4	Monomer	----

* Peak elutes in the void volume fraction.

Interestingly, higher molecular weight peaks 1, 2, and 3 in the recombinant sample overlap with peaks 1 and 3 in the extracted sample suggesting that the K31/K81 octamer, tetramer, and dimer are present in both the extracted and recombinant samples. Peak 1 in the extracted sample, not observed in the recombinant proteins sample, elutes at the time corresponding to the column void volume. Thus, sample components too large to be retained on the column are already present in the extracted sample. At the same time, there is no protein eluting at retention times corresponding to K31 and K81 monomers in the extracted sample. From the SEC analysis we conclude that in the recombinant sample under denaturing conditions the major fraction of the solution is monomeric rhK31 and rhK81 in equilibrium with higher order oligomers. On the contrary, the major fraction of the KTN solution corresponds to oligomers larger than octamers

and the smallest observable component is a dimer. Dimer observation in the KTN sample is consistent with the formation of the obligate keratin dimer in nature, however, it is interesting that this dimer is resistant to reducing and denaturing conditions.

The presence of larger heteropolymers in the extracted KTN sample, as observed in the SEC, SDS-PAGE, and Western blot analyses, are consistent with the extraction procedure that relies on breaking down preformed, durable keratin-based structures. In order to efficiently extract the desired keratin biopolymers, the extensive network of intermolecular disulfide bonds must be reduced. Thus, the size of sample components acquired from extraction is dependent on the efficiency with which this network is disrupted, and the resulting higher order structures persist due to covalent interactions that are not affected by the solution conditions. Conversely, recombinant protein production facilitates assembly from each individual component. To further probe the solution behavior of the recombinant and extracted keratins, we used DLS to monitor changes in oligomerization equilibrium as the concentration of denaturant in the sample was decreased.

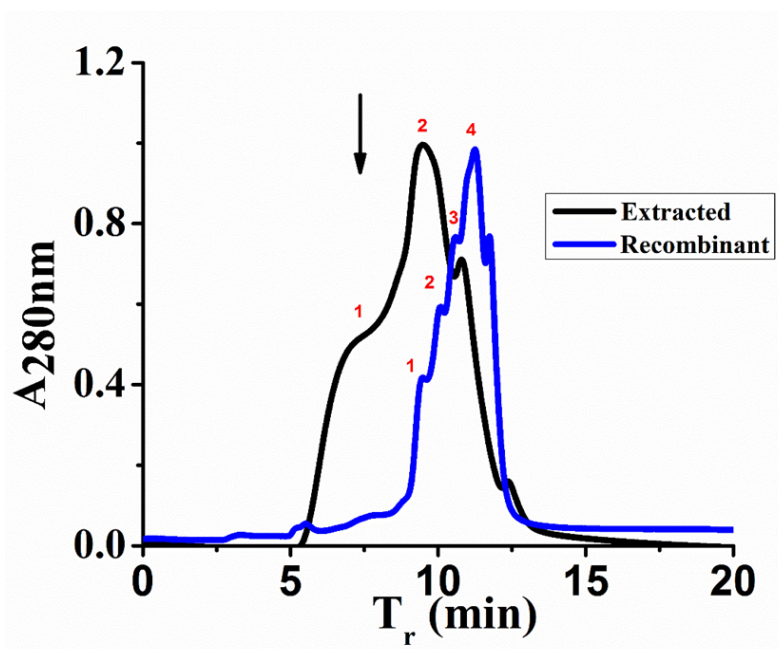


Figure 3.2. Chromatogram of recombinant (blue) and extracted (black) keratin in 8 M urea obtained from SEC. Red numbers correspond to peak labels listed in table 1.

We performed DLS on aliquots of samples obtained during each dialysis step. As the sample is dialyzed, the concentration of urea in the buffer is reduced in a step-wise manner in order to allow the proteins to return to their native state, and in the case of keratin proteins, to allow for self-assembly to occur. Thus, as the urea concentration decreases we expect the oligomerization equilibrium to shift towards higher order oligomers and finally fibers. However, all samples are filtered prior to analysis using a 0.22 μm filter. Consequently, any sample components larger than 0.22 μm will not be observed, similar to the SEC. **Figure 3.3** shows recombinant (**Figure 3.3A**) and extracted (**Figure 3.3B**) heteropolymer samples at 8 M (blue), 4 M (red), and 0 M (black) urea concentrations. Consistent with SEC data, nanostructures present in the KTN sample are larger than in the recombinant sample at the same solution conditions (**Table 3.2, Figure 3.3**).

An overlay of the volume percent of recombinant and extracted keratins in 0 M urea is shown in **Figure 3C**. The volume percent distribution provides the relative proportion of the different sample components. The populations detected in the DLS at 0 M urea corresponds to the keratin that has not been incorporated into IF after all denaturant has been removed from the system. The major scattering species in the recombinant keratin sample has an 8 nm hydrodynamic radius, consistent with K31 and/or K81 monomers⁷⁴. The extracted keratin sample is mostly composed of 50 nm oligomers. This is consistent with measurements obtained at each urea concentration, as well as the SEC and Western blot analysis, and further indicates that upon extraction the starting material is not completely reduced to individual proteins.

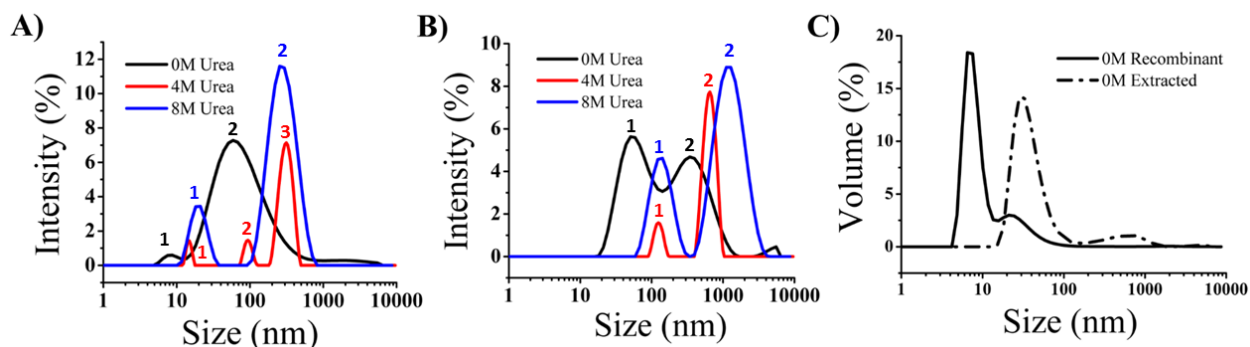


Figure 3.3. DLS from a) recombinant keratin urea series b) extracted keratin urea series and c) recombinant (solid line) and extracted (dotted line) keratin samples in 0 M urea.

Table 3.2. Hydrodynamic radius of species present in solution at decreasing urea concentrations.

Urea (M)	Peak #	rhK31/K81 (nm)	KTN (nm)
8	1	18	120
8	2	225	1100
4	1	13	110
4	2	120	900
4	3	460	----
0	1	8	50
0	2	60	295

3.4.3 TEM

One of the essential features of keratin protein materials is their intrinsic capacity for self-assembly. Retaining this important biological feature provides the ability for generation of materials such as films⁴⁰, hydrogels³⁸, and sponges⁴⁵. Self-assembly of keratin IFs is a well-studied process^{28,75}. During IF assembly a dimer composed of one type I (acidic) and one type II (basic) keratin is formed. Following dimer formation, tetramers form through antiparallel alignment of two heterodimers to create a staggered conformation. Subsequent parallel head to tail stacking of tetramers results in protofilaments, which further assemble to form 10 nm diameter IFs^{28,76}.

In order for recombinant keratin proteins to be viable for use as biomaterials, they too must possess the ability to self-assemble into fibers after expression and purification. Results from solution characterization point to the formation of higher order structures in both the recombinant and extracted samples.

Extracted and recombinant keratins were prepared using the dialysis protocol described in Materials and Methods. Samples, in buffer without urea and with a mild reducing agent, 5 mM DTT, were prepared for TEM analysis at a concentration of 5 mg/mL. **Figures 3.4A and 3.4B** are representative TEM images of rhK31/K81 nanostructures. The recombinant proteins appear to self-assemble into standard 10 nm diameter keratin IFs, and further form large bundles through additional IF interactions. These structures are several microns long and average 150 nm wide. **Figures 3.4C and 3.4D** are representative TEM images of the extracted keratin nanostructures. At a 5 mg/mL concentration, the extracted materials readily formed films on the TEM grid (Figure S2). These films appeared featureless and individual fibers or fiber bundles were not observed. Therefore, the extracted samples were diluted to 0.5 mg/mL. This sample concentration resulted in fibers observable by TEM, but the overall number of fibers, in comparison to the recombinant

sample was low. Moreover, these fibers do not have the typical IF morphology. The width of fibers was estimated to be between 70 and 100 nm, with lengths of a few microns (**Figure 3.4C and 3.4D**). However, similar to the recombinant sample, some bundling of fibers is apparent (**Figure 3.4C**).

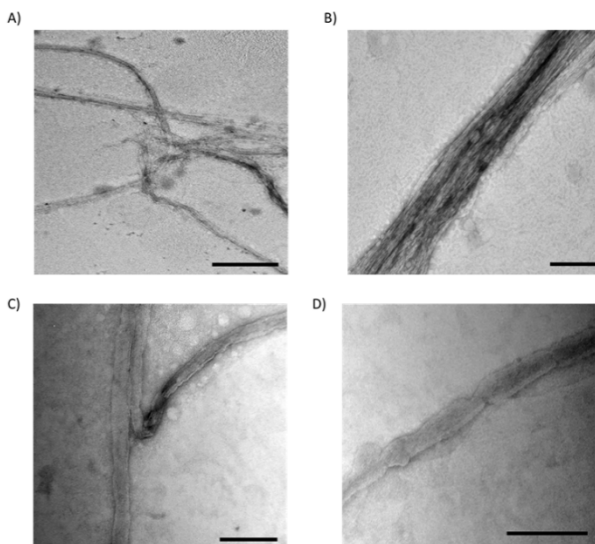


Figure 3.4. TEM images of recombinant (a-b) and extracted (c-d) keratin proteins. Scale bars are (a) 500 nm and (b-d) 300 nm. All images are stained with 2% uranyl acetate.

3.4.4 ToF SIMS

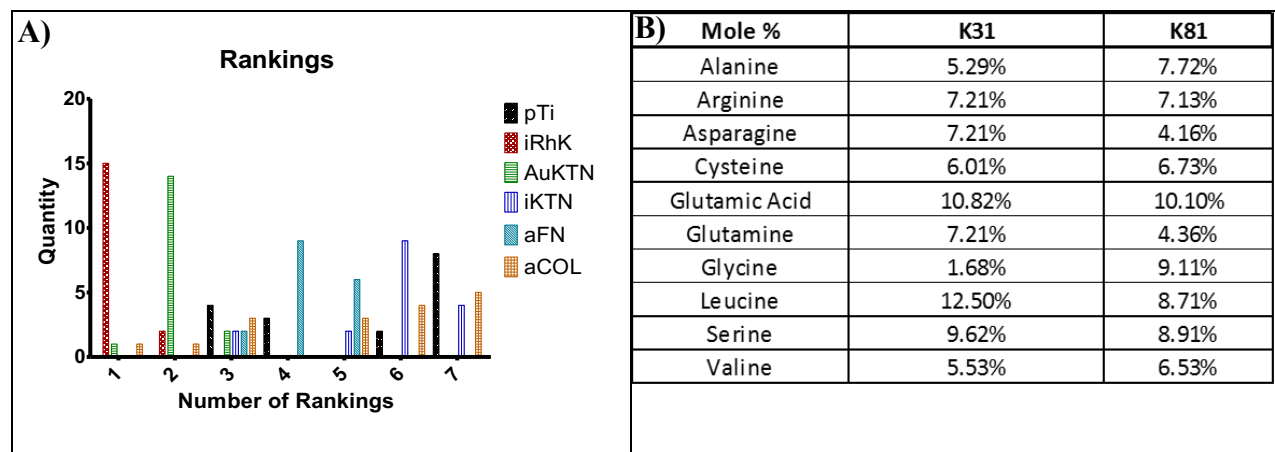


Figure 3.5. A) Keratin substrates were independently ranked from highest intensity ‘1’ to lowest intensity ‘7’ for each amino acid listed in 3.5B. Rankings for each substrate were then accumulated. If a substrate has 15 amino acids with the rank ‘1’ the quantity will be 15. Some amino acids in

the ToF-SIMS have multiple positive fragments, each fragments was used. A large '1' quantity signifies the highest intensity for relevant amino acids. B) Amino acids chosen to be analyzed are represented in this table, to be considered the amino acid mole percent for either K31 or K81 must exceed 6%.

Our KN coating thickness is postulated to be 2 nm or less⁷⁷, ToF-SIMS was chosen for elemental analysis because of its low detection resolution of one to two monolayers in comparison to other common techniques such as X-ray Photoelectron Spectroscopy^{78,79}. ToF SIMS produces mass spectra from the outermost layers (10-20 Å) of the surface material, we used the intensity level from the mass spectra for our further analysis. Characterization of keratin coatings, attached to titanium substrates via silane coupling chemistry, was challenging, owing to the extremely thin nature of the keratin layer. Cysteine is a defining element for keratins as it comprises approximately 6% of K31 and K81, so amino acids obtaining at least 6% for either K31 or K81 were used as a basis for positive keratin identification in ToF SIMS to preserve consistency as seen in **Figure 3.5B**. Relative intensities of the amino acids associated with these peptides were measured for each sample surface and ranked, 1 to 7, with 1 being the most abundant. **Figure 3.5** shows the number of peptides at each ranking for each test substrate. Although overall signal is low due to the thinness of the coatings, these data suggest that the recombinant keratin produces the most abundant coating. The method is by no means optimal, as suggested by the results from a plain titanium surface. Extracted keratin on gold provides an important control, and **Figure 3.5** shows a large number of peptides with a ranking of 2. The coating made using extracted keratins shows a relatively large number of peptides, but they are ranked no higher than 3, indicating that the thickness or continuity of this coating may not be as high as that for the recombinant proteins, or the extracted proteins deposited onto a gold surface. As expected, fibronectin and collagen gave

relatively fewer hits with high rankings. More insight into the ToF SIMS data can be garnered from assessment of the AFM data.

3.4.5 *AFM*

AFM is a commonly used technique with high resolution of approximately 1 Å to characterize topography only limited by thermal and electrical noise⁸⁰. This resolution allows for visualization of molecular structures. AFM confirms that recombinant keratins are able to create a uniform coating, although the roughness is not significantly different than pTi. When observing the topography visually, KTN on gold and recombinant keratins display similarly homogenous surfaces with limited appearance of aggregated features (**Figure 3.6A**). Here, KTN on gold is used as a positive control as it has been previously shown that cysteine readily bonds to gold surfaces, a phenomenon that has been used for the formation of self-assembled monolayers or SAMs⁷⁷. KTN attached through a silane coupling layer appears more irregular, suggesting that protein aggregates are present, which is also suggested by the SDS-PAGE, SEC and DLS data. The images are confirmed by roughness measurements that show the KTN on silane is significantly rougher than any of the other test substrates (**Figure 3.5B**). Taken together with the ToF SIMS data, it appears that KTN on silane is a less uniform coating, perhaps with a composition dominated by protein aggregates and/or uncoated areas, compared to the recombinant keratin on silane or KTN on gold.

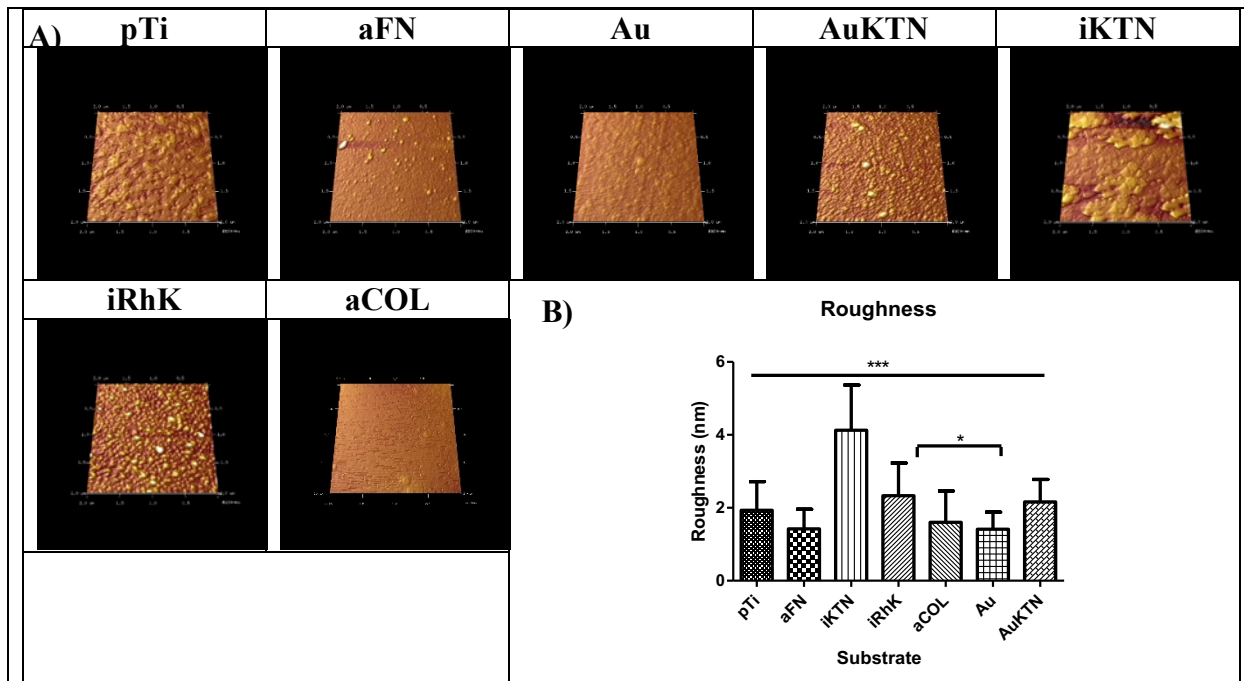


Figure 3.6. A) Rendered images of substrates examined by AFM. B) RMS roughness values of substrates. Significance shown is iKTN against all remaining experimental groups, there is additional significance between iRhK and Au. Significance is identified by * for $p \leq 0.05$, ** for $p \leq 0.01$, and *** for $p \leq 0.001$. $*** \leq 0.001$.

3.4.6 Cellular Motif Identification

Regardless of the extraction or fabrication method, retention of biological function is vital to many biomaterial coating applications. Protein attachment to silanes can elicit conformational changes that can decrease cell adhesion^{81,82}, as shown in several studies. Identification of cellular motifs indicates the coating's capability to possess biological function (i.e. cell adhesion through specific receptors). Hair keratins contain the leucine-aspartic acid-valine (LDV) motif, whereas wool keratin and fibronectin possess both the LDV and arginine-glycine-aspartic acid (RGD) motif^{30,83}. As shown in **Table 4** and **Figure 3.7A**, the recombinant keratin coating has larger affinity for $\alpha 2\beta 3$ compared to $\alpha 4\beta 1$, and is significant compared to both plain Ti and KTN. Although the primary motif in hair keratin is the LDV, various cell types have been shown to

adhere to extracted hair keratin⁴⁰. For the $\alpha4\beta1$ integrin, both KTN and KTN on gold shown a greater affinity than the recombinant keratin, which is unexpected due to the composition uniformity suggested by the ToF SIMS and AFM data, but specific conformation of the molecules on the surface and steric availability of the binding motifs would certainly play a role.

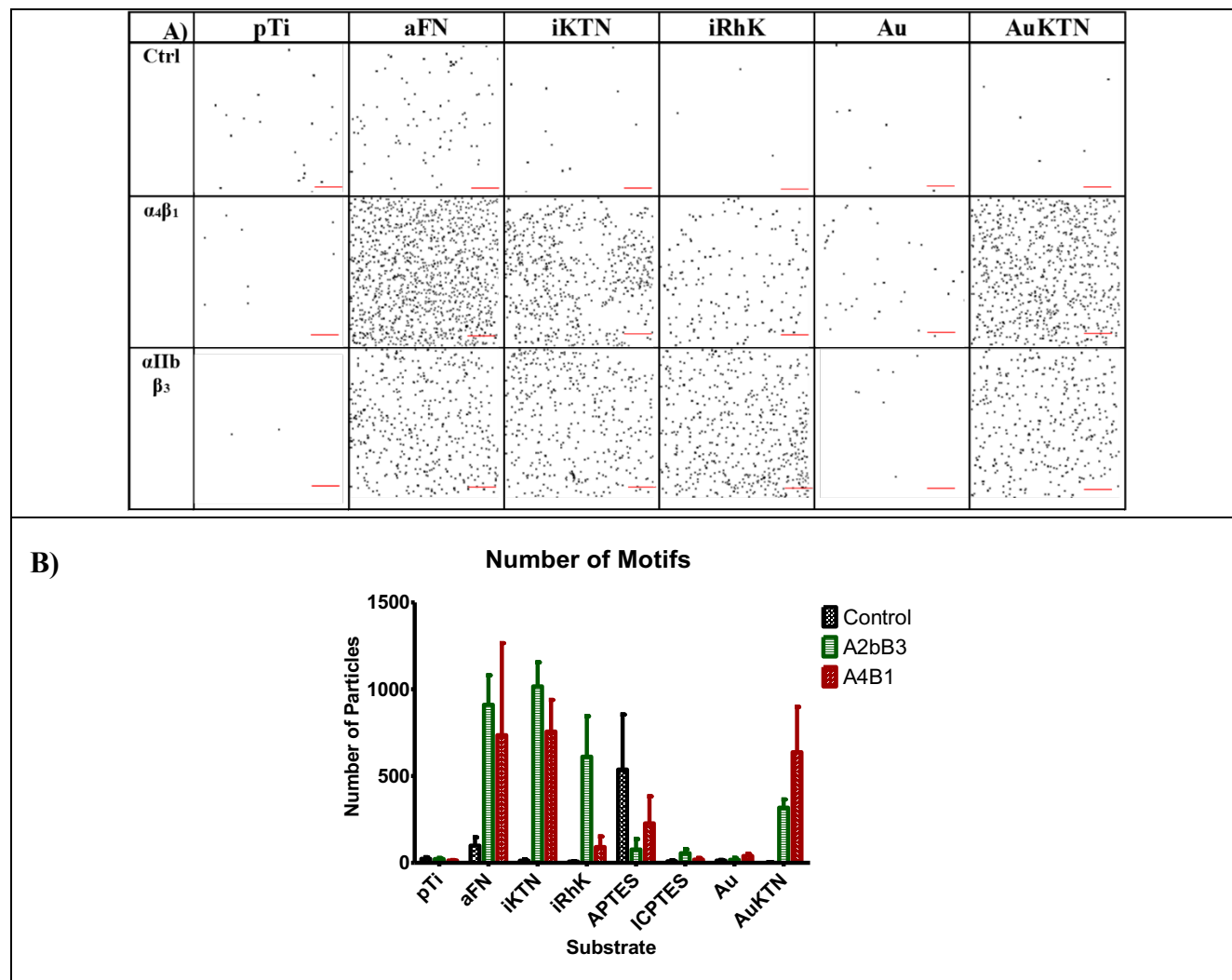


Figure 3.7. A) Cellular motifs identified using fluorescent spheres, binary images were created in Image J for better visualization and the scale bar represents 50 μ m. B) Number of cellular motifs on substrates.

3.4.7 Cellular Adhesion Immunochemistry

A cells' biological interactions with coatings can be partially characterized by the growth, maturation, and mechanism of attachment. An epithelial cell line, HaCaT, and connective tissue cell, fibroblasts, were used in this study to observe cell attachment. HaCaT cells are immortalized keratinocytes, with their primary *in vivo* cell attachment mediated to the basement membrane⁸⁴. Whereas, fibroblasts serve as a connective tissue cell model and attach to the extracellular matrix (ECM), a non-cellular structure that contains fibrous proteins, *in vivo*⁸⁵. Focal adhesions create transmembrane communication channels that can activate cell proliferation^{86,87}, phenotypic changes^{88,89}, and cell signaling cascades⁹⁰. Actin fibers are an indication of focal adhesion formation⁸⁷. **Figures 3.8 and 3.9** show the areas of positive actin staining for HaCaT and fibroblast cells, respectively. Although significant differences are not present between the various substrates, the morphologies described through circularity measures exhibit significant changes. In both HaCaT and fibroblast cells, plain Ti, fibronectin, and recombinant keratins allow for the cells to adopt a spread morphology. Cell spreading can indicate that cells perceive the underlying substrate through trans-membrane receptors, even though they may have similar actin protein areas upon staining.

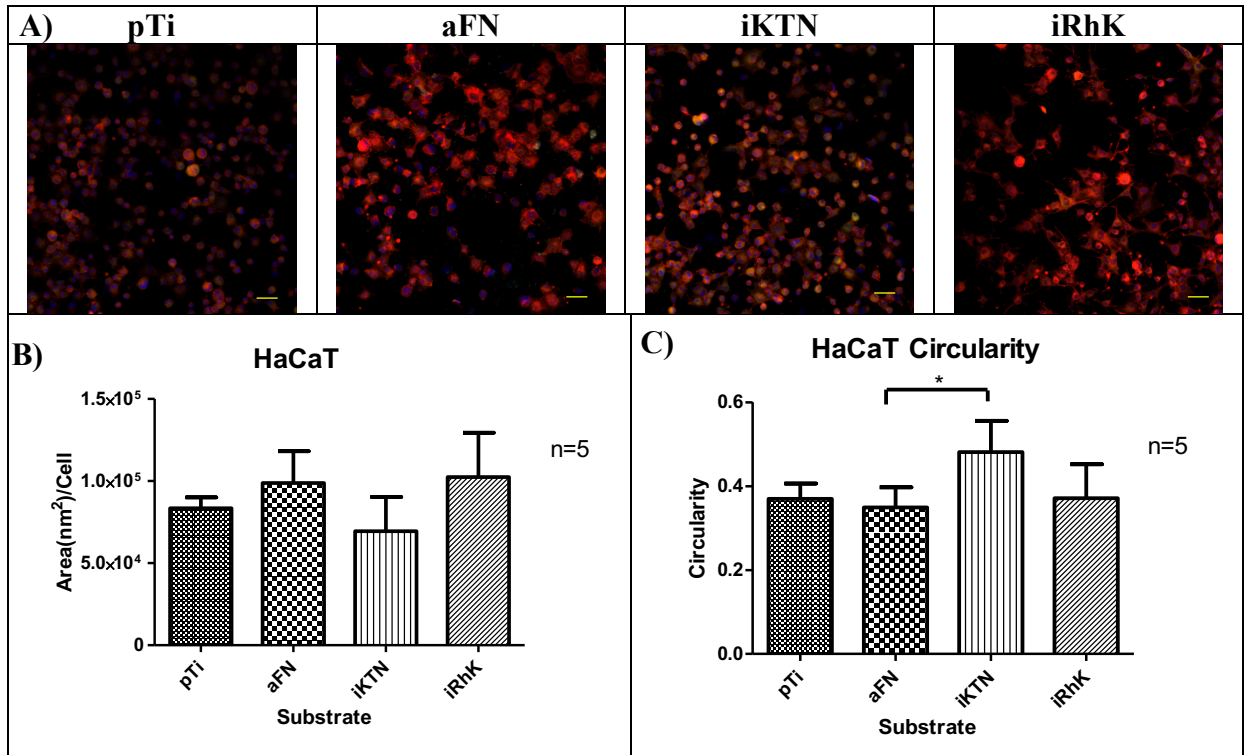


Figure 3.8. A) HaCaT cells focal adhesions represented by red (Actin), green (vinculin), blue (nucleus). B) Area of Actin staining quantified by ImageJ (n=5). C) Circularity observed by Image J is graphical represented (n=5). Significance is identified by * for $p \leq 0.05$, ** for $p \leq 0.01$, and *** for $p \leq 0.001$. *** ≤ 0.001 . Scale bars represent 50 μm .

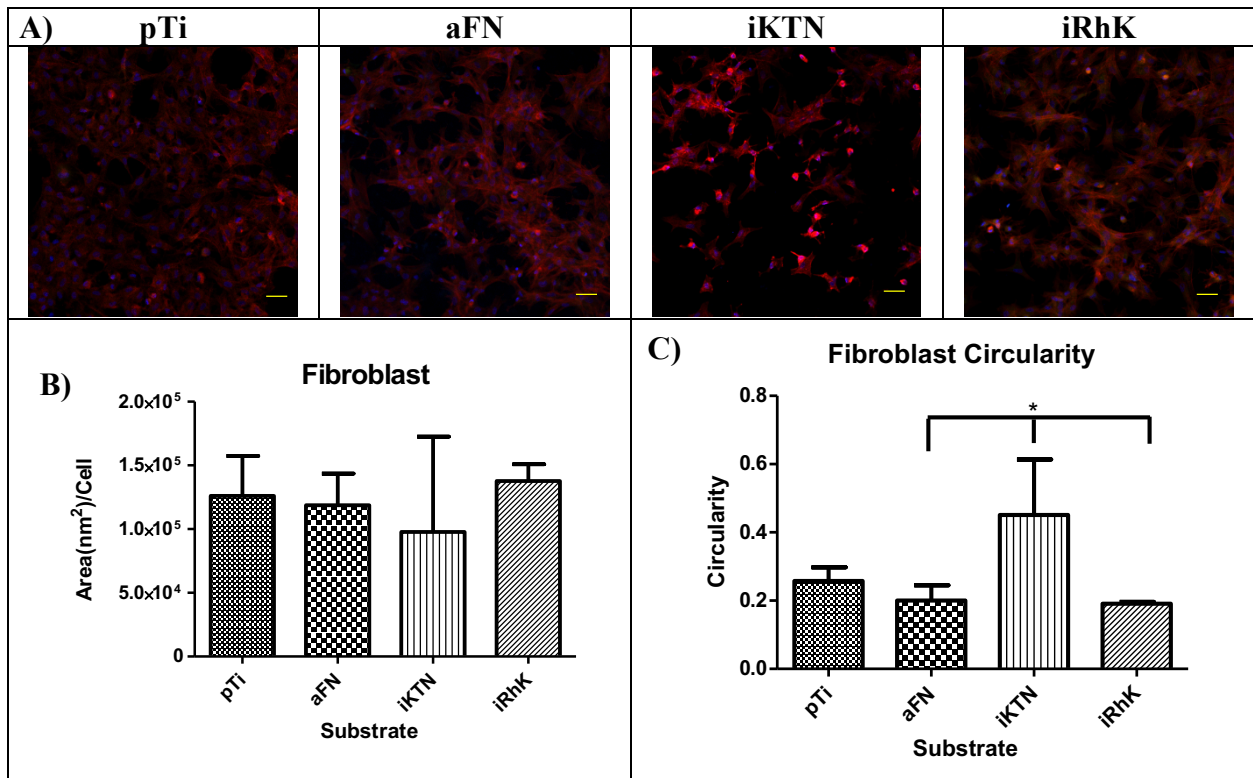


Figure 3.9. A) Fibroblasts focal adhesions represented by red (Actin), green (vinculin), blue (nucleus). B) Area of Actin staining quantified by ImageJ. C) Circularity observed by Image J is graphical represented. Circularity ranges from zero to one, where one indicates a perfect circle. Significance is identified by * for $p \leq 0.05$, ** for $p \leq 0.01$, and *** for $p \leq 0.001$. *** ≤ 0.001 . Scale bars represent 50 μm .

3.4.8 *Involucrin and Smooth Muscle Actin Detection*

Upregulation of involucrin is an early marker of terminal differentiation for keratinocytes⁹¹, which describes the progression of keratinocytes towards a stratified epidermis structure. HaCaT cells exposed to the recombinant keratin coating expressed a higher concentration of the involucrin protein in comparison to other experimental groups (**Figure 3.10A**). During this relatively short-term culture period, the recombinant keratin provokes a response in the HaCaT cells indicating the cells are beginning terminal differentiation. When these cells are transforming from spinal cells to granular cells, an upregulation of involucrin occurs, denoting the beginning of keratinization. Other studies have examined involucrin upregulation as

a defining test for artificial skin equivalents^{92,93}. These data suggest that the recombinant keratin has a higher propensity for inducing involucrin and hence, maturation in terms of potential skin cell differentiation.

Smooth muscle actin is a definitive characteristic of myofibroblast, which can be induced through mechanotransduction and biochemical cues. Fibroblasts are observed to express SMA on all substrates. Although SMA is a marker for myofibroblasts present in granulation tissue during wound healing⁹⁴, substrate stiffness can induce the smooth muscle actin phenotype and cell contractility⁹⁵⁻⁹⁷. HeLa cells served as the positive control but were seeded on at tissue culture plate, which does not have an equal stiffness to titanium, this could provide an explanation to why band area and intensity for SMA in HeLa cells is less than all other substrates.

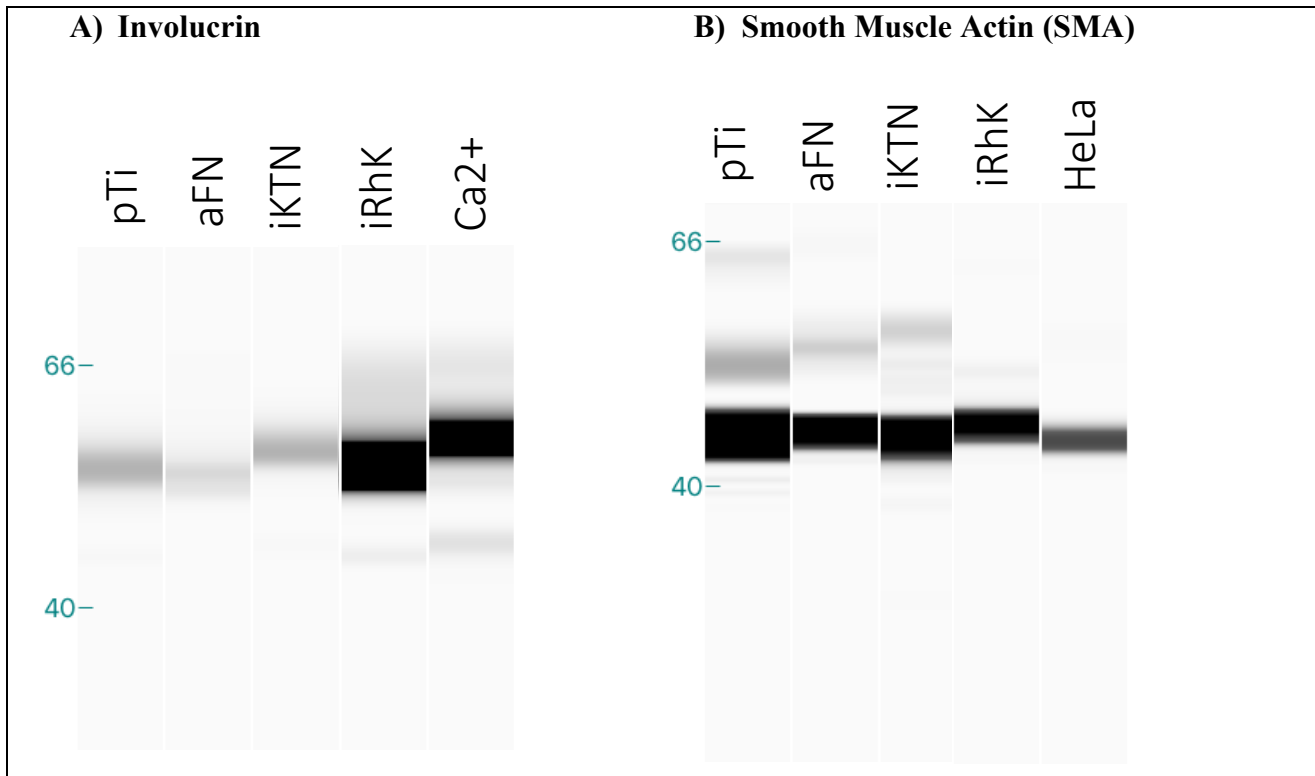


Figure 3.10. A) **Involucrin.** A digitized Western blot lane view from the ProteinSimple Wes instrument for involucrin including Ca²⁺ induced HaCaT cells, which represent the positive control. B) **Smooth Muscle Actin.** Digitized Western blot for smooth muscle actin in fibroblasts.

3.5 Conclusions

Keratin-based biomaterials have been successfully used as scaffolds in regenerative medicine and tissue engineering^{41,53,98,99}. However, structure-property studies were impeded by the lack of homogeneity and consistent samples. We have shown here that trichocytic keratins K31 and K81 can be produced recombinantly, resulting in samples of increased homogeneity. Not surprisingly, the composition of extracted versus recombinant materials is shifted towards higher molecular weight oligomers. The distribution of oligomers and their sizes are dependent on the efficiency with which the extensive network of intermolecular disulfide bonds is disrupted in hair fibers, further contributing to the sample heterogeneity.

The recombinant heteropolymer forms standard IF that further associate to create large bundled structures, while extracted keratins fiber did not appear to have the typical IF morphology. Nonetheless, extracted keratins have a remarkable propensity for self-assembly in films that was not observed for recombinant samples under the same conditions. Functional differences in recombinant and extracted keratin composition can also be observed in topography, motif identification, and cellular responses. This further reinforces the notion that recombinant and extracted samples have different compositions. It appears that recombinant keratins, probably due to their relatively higher level of homogeneity and lack of low molecular weight contaminants, form more uniform coatings, which in turn leads to increased biological activity when compared to KTN.

Design flexibility afforded by recombinant technology will result in multifunctional, dynamic keratin materials. Tailoring of the function, composition, and nanostructure can now be achieved at the amino acid sequence level. Both extracted and recombinant keratin biopolymers provide a promising tool for engineering novel biomaterials with controlled chemical and physical

properties, and future work on the fabrication and characterization of these materials will allow for new advances in regenerative medicine, medical device coatings, and tissue engineering.

3.6 Acknowledgements

The authors would like to thank Virginia Tech, the VT Chemistry Department, the Department of Biomedical Engineering and Mechanics, the Department of Defense Congressionally Directed Medical Research Programs (CDMRP; grant number W81XWH-15-1-0343), and Virginia Tech-Initiative for Maximizing Student Development (IMSD; grant number R25GM072767-10) for funding. We also thank Dr. Sujee Jeyapalina for the gift of the HaCaT cells and for helpful discussions regarding culture and assays for these cells. The authors are also thankful to the Grove and Van Dyke labs for discussions and careful reading of the draft manuscript.

3.7 References

1. Goldberg, M., Langer, R. & Jia, X. Nanostructured materials for applications in drug delivery and tissue engineering. *J. Biomater. Sci. Polym. Ed.* **18**, 241–268 (2007).
2. Kuratomi, Y. *et al.* Laminin γ 1 chain peptide, C-16 (KAFDITYVRLKF), promotes migration, MMP-9 secretion and pulmonary metastasis of B16–F10 mouse melanoma cells. *Br. J. Cancer* **86**, 1169–1173 (2002).
3. Nectow, A. R., Marra, K. G. & Kaplan, D. L. Biomaterials for the Development of Peripheral Nerve Guidance Conduits. *Tissue Eng. Part B Rev.* **18**, 40–50 (2012).
4. Pakulska, M. M., Ballios, B. G. & Shoichet, M. S. Injectable hydrogels for central nervous system therapy. *Biomed. Mater.* **7**, 24101 (2012).
5. Park, S.-H., Park, S. R., Chung, S. Il, Pai, K. S. & Min, B.-H. Tissue-engineered Cartilage Using Fibrin/Hyaluronan Composite Gel and Its In Vivo Implantation. *Artif. Organs* **29**, 838–845 (2005).
6. Rouse, J. G. & Van Dyke, M. E. A review of keratin-based biomaterials for biomedical applications. *Materials (Basel)*. **3**, 999–1014 (2010).
7. Schleicher, I. *et al.* Surface Modification by Complexes of Vitronectin and Growth Factors for Serum-Free Culture of Human Osteoblasts. *Tissue Eng.* **11**, 1688–1698 (2005).
8. Silva, S. S., Mano, J. F. & Reis, R. L. Potential applications of natural origin polymer-based systems in soft tissue regeneration. *Crit. Rev. Biotechnol.* **30**, 200–221 (2010).
9. Stoppel, W. L., Ghezzi, C. E., McNamara, S. L., III, L. D. B. & Kaplan, D. L. Clinical Applications of Naturally Derived Biopolymer-Based Scaffolds for Regenerative Medicine. *Ann. Biomed. Eng.* **43**, 657–680 (2014).
10. Vepari, C. & Kaplan, D. L. Silk as a biomaterial. *Prog. Polym. Sci.* **32**, 991–1007 (2007).
11. WITTMER, C., PHELPS, J., SALTZMAN, W. & VANTASSEL, P. Fibronectin terminated multilayer films: Protein adsorption and cell attachment studies. *Biomaterials* **28**, 851–860 (2007).
12. Brinckmann, J. Collagens at a Glance. *Topics in Current Chemistry* 1–6 (2005). doi:10.1007/b103817
13. McKeown-Longo, P. J. & Panetti, T. S. Structure and Function of Vitronectin. *Trends Glycosci. Glycotechnol.* **8**, 327–340 (1996).
14. Pankov, R. Fibronectin at a glance. *J. Cell Sci.* **115**, 3861–3863 (2002).
15. Parenteau-Bareil, R., Gauvin, R. & Berthod, F. Collagen-Based Biomaterials for Tissue Engineering Applications. *Materials (Basel)*. **3**, 1863–1887 (2010).
16. Vrhovski, B. & Weiss, A. S. Biochemistry of tropoelastin. *Eur. J. Biochem.* **258**, 1–18 (1998).
17. von der Mark, K., Park, J., Bauer, S. & Schmuki, P. Nanoscale engineering of biomimetic surfaces: cues from the extracellular matrix. *Cell Tissue Res.* **339**, 131–153 (2010).
18. Anderson, J. M., Rodriguez, A. & Chang, D. T. Foreign body reaction to biomaterials. *Semin. Immunol.* **20**, 86–100 (2008).
19. Smith Callahan, L. A. *et al.* Directed differentiation and neurite extension of mouse embryonic stem cell on aligned poly(lactide) nanofibers functionalized with YIGSR peptide. *Biomaterials* **34**, 9089–9095 (2013).

20. de Luca, A. C., Faroni, A., Downes, S. & Terenghi, G. Differentiated adipose-derived stem cells act synergistically with RGD-modified surfaces to improve neurite outgrowth in a co-culture model. *J. Tissue Eng. Regen. Med.* **10**, 647–655 (2013).
21. Lutolf, M. P. & Hubbell, J. A. Synthetic biomaterials as instructive extracellular microenvironments for morphogenesis in tissue engineering. *Nat. Biotechnol.* **23**, 47–55 (2005).
22. Stevens, M. M. & George, J. H. Exploring and Engineering the Cell Surface Interface. doi:10.1126/science.1106587
23. Williams, D. F. On the nature of biomaterials. *Biomaterials* **30**, 5897–5909 (2009).
24. Gomes, S., Leonor, I. B., Mano, J. F., Reis, R. L. & Kaplan, D. L. Natural and genetically engineered proteins for tissue engineering. *Prog. Polym. Sci.* **37**, 1–17 (2012).
25. Engler, A. J., Sen, S., Sweeney, H. L. & Discher, D. E. Matrix elasticity directs stem cell lineage specification. *Cell* **126**, 677–689 (2006).
26. Kohn, J., Welsh, W. J. & Knight, D. A new approach to the rationale discovery of polymeric biomaterials. *Biomaterials* **28**, 4171–4177 (2007).
27. Almine, J. F. *et al.* Elastin-based materials. *Chem. Soc. Rev.* **39**, 3371 (2010).
28. Coulombe, P. A. Elucidating the early stages of keratin filament assembly. *J. Cell Biol.* **111**, 153–169 (1990).
29. Altman, G. H. *et al.* Silk-based biomaterials. *Biomaterials* **24**, 401–416 (2003).
30. Tachibana, A., Furuta, Y., Takeshima, H., Tanabe, T. & Yamauchi, K. Fabrication of wool keratin sponge scaffolds for long-term cell cultivation. *J. Biotechnol.* **93**, 165–170 (2002).
31. Lu, Q. *et al.* Water-insoluble silk films with silk I structure. *Acta Biomater.* **6**, 1380–1387 (2010).
32. An, B., Lin, Y.-S. & Brodsky, B. Collagen interactions: Drug design and delivery. *Adv. Drug Deliv. Rev.* **97**, 69–84 (2016).
33. Fearing, B. & Dyke, M. Van. In vitro response of macrophage polarization to a keratin biomaterial. *Acta Biomater.* (2014). at <<http://www.sciencedirect.com/science/article/pii/S1742706114001603>>
34. Vasconcelos, A., Freddi, G. & Cavaco-Paulo, A. Biodegradable Materials Based on Silk Fibroin and Keratin. *Biomacromolecules* **9**, 1299–1305 (2008).
35. Belcarz, A. *et al.* Covalent coating of hydroxyapatite by keratin stabilizes gentamicin release. *J. Biomed. Mater. Res. Part B Appl. Biomater.* **89B**, 102–113 (2009).
36. Dias, M. B., Reyes-Gonzalez, L., Veloso, F. M. & Casman, E. A. Effects of the USA PATRIOT Act and the 2002 Bioterrorism Preparedness Act on select agent research in the United States. *Proc. Natl. Acad. Sci.* **107**, 9556–9561 (2010).
37. Dias, G. J., Peplow, P. V, McLaughlin, A., Teixeira, F. & Kelly, R. J. Biocompatibility and osseointegration of reconstituted keratin in an ovine model. *J. Biomed. Mater. Res. Part A* **9999A**, NA-NA (2009).
38. Hill, P. S. *et al.* Repair of Peripheral Nerve Defects in Rabbits Using Keratin Hydrogel Scaffolds. *Tissue Eng. Part A* **17**, 1499–1505 (2011).
39. Lee, K. Y., Kong, S. J., Park, W. H., Ha, W. S. & Kwon, I. C. Effect of surface properties on the antithrombogenicity of silk fibroin/S-carboxymethyl kerateine blend films. *J. Biomater. Sci. Polym. Ed.* **9**, 905–914 (1998).

40. Reichl, S. Films based on human hair keratin as substrates for cell culture and tissue engineering. *Biomaterials* **30**, 6854–6866 (2009).
41. Reichl, S., Borrelli, M. & Geerling, G. Keratin films for ocular surface reconstruction. *Biomaterials* **32**, 3375–3386 (2011).
42. Saul, J. M., Ellenburg, M. D., de Guzman, R. C. & Dyke, M. Van. Keratin hydrogels support the sustained release of bioactive ciprofloxacin. *J. Biomed. Mater. Res. Part A* **98A**, 544–553 (2011).
43. Shen, D. *et al.* The amelioration of cardiac dysfunction after myocardial infarction by the injection of keratin biomaterials derived from human hair. *Biomaterials* **32**, 9290–9299 (2011).
44. Sierpinski, P. *et al.* The use of keratin biomaterials derived from human hair for the promotion of rapid regeneration of peripheral nerves. *Biomaterials* **29**, 118–128 (2008).
45. Tachibana, A., Kaneko, S., Tanabe, T. & Yamauchi, K. Rapid fabrication of keratin–hydroxyapatite hybrid sponges toward osteoblast cultivation and differentiation. *Biomaterials* **26**, 297–302 (2005).
46. Thilagar, S., Jothi, N. A., Omar, A. R. S., Kamaruddin, M. Y. & Ganabadi, S. Effect of keratin-gelatin and bFGF-gelatin composite film as a sandwich layer for full-thickness skin mesh graft in experimental dogs. *J. Biomed. Mater. Res. Part B Appl. Biomater.* **88B**, 12–16 (2009).
47. Yamauchi, K., Maniwa, M. & Mori, T. Cultivation of fibroblast cells on keratin-coated substrata. *J. Biomater. Sci. Polym. Ed.* **9**, 259–270 (1998).
48. Richter, J. R., de Guzman, R. C. & Van Dyke, M. E. Mechanisms of hepatocyte attachment to keratin biomaterials. *Biomaterials* **32**, 7555–7561 (2011).
49. Kellner, J. C. & Coulombe, P. A. Keratins and protein synthesis: the plot thickens: Figure 1. *J. Cell Biol.* **187**, 157–159 (2009).
50. Kowalczewski, C. J. *et al.* Reduction of ectopic bone growth in critically-sized rat mandible defects by delivery of rhBMP-2 from keratine biomaterials. *Biomaterials* **35**, 3220–3228 (2014).
51. Burnett, L. R. *et al.* Novel keratin (KeraStat™) and polyurethane (Nanosan®-Sorb) biomaterials are hemostatic in a porcine lethal extremity hemorrhage model. *J. Biomater. Appl.* **28**, 869–879 (2013).
52. Apel, P. J. *et al.* Peripheral Nerve Regeneration Using a Keratin-Based Scaffold: Long-Term Functional and Histological Outcomes in a Mouse Model. *J. Hand Surg. Am.* **33**, 1541–1547 (2008).
53. Ham, T. R. *et al.* Tunable Keratin Hydrogels for Controlled Erosion and Growth Factor Delivery. *Biomacromolecules* **17**, 225–236 (2015).
54. Parker, R. N. *et al.* Homo- and heteropolymer self-assembly of recombinant trichocytic keratins. *Biopolymers* **107**, e23037 (2017).
55. de Guzman, R. C. *et al.* Mechanical and biological properties of keratose biomaterials. *Biomaterials* **32**, 8205–8217 (2011).
56. Yu, J., Yu, D., Checkla, D. M., Freedberg, I. M. & Bertolino, A. P. Human hair keratins. *J. Invest. Dermatol.* **101**, S56–S59 (1993).
57. Strnad, P., Usachov, V., Debes, C., Gräter, F. & Parry, D. Unique amino acid signatures that are evolutionarily conserved distinguish simple-type, epidermal and hair keratins. *J Cell Sci* (2011). at <<http://jcs.biologists.org/content/124/24/4221.short>>

58. Honda, Y. *et al.* *In vitro* Assembly Properties of Human Type I and II Hair Keratins. *Cell Struct. Funct.* **39**, 31–43 (2014).
59. Van Dyke, M. & Rahmany, M. Keratin Nanomaterials and Methods of Production. (2015). at <<https://www.google.com/patents/US20170051027>>
60. Trent, A. & Van Dyke, M. E. Development and characterization of a biomimetic coating for percutaneous devices. *Mater. Sci. Eng. C*
61. Middleton, C. A., Pendegrass, C. J., Gordon, D., Jacob, J. & Blunn, G. W. Fibronectin silanized titanium alloy: a bioinductive and durable coating to enhance fibroblast attachment in vitro. *J. Biomed. Mater. Res. Part A* **83**, 1032–1038 (2007).
62. Chimutengwende-Gordon, M., Pendegrass, C. & Blunn, G. Enhancing the soft tissue seal around intraosseous transcutaneous amputation prostheses using silanized fibronectin titanium alloy. *Biomed. Mater.* **6**, 25008 (2011).
63. Vanderleyden, E., Van Hoorebeke, L., Schacht, E. & Dubruel, P. Comparative Study of Collagen and Gelatin Coatings on Titanium Surfaces. *Macromol. Symp.* **309–310**, 190–198 (2011).
64. Dinjaski, N. & Kaplan, D. L. Recombinant protein blends: silk beyond natural design. *Curr. Opin. Biotechnol.* **39**, 1–7 (2016).
65. Harris, T. I. *et al.* Sticky Situation: An Investigation of Robust Aqueous-Based Recombinant Spider Silk Protein Coatings and Adhesives. *Biomacromolecules* **17**, 3761–3772 (2016).
66. Jang, Y. & Champion, J. A. Self-Assembled Materials Made from Functional Recombinant Proteins. *Acc. Chem. Res.* **49**, 2188–2198 (2016).
67. Rodríguez-Cabello, J. C., Arias, F. J., Rodrigo, M. A. & Girotti, A. Elastin-like polypeptides in drug delivery. *Adv. Drug Deliv. Rev.* **97**, 85–100 (2016).
68. Zhou, M.-L., Qian, Z.-G., Chen, L., Kaplan, D. L. & Xia, X.-X. Rationally Designed Redox-Sensitive Protein Hydrogels with Tunable Mechanical Properties. *Biomacromolecules* **17**, 3508–3515 (2016).
69. Spiess, K., Lammel, A. & Scheibel, T. Recombinant Spider Silk Proteins for Applications in Biomaterials. *Macromol. Biosci.* **10**, 998–1007 (2010).
70. Teng, W., Cappello, J. & Wu, X. Recombinant Silk-Elastinlike Protein Polymer Displays Elasticity Comparable to Elastin. *Biomacromolecules* **10**, 3028–3036 (2009).
71. An, B., Kaplan, D. L. & Brodsky, B. Engineered recombinant bacterial collagen as an alternative collagen-based biomaterial for tissue engineering. *Front. Chem.* **2**, (2014).
72. An, B. *et al.* Recombinant Collagen Engineered to Bind to Discoidin Domain Receptor Functions as a Receptor Inhibitor. *J. Biol. Chem.* **291**, 4343–4355 (2015).
73. Elvin, C. M. *et al.* Synthesis and properties of crosslinked recombinant pro-resilin. *Nature* **437**, 999–1002 (2005).
74. Steinert, P. M., Marekov, L. N., Fraser, R. D. B. & Parry, D. A. D. Keratin Intermediate Filament Structure. *J. Mol. Biol.* **230**, 436–452 (1993).
75. Steinert, P. M., Steven, A. C. & Roop, D. R. Structural Features of Epidermal Keratin Filaments Reassembled in Vitro. *J. Invest. Dermatol.* **81**, S86–S90 (1983).
76. Hatzfeld, M. The coiled coil of in vitro assembled keratin filaments is a heterodimer of type I and II keratins: use of site-specific mutagenesis and recombinant protein expression. *J. Cell Biol.* **110**, 1199–1210 (1990).

77. de Guzman, R. C. *et al.* Binding Interactions of Keratin-Based Hair Fiber Extract to Gold, Keratin, and BMP-2. *PLoS One* **10**, e0137233 (2015).
78. Lhoest, J.-B., Detrait, E., van den Bosch de Aguilar, P. & Bertrand, P. Fibronectin adsorption, conformation, and orientation on polystyrene substrates studied by radiolabeling, XPS, and ToF SIMS. *J. Biomed. Mater. Res.* **41**, 95–103 (1998).
79. Belu, A. M., Graham, D. J. & Castner, D. G. Time-of-flight secondary ion mass spectrometry: techniques and applications for the characterization of biomaterial surfaces. *Biomaterials* **24**, 3635–3653 (2003).
80. Last, J. A., Russell, P., Nealey, P. F. & Murphy, C. J. The applications of atomic force microscopy to vision science. *Invest. Ophthalmol. Vis. Sci.* **51**, 6083–94 (2010).
81. Webb, K., Hlady, V. & Tresco, P. A. Relationships among cell attachment, spreading, cytoskeletal organization, and migration rate for anchorage-dependent cells on model surfaces. *J. Biomed. Mater. Res.* **49**, 362–8 (2000).
82. Keselowsky, B. & Collard, D. Surface chemistry modulates fibronectin conformation and directs integrin binding and specificity to control cell adhesion. *J. Biomed.* (2003). at <<http://onlinelibrary.wiley.com/doi/10.1002/jbm.a.10537/full>>
83. Verma, V., Verma, P., Ray, P. & Ray, A. R. Preparation of scaffolds from human hair proteins for tissue-engineering applications. *Biomed. Mater.* **3**, 25007 (2008).
84. Breitzkreutz, D. *et al.* Epidermal differentiation and basement membrane formation by HaCaT cells in surface transplants. *Eur. J. Cell Biol.* **75**, 273–286 (1998).
85. Rhee, S. & Grinnell, F. Fibroblast mechanics in 3D collagen matrices. *Adv. Drug Deliv. Rev.* **59**, 1299–1305 (2007).
86. Petrie, T. A. *et al.* The effect of integrin-specific bioactive coatings on tissue healing and implant osseointegration. *Biomaterials* **29**, 2849–2857 (2008).
87. Yoshigi, M., Hoffman, L. M., Jensen, C. C., Yost, H. J. & Beckerle, M. C. Mechanical force mobilizes zyxin from focal adhesions to actin filaments and regulates cytoskeletal reinforcement. *J. Cell Biol.* **171**, 209–215 (2005).
88. Fearing, B. V & Dyke, M. E. Van. Activation of Astrocytes in Vitro by Macrophages Polarized with Keratin Biomaterial Treatment. *Open J. Regen. Med.* **5**, 1–13 (2016).
89. Owan, I. *et al.* Mechanotransduction in bone: osteoblasts are more responsive to fluid forces than mechanical strain. *Am. J. Physiol. Physiol.* **273**, C810–C815 (1997).
90. Maqueda, A. *et al.* Activation pathways of $\alpha 4\beta 1$ integrin leading to distinct T-cell cytoskeleton reorganization, Rac1 regulation and Pyk2 phosphorylation. *J. Cell. Physiol.* **207**, 746–756 (2006).
91. Fiona, M. & Watt, D. Involucrin and other markers of keratinocyte terminal differentiation. *J Invest Dermatol* (1983). at <https://www.researchgate.net/profile/Fiona_Watt/publication/16849977_Involucrin_and_other_markers_of_keratinocyte_terminal_differentiation/links/549d8a830cf2fedbc31195b7.pdf>
92. Yang, E. K. *et al.* Tissue Engineered Artificial Skin Composed of Dermis and Epidermis. *Artif. Organs* **24**, 7–17 (2000).
93. Jung, M. H., Jung, S.-M. & Shin, H. S. Co-stimulation of HaCaT keratinization with mechanical stress and air-exposure using a novel 3D culture device. *Sci. Rep.* **6**, 33889 (2016).

94. Gabbiani, G. The myofibroblast in wound healing and fibrocontractive diseases. *J. Pathol.* **200**, 500–503 (2003).
95. Solon, J., Levental, I., Sengupta, K., Georges, P. C. & Janmey, P. A. Fibroblast adaptation and stiffness matching to soft elastic substrates. *Biophys. J.* **93**, 4453–61 (2007).
96. Hinz, B., Celetta, G., Tomasek, J. J., Gabbiani, G. & Chaponnier, C. Alpha-smooth muscle actin expression upregulates fibroblast contractile activity. *Mol. Biol. Cell* **12**, 2730–41 (2001).
97. Jones, C. & Ehrlich, H. P. Fibroblast expression of α -smooth muscle actin, $\alpha 2\beta 1$ integrin and $\alpha v\beta 3$ integrin: influence of surface rigidity. *Exp. Mol. Pathol.* **91**, 394–9 (2011).
98. Tomblyn, S. *et al.* Keratin hydrogel carrier system for simultaneous delivery of exogenous growth factors and muscle progenitor cells. *J. Biomed. Mater. Res. Part B Appl. Biomater.* **104**, 864–879 (2015).
99. Pace, L. A. *et al.* A Human Hair Keratin Hydrogel Scaffold Enhances Median Nerve Regeneration in Nonhuman Primates: An Electrophysiological and Histological Study. *Tissue Eng. Part A* 131115063659000 (2013). doi:10.1089/ten.tea.2013.0084

3.8 Supplementary Figures

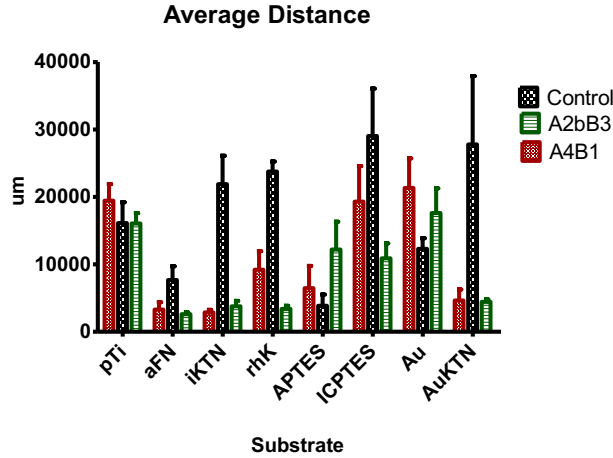


Figure 3.11 Average distance between cellular motifs.

Table S3.3. Significance for the averages of motif distance. The * signifies $p \leq 0.05$, ** signifies $p \leq 0.01$, *** signifies $p \leq 0.001$, and ns signifies $p \geq 0.05$.

Average Distance		pTi	aFN	iKTN	iRhK	Au	AuKTN
pTi	Control		ns	ns	ns	ns	**
	alpha4 Beta1		***	***	*	ns	***
	alpha2b Beta3		**	**	**	ns	ns
aFN	Control			**	***	**	***
	alpha4 Beta1			ns	ns	ns	ns
	alpha2b Beta3			ns	ns	***	***
iKTN	Control				ns	ns	ns
	alpha4 Beta1				ns	*	ns
	alpha2b Beta3				ns	**	**
iRhK	Control					ns	ns
	alpha4 Beta1					ns	ns
	alpha2b Beta3					ns	ns
Au	Control						ns
	alpha4 Beta1						ns
	alpha2b Beta3						ns

Table S3.4. Significance for the averages of motif sites. The * signifies $p \leq 0.05$, ** signifies $p \leq 0.01$, *** signifies $p \leq 0.001$, and ns signifies $p \geq 0.05$.

Average Motif		pTi	aFN	iKTN	iRhK	Au	AuKTN
pTi	Control		ns	ns	ns	ns	ns
	alpha4 Beta1		***	***	ns	ns	***
	alpha2b Beta3		***	***	***	ns	ns
aFN	Control		ns	ns	ns	ns	ns
	alpha4 Beta1		ns	***	***	***	ns
	alpha2b Beta3		ns	ns	***	***	***
iKTN	Control		ns	ns	ns	ns	ns
	alpha4 Beta1		***	***	ns	***	ns
	alpha2b Beta3		***	***	***	***	***
	alpha4 Beta1	ns	ns	***	ns	***	
	alpha2b Beta3	***	ns	ns	ns	ns	
iRhK	Control	ns	ns	ns	ns	ns	
	alpha4 Beta1	ns	***	ns	ns	***	
	alpha2b Beta3	***	ns	ns	ns	ns	
Au	Control	ns	ns	ns	ns	ns	
	alpha4 Beta1	***	ns	ns	ns	***	
	alpha2b Beta3	ns	ns	ns	ns	ns	

**Chapter 4. Application of Fluid Shear Stress on Skin Cells to
Characterize Cellular Attachment on Keratin
Nanomaterial Substrates**

Alexis Trent¹, Mark E. Van Dyke^{2}*

1. Department of Materials Science and Engineering, Virginia Tech, Blacksburg, VA 24060

2. Department of Biomedical Engineering and Mechanics, Virginia Tech, Blacksburg, VA

24060

(Manuscript in Preparation)

4.1 Abstract

Percutaneous osseointegrated prosthetics (POP) aim to transform the way in which prosthetic limbs are attached to amputees, potentially providing them with enhanced gait, osseoperception, and quality of life compared to socket-interface devices. Although, POPs aid in increased mobility, they experience failure attributed to instability of the skin-titanium interface. Avulsion or mechanical tearing can occur when loading is applied and skin tears away from the implant, increasing the risk for opportunistic infection. Various coating and surface modifications have been explored to increase the mechanical stability of the cell-substrate interface. *In vitro* experiments have shown keratin nanomaterials, formed as a coating on titanium surfaces, can improve cellular adhesion, which may lead to a more stable skin-implant interface, similar to the human fingernail. Shear stress has previously been used to assess mechanical integrity of cellular integrin-mediated attachment to substrates in *in vitro* experiments and may be predictive of *in vivo* behavior. In the present study, dermal fibroblast and HaCaT cells (keratinocytes) were investigated for morphological changes and the presence focal adhesion formation and maturation under shear stress conditions, in an effort to simulate the loading forces of a POP at the skin-implant interface. Keratin protein upregulation in HaCaT cells was evaluated to discern effects of shear on terminal differentiation and keratinocyte activation. Our study provides quantitative results for cell attachment to keratin nanomaterials, which can advance the development of keratin nanomaterials as a potential biomimetic substrate for POP applications.

Keywords: Keratin, percutaneous, biomimetic, coating, biomaterial interface, nanomaterial, shear, cell strength, medical device

4.2 Introduction

The mechanical stability of interfaces between implantable prosthetics and surrounding tissue is crucial for a successfully functioning medical device. Investigations for creating a mechanically and biologically stable interaction between cells and the implant surface, largely by surface treatments and coatings, has been at the forefront of development for this type of medical device. Biocompatible characteristics are a primary component of implant surface design criteria, and in cases where the bulk material may not possess the requisite biocompatibility, satisfactory performance may be obtained via the use of a coating. After a material has been identified as a potentially viable coating, other characteristics need careful examination. Mechanical interactions between cells and substrates play a role in cell signaling and adhesion properties, as well as wound healing responses in the short-term and long-term tissue remodeling and stability¹. Mechanotransduction, the process of mechanical forces applied to a cell being turned into biochemical signals within a cell, should be considered as part of the medical device design process^{2,3}. The main cellular component in mechanotransduction is the focal adhesion, which is a physical attachment of the cell to its surrounding environment, mediated by a class of transmembrane receptors known as integrins. Cell adhesion strength is an important factor to characterize the integrin-mediated attachment between cells and substrates that can assist in validation of a biomaterial's interfacial properties and can be predictive of a surface coating's in vivo performance.

Amputees utilizing socket based prosthetics can experience soreness, pressure ulcers, and load-related pain^{4,5}. Percutaneous osseointegrated prosthetics (POPs) provide improved gait and quality of life for patients⁶. Although POPs are advantageous, they suffer from failure modes that include mechanical tearing of the skin from the implant at the interface, which creates damaged

tissue and a potential route for infection⁷. Patients possessing below the knee POPs have heightened sensitivity on the anterior side of skin-POP toward irritation because there is limited subcutaneous tissue. The thin layer of skin that is present undergoes high-stress gradients and possess a lower stress threshold, causing avulsion and mechanical failure of the skin-POP interface^{8,9}. Investigation of the skin-POP interface has been analyzed through finite element analysis applied to both the bone and skin¹⁰⁻¹², but has not been modeled on a cellular level or with the addition of a coating designed to facilitate integrin-mediated cell adhesion. Providing an *in vitro*, cellular-level analysis of substrate adhesion could provide insight on the suitability of experimental coatings for POP devices.

Various extracellular matrix (ECM) proteins (e.g. fibronectin¹³⁻¹⁵, collagen¹⁶⁻¹⁸, laminin¹⁹) have been implemented to create a biocompatible surface for POP and other medical devices. Keratin has recently been investigated as a coating for percutaneous devices due to extensive research with coatings^{20,21}, hydrogels^{22,23}, and recombinant keratin²⁴ for applications ranging from hemostasis²⁵ to peripheral nerve repair^{26,27}. Hair keratin possesses the leucine-aspartic acid-valine (LDV) amino acid motif, which is postulated to be the primary ligand for integrin-mediated cell attachment. Although shear stress on keratin substrates has been investigated with Schwann cells²⁸, the mechanical integrity of cellular attachment, morphology, and intermediate filament expression of skin-related cells on keratin nanomaterials (KNs) has yet to be examined. The use of keratin, as opposed to other biomolecular coatings, is justified, particularly used for their percutaneous portion of POP devices, because the same keratins that make up the human fingernail are found in human hair keratins. Keratin biomaterials derived from human hair fibers may provide a biomimetic coating that would offer a stable interface with the skin, similar to the human skin-fingernail interface.

To test the mechanical strength of cell-substrate interactions, various modalities have been examined. Single cell analysis with magnetic twisting cytometry (MTC)^{29,30}, mechanical tweezers²⁹, atomic force microscopy (AFM)³¹, and optical tweezers³² have allowed for examination of integrin and other transmembrane receptor's adhesion strength, elastic properties, and observations of deformation. Applying fluid shear stress is another method used to observe attachment for cell monolayers. Hydrodynamic shear between parallel plates^{28,33,34}, rotating disc³⁵, radial flow³⁶ and a cone and plate³⁷ have been used successfully. Shear stress from blood flow in arteries can range from 2-20 dynes/cm², and is therefore considered in many studies to be within a normal physiologic range. When this range is applied to endothelial cells, it induces cell alignment, activation of ion channels, and reorganization of internal cytoskeletal³⁷. Fluid shear stress has been commonly used to assess cell attachment in endothelial cells, but other cells such as osteoblasts have been tested to determine the influence of shear stress on adhesion and cell spreading³⁸. In this study, we used fluid shear stress to examine adhesion of skin cell monolayers' to underlying keratin nanomaterial (KN) substrates and to provide information about the biomimetic characteristics of the coatings within the context of a percutaneous implant application.

4.3 Methods

4.3.1 Keratin Extraction

KN were extracted using a proprietary process³⁹. To summarize, human hair fibers were treated with either peracetic acid (keratose or KOS) or thioglycolate (keratine or KTN) to disrupt disulfide bonds. The cortical proteins were extracted using 100mM Tris base (2-amino-2-(hydroxymethyl)-1,3-propanediol) buffer and solids removed by centrifugation and filtration. The clarified solutions were further processed via tangential flow filtration (TFF) against a buffer solution containing 100mM/10mM disodium phosphate/NaCl. Multiple wash cycles in the TFF

system were used to remove low molecular weight peptides and processing chemicals. Immediately following the washes, the solutions were concentrated and freeze-dried to yield a dry powder of either KOS or KTN.

4.3.2 *Silane Coupling and Protein Deposition*

Microscope slides with a 5 nm titanium coating were purchased from Deposition Research Laboratory Incorporated (St. Charles, Missouri, USA). Slides were immersed in various silane solutions such as 10% 3-Isocyanatopropyltriethoxysilane (I;ICPTES; Acros Organics, Geel, Belgium) in 100% ethanol, 5% Glycidoxypropyltrimethoxysilane (g;GPTES; Acros Organics, Geel, Belgium) in 95% ethanol, or 5% 3-Aminopropyltriethoxysilane (a;APTES; TCI America, Portland, OR, USA) in 95% ethanol while being shaken gently for three hours at room temperature (RT). After the shaking period, slides were rinsed three times with 100% ethanol, followed by a rinse of MilliQ water three times, then placed in an oven for 30 minutes at 110° C. Silanized slides were then incubated in 1% KTN in sodium phosphate buffer at pH 7.4, 1% KOS in sodium phosphate buffer at pH 7.4, or approximately 1 mg/mL recombinant human keratin (rhK; dimers of keratin K31 andK81; provided by Dr. Tijana Grove, Virginia Tech Department of Chemistry) in water overnight at RT, or 5 μ g/cm² of human fibronectin (Corning, Corning, NY, USA) for 1 hour at RT. After protein incubation, slides were rinse three times with MilliQ water and left to air dry. All slides were exposed to 1 hour of ultraviolet light as a sterilization method.

4.3.3 *Cell culture*

HaCaT (Catalog #T0020001; AddexBio Technologies; San Diego, CA, USA) cells were cultured with Dulbecco's Modified Eagle Medium (DMEM) including 1% penicillin-streptomycin (P/S) and 10% fetal bovine serum (FBS) and used at passages 12-18. Roswell Park Memorial Institute medium-1640 (RPMI) with 10% FBS and 1% P/S was used for neonatal fibroblast cells

(PCS-201-010; ATCC; Manassas, VA, USA). Subculturing occurred every three days at a 1:3 dilution for both cell types. All cells were incubated at 5% CO₂ and 37°C.

4.3.4 *Shear Assay and Focal Adhesion Immunocytochemistry*

HaCaT and fibroblast cells were separately seeded at 10,000 cell/cm² onto the slides, but were initially confined within an 800µL droplet for the first three hours to facilitate attachment within a region of interest, then an appropriate amount cell media was added to cover the entire slide. To create various degrees of cell monolayers, incubation periods of 6 hours, 24 hours, and 72 hours, were used; media was not changed within this incubation period. A GlycoTech (GlycoTech, Gaithersburg, MD, USA) rectangular flow chamber shear device with a 1cm flow width and 0.0254cm thickness was used. Incubated cells underwent a shear stress of 10 dynes/cm² for 5 minutes with HEPES buffer as described by Boettiger⁴⁰. Immediately after applied shear, slides were fixed with 4% paraformaldehyde (PFA) for 15 minutes, rinsed with PBS and later stained for focal adhesions.

Focal adhesion complexes (F-actin and vinculin) were identified using the MilliPore FAK 100 kit. After fixation, cells were permeabilized with 0.1% Triton-X, rinsed with Phosphate Buffer Saline (PBS), and blocked with 1% bovine serum albumin (BSA). Staining was performed as described in the manufacturer's FAK kit with specific dilutions and incubation times for Vinculin (1:300; 1 hour), phalloidin (1:150; 1 hour), Alexa Fluor 488(1:300; 1 hour) (ThermoFisher, Waltham, MA, USA), and Dapi (1:1000; 5 minutes). Cells were imaged on a Zeiss Imager A1m microscope. Two images per viable slide were assessed and the quantitative values obtained were averaged.

4.3.5 *Automated Western Blot System (Capillary Electrophoresis Immunoassay)*

The keratin proteins K6, K10, and K16 were identified in HaCaT samples using an automated Western blot (Wes Simple Western Analysis, ProteinSimple, San Jose, USA). Cell lysates were mixed with the 5X Fluorescent solution at a 4:1 dilution. The biotinylated ladder and cell samples were heated at 95°C for 5 minutes. For the keratin proteins listed, the primary antibodies K6, K10, and K16 (Progen Biotechnik, Germany) were diluted 1:25 with the ProteinSimple Antibody Diluent and the secondary antibody, Rabbit anti-Guinea Pig IgG (H+L), HRP (ThermoFisher, Waltham, MA, USA) was diluted 1:100. According to the Wes Plating System protocol, all included solutions were placed in their locations, the plate is placed in the instrument, and automatically run. Band detection and analysis was completed with ProteinSimple's Compass software.

4.3.6 *Statistics*

All data were analyzed with GraphPad Prism 5 (GraphPad Software La Jolla, CA). All data is represented by the mean \pm standard deviation, with replications identified on each graph. A two-way analysis of variance (ANOVA) was used to determine differences between experimental groups with Bonferroni or Tukey's used as a post-hoc test for significance.

4.4 Results and Discussion

4.4.1 *Shear Assay and Focal Adhesion Immunocytochemistry*

4.4.1.1 Fibroblasts

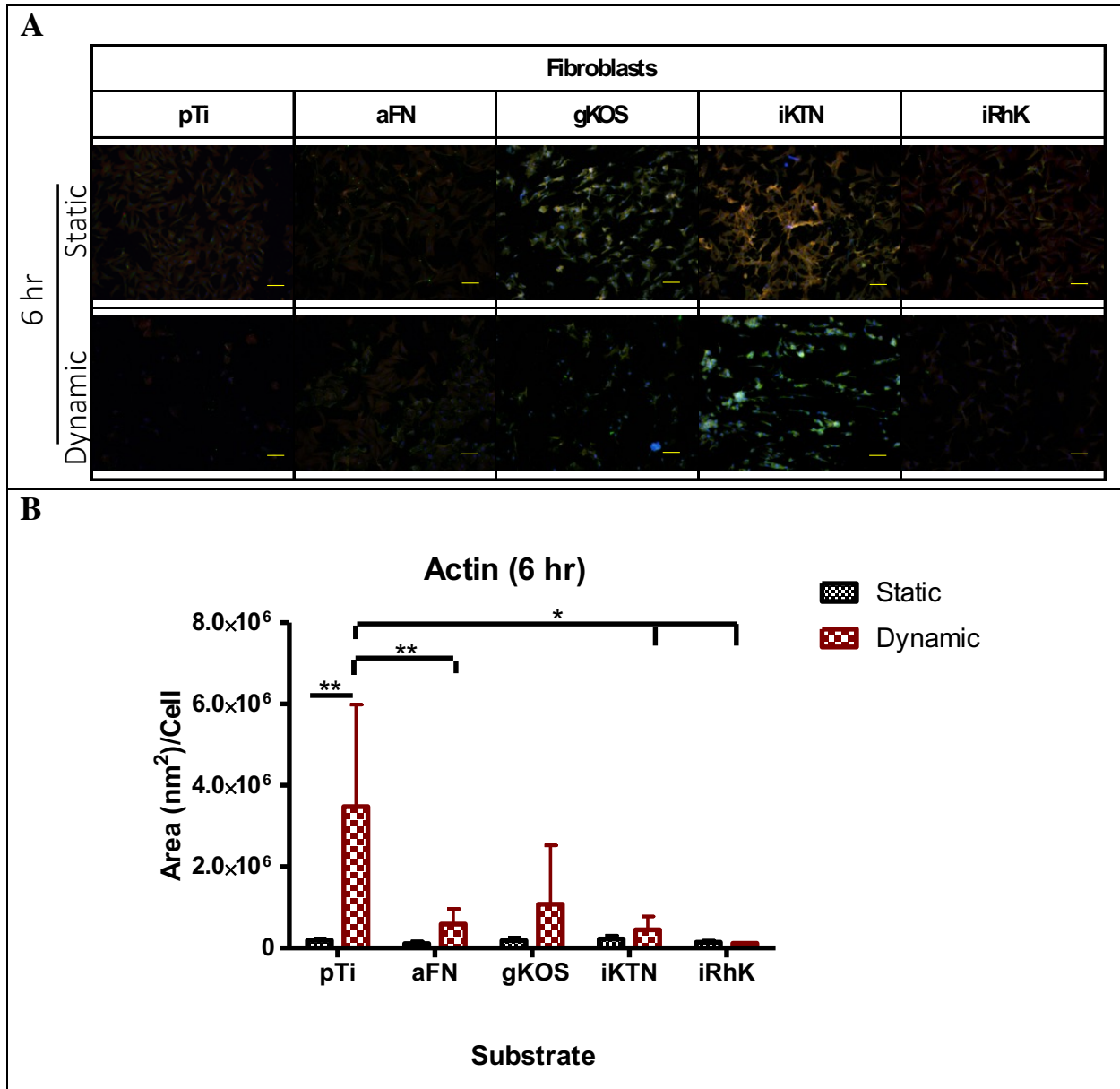


Figure 4.1. Representative images of fibroblasts at 6 hours. A) Static conditions represent 0 dyne/cm², while dynamic represents 10 dyne/cm². Focal adhesions are identified by red (actin), green (vinculin), and blue (nucleus). B) Graph of the area of actin per cell. The significance is shown by * ≤ 0.05 and ** ≤ 0.01 within substrates and between substrates under the same shear conditions. Scale bars represent 50 μ m.

Dermal fibroblasts were seeded onto various substrates and incubated for 6, 24, and 72 hours. The cells were then exposed to shear stress to quantify cell adhesion via the amount of actin expressed by remaining cells. It can be observed in **Figure 4.1**, when fibroblasts are exposed to

shear on pTi, they appear to show a larger amount (and variation) of actin expression. Within pTi, the fibroblasts under shear conditions show a significant difference compared to the static condition, as well as substrates aFN, iKTN, and iRhK in the shear condition. Cells that remain on pTi during shear may express an upregulation of actin due to variations in confluency (i.e. clumps of cells adhered to each other, as well as the substrate). Cell-cell interactions could aid in the resilience of focal adhesions⁴¹ at the time point selected, resulting in an increased cell count and apparent upregulation of expressed actin. This heterogeneity may be the cause of the large standard deviation observed for this experimental group.

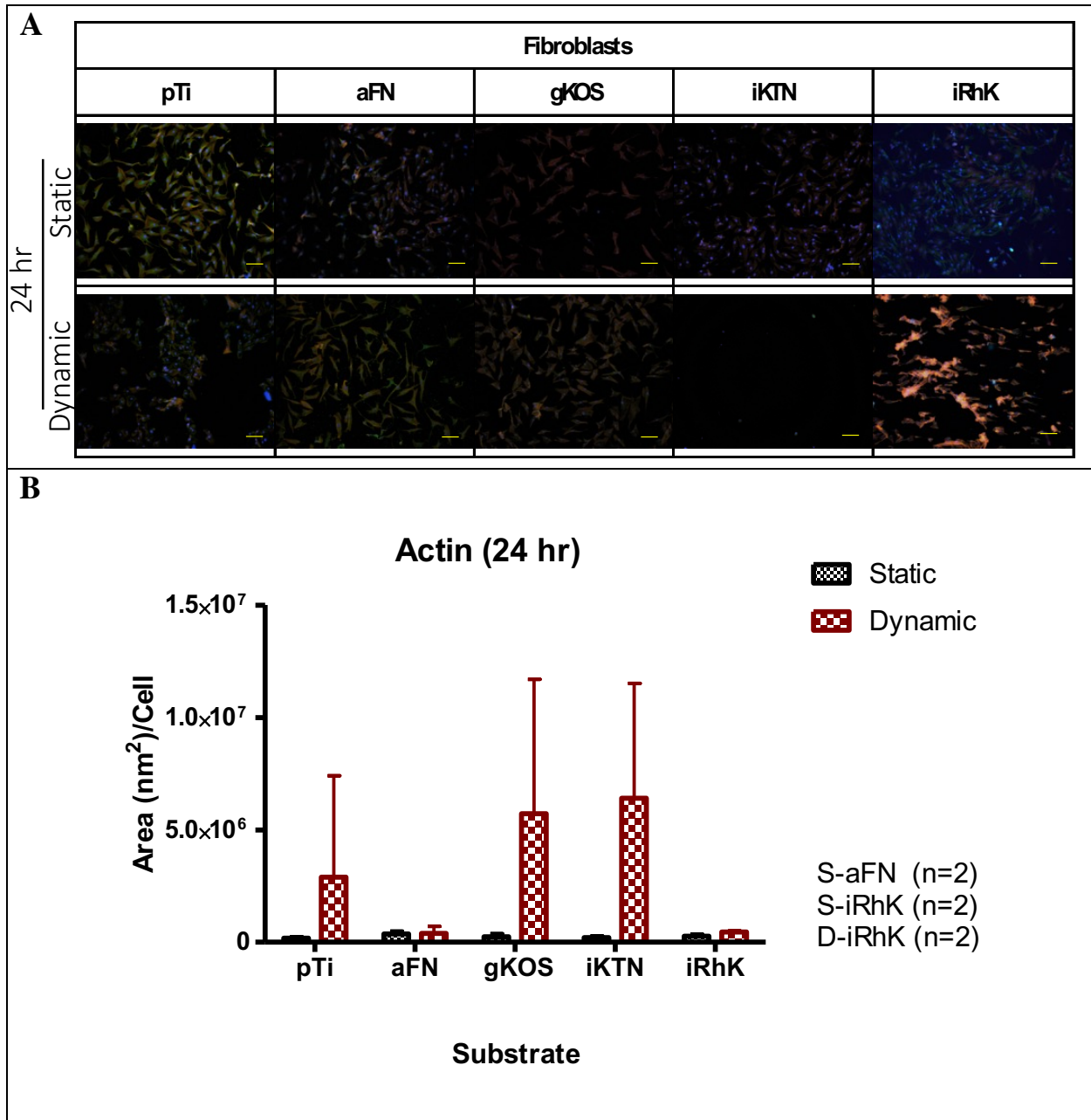


Figure 4.2. Representative images of fibroblasts at 24 hours. A) Static (S) conditions represent 0 dyne/cm², while dynamic (D) represents 10 dynes/cm². Focal adhesions are identified by red (actin), green (vinculin), and blue (nucleus). B) Graph of the area of actin per cell. No significance identified. Scale bars represent 50 μ m.

At the 24 hour time point (**Figure 4.2A**), fibroblasts in the static condition on all substrates have an unvaried standard deviation (**Figure 4.2B**), whereas within each of the substrates pTi, iKTN, and gKOS under dynamic conditions show inconsistent actin expression. While the static

condition appears as expected, it was observed after cells are exposed to shear on iRhK that they formed a slender tear drop shape as if the cells were being dragged by the shear, but still possessed sufficient focal adhesions remain attached. When focal adhesions mature they tend to reside on the perimeter of the cell's contact with a substrate⁴². It is possible this phenomena is occurring on the iRhK substrate. Another observation is the modest increase in actin in the iRhK condition, which may be attributed to cell strengthening through the constant shear exposure period, whereas a continued presence of cells^{43,44} may be the reason for high actin levels on the pTi substrate. iKTN, and gKOS's large standard deviations can be attributed to low cell counts combined with a high expression of actin for cells that remained attached, which also may be related to cell strengthening.

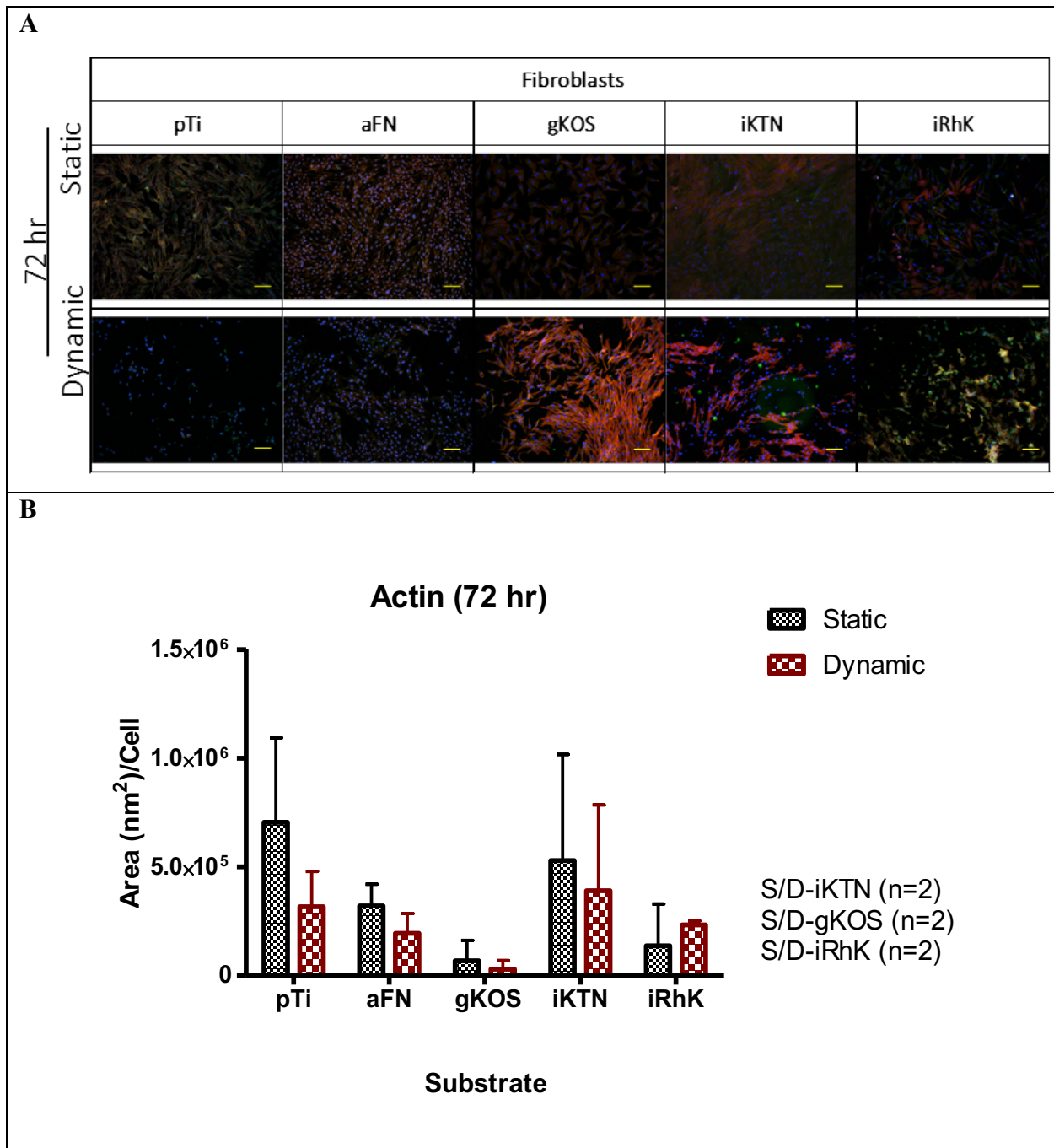


Figure 4.3. Representative images of fibroblasts at 72 hours. A) Static (S) conditions represent 0 dyne/cm², while dynamic (D) represents 10 dynes/cm². Focal adhesions are identified by red (actin), green (vinculin), and blue (nucleus). B) Graph of the area of actin per cell. No significance identified. Scale bars represent 50 μ m.

The 72-hour time point would logically have the most mature focal adhesions, which may also translate to a more homogenized range of actin present (i.e. lower standard deviation within

experimental groups). There were no apparent differences within each experimental group between static and dynamic, most likely due to the longer culture period.

4.4.1.2 HaCaT

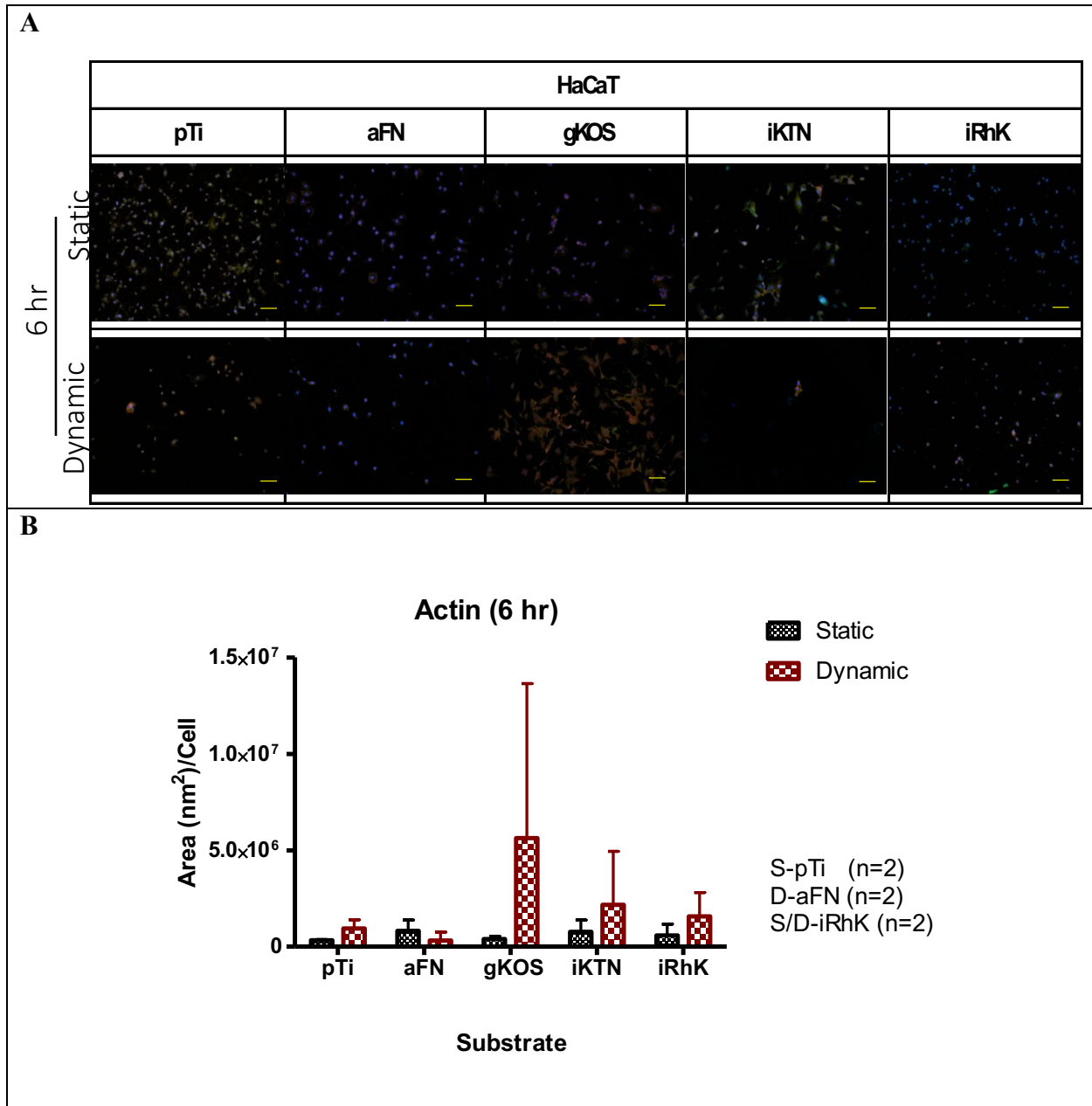


Figure 4.4. Representative images of HaCaT cells at 6 hours. A) Static (S) conditions represent 0 dyne/cm², while dynamic (D) represents 10 dynes/cm². Focal adhesions are identified by red (actin), green (vinculin), and blue (nucleus). B) Graph of the area of actin per cell. No significance identified. Scale bars represent 50 μ m.

With the exception of gKOS, HaCaT were consistent in the actin levels expressed per cell, although the average number of attached cells decreased after the dynamic shear conditions were applied. At the 6 hour time point, nascent adhesion turnover has been completed and cells begin reorganization of actin filaments, creating focal complexes and focal adhesions in a continuum⁴². During this process, cells are able to adapt to mechanical stress by modulating responses to extraneous stimuli. In the cell culture scratch assay with keratinocytes, it was demonstrated mechanical stress caused the upregulated expression of metalloproteinase-9(MMP-9), further stimulating the Rho family proteins⁴⁵, which are involved in the cell-substrate adhesion formation⁴². Although the cell scratch assay study did not directly correlate the mechanical stress to Rho-mediated adhesion, it is plausible, due to the upregulation of Rho through mechanical stimuli this could cause the activation and enhancement of focal adhesions. The inconsistency seen in gKOS may be due to a mixture of adhesion strengthening as well as cell adhesion failure, which varied across multiple samples. Although other substrates have less variation within the dynamic condition data, the expression is either slightly higher or equal to the static condition, further affirming adhesion strengthening is possibly occurring.

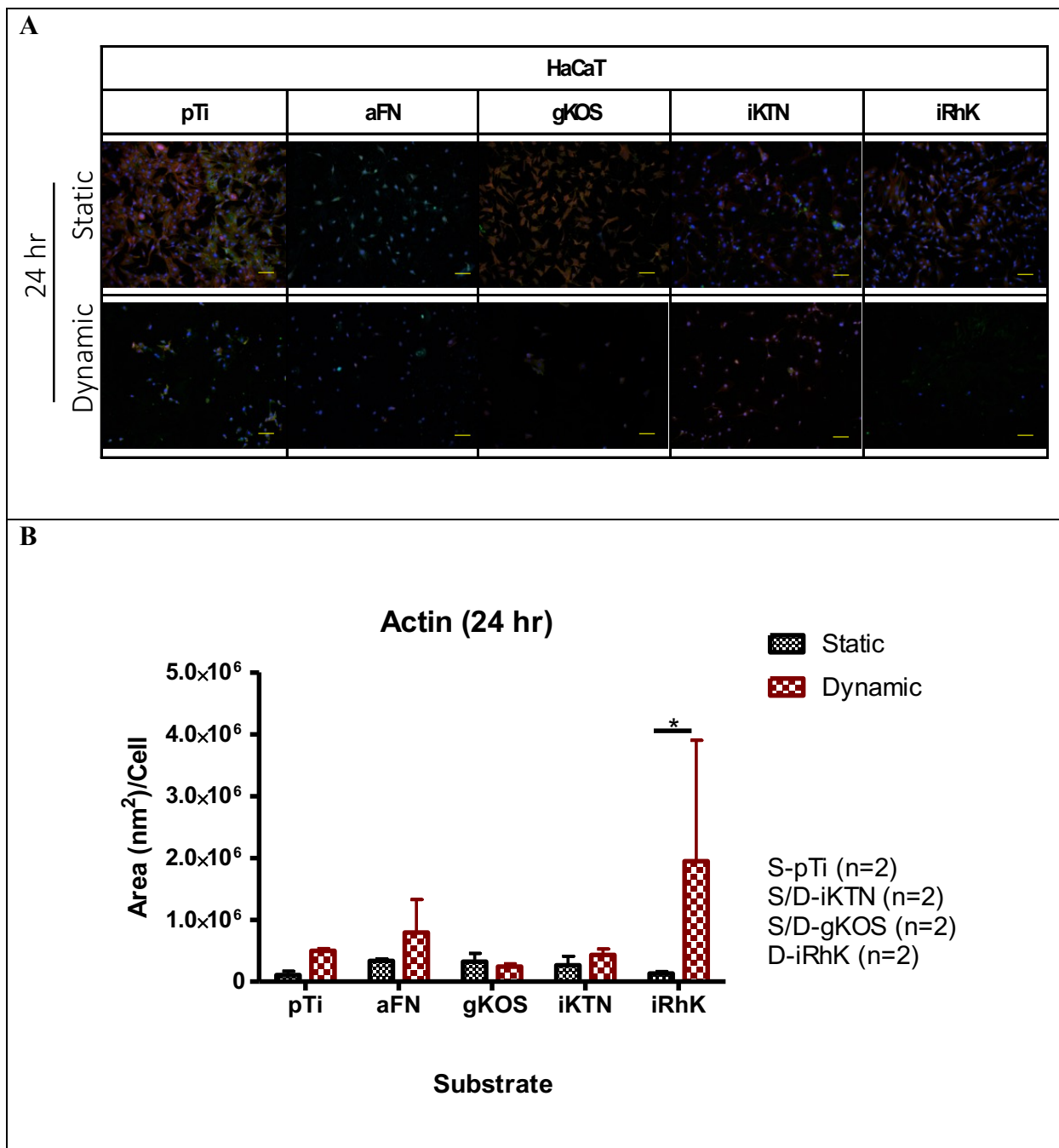


Figure 4.5. Representative images of HaCaT cells at 24 hours. A) Static (S) conditions represent 0 dyne/cm², while dynamic (D) represents 10 dynes/cm². Focal adhesions are identified by red (actin), green (vinculin), and blue (nucleus). B) Graph of the area of actin per cell. The significance is shown by * ≤ 0.05 and ** ≤ 0.01 within substrates and between substrates under the same shear conditions. Scale bars represent 50 μ m.

Figure 4.4 and **Figure 4.5** display expected results with consistent results with the static iRhK condition. An increase in a spread cellular morphology compared to the 6 hour time point is

expected and observed. Here, we see an increase in cell-cell interactions, which leads to intracellular adhesions that can assist the entire cell monolayer to withstand the shear forces. Either the cell-cell adhesion can create additional reinforcement for adhesion or it becomes the dominant adhesion force, greater than cell-substrate mediated adhesion, creating a situation where once failure occurs, large sections of cells become detached.

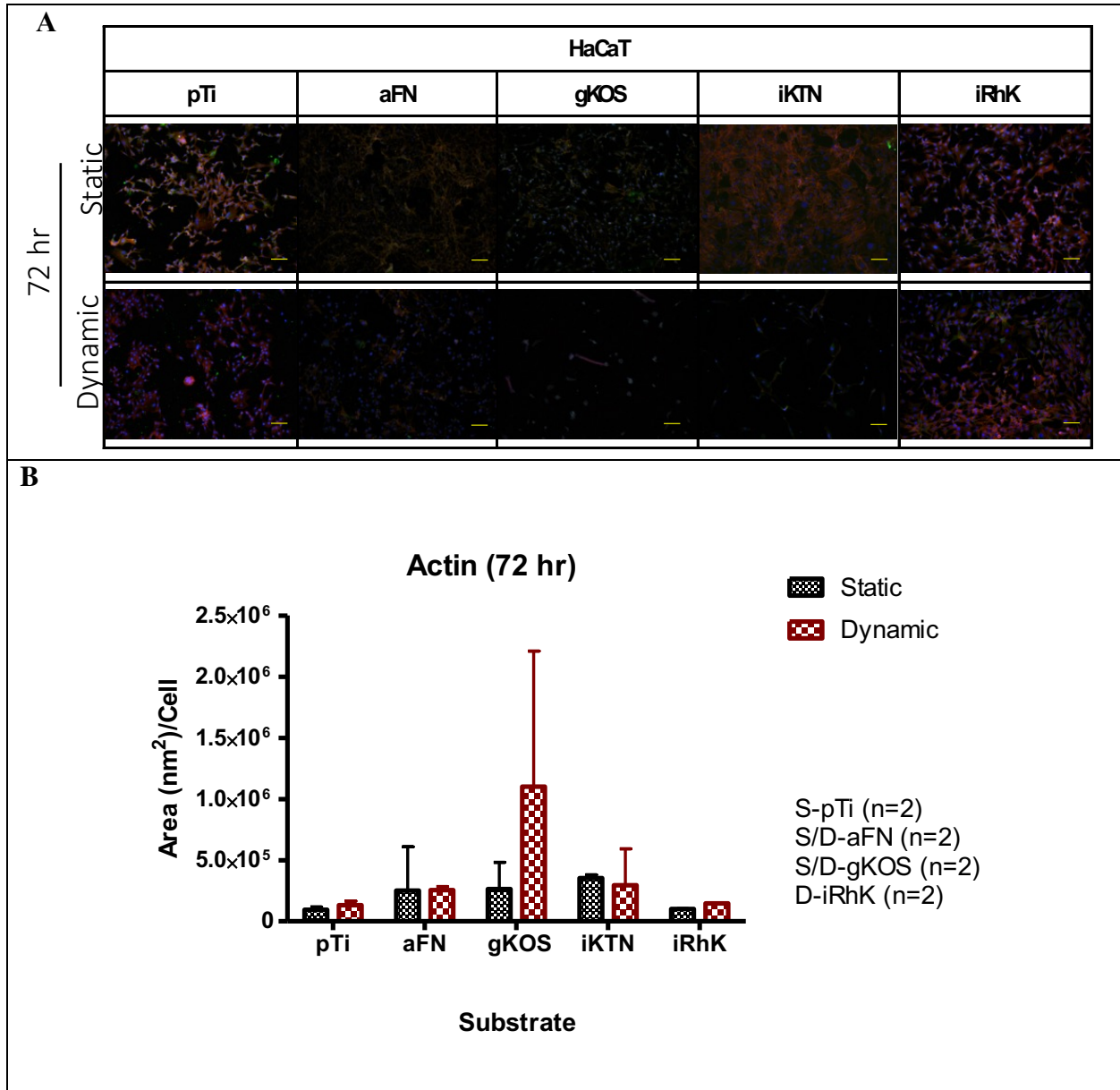


Figure 4.6. Representative images of HaCaT cells at 72 hours. A) Static (S) conditions represent 0 dyne/cm², while dynamic (D) represents 10 dynes/cm². Focal adhesions are identified

by red (actin), green (vinculin), and blue (nucleus). B) Graph of the area of actin per cell. No significance identified. Scale bars represent 50 μm .

Figure 4.6 shows the HaCaT cells were seeded onto KN coatings. Cells were incubated for 72 hours and either exposed to shear (10 dynes/cm²) or kept as a static control (0 dynes/cm²). In comparison to fibroblasts, HaCaT cells showed increased consistency within each timepoint resulting in lower standard deviations, uniformity across substrates, and fewer anomalies when observed microscopically. With the exception of gKOS at 6 hours, iRhK at 24 hours, and gKOS at 72 hours, the expressed actin under dynamic conditions is comparable to their corresponding static condition. It can be hypothesized that either the number of cells and the actin expression has remained unchanged from the static condition, or substrates exposed to shear have fewer cells but are being strengthened by shear, resulting in a higher actin expression per cell. The consistency of the observed data (i.e. low standard deviation) in the HaCaT cells may stem from their keratinocyte origin and the specificity of the KN-cell interaction. That is, this interaction may represent a more biomimetic scenario than, for example, a fibroblast, as it is the keratinocyte that attaches directly to components of the human fingernail. KN may provide biochemical cues to keratinocytes that other cell types may not be capable of processing into altered adhesion behavior.

4.4.2 Modes of Failure

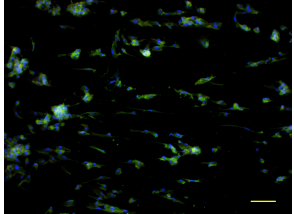
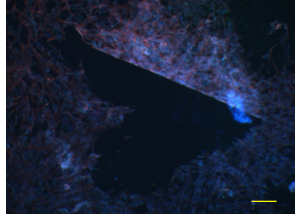
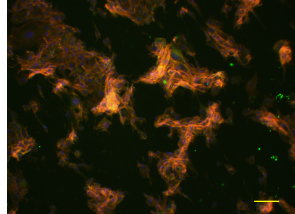
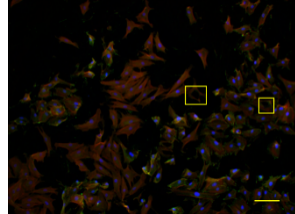
Different Modes of Failure under Dynamic Conditions			
Fibroblasts-iKTN-6 hours	Fibroblast-iRhK-24 hours	HaCaT-aFN-72 hours	Fibroblasts-aFN-6 hours
A) Dragging	B) Sheets	C) Bunching	D) No Nucleus
			

Figure 4.7. Modes of Failure after shear exposure. Modes of Failure under dynamic conditions (10 dynes/cm²) for HaCaT and fibroblast cells. Scale bars represent 50 μ m.

The anomalies in actin expression quantitation were significantly affected by the failure modes experienced by detaching cells. Actin expression in any particular region could be from a small concentration of remaining attached cells while the rest of the sample shows minimal cells. In **Figure 4.7**, four anomalies were observed after are shown following shear (10 dynes/cm² for 5 minutes). In **Figure 4.7A**, cells failed by a dragging method, cells either became slender and elongated or formed crescent-shaped cells. This can be explained by two methods, cells may become aligned with the direction of the shear similar to that observed with endothelial cells³⁴. It has been postulated that cells elongated and align themselves with the shear flow to minimize the drag resistance from the mechanical stimuli⁴⁶. This can cause irregularities in the observed actin expression because the area of expression will be reduced, while the number of cells remains similar to static conditions.

In **Figure 7B**, cells were sheared off via a sheet-like mechanism. This type of failure could be the result of cell-cell adhesions becoming the dominant cell adhesion modality over cell-substrate attachment. Preferentially, cell-cell adhesion could be indicative that the cells are either not integrin-mediated attached to the substrate resulting in a connected sheet of cells being sheared

instead of individual cells. This can affect the area of actin analysis, because it will create large gaps in a confluent cell sheet, resulting in a limited number of actin area. If the extraneous cell sheet is not completely detached, a large actin expression with limited nucleus visibility can be observed. This can create inconsistencies because of the high actin expression for a limited number of nuclei quantified.

A bunching effect can be observed in **Figure 4.7C**, the cells here seem to be affected by detachment, but aggregate together either through strong cell-cell adhesion in conjunction with weak cell-substrate adhesion or cells are detached and continue in flow until they are caught by underlying causing a buildup of cells detached cells on current cell-substrate mediated cells. This can cause a high intensity, low area actin expression with limited to no nucleus present. Lastly, in **Figure 7D**, cells that are adhered and spread are seen, but no nucleus has been detected. This is possibly due to shear exposure on the nucleus in a concentrated area in comparison to the cell body which is spread over a large area. This also affects the actin expression measurements skewing actin expression per cell. In future experiments, using micro-patterned adhesion islands can provide information on the cell-substrate interface⁴⁷, although it would not provide information on cellular monolayers.

4.4.3 Automated Western Blot System (Capillary Electrophoresis Immunoassay)

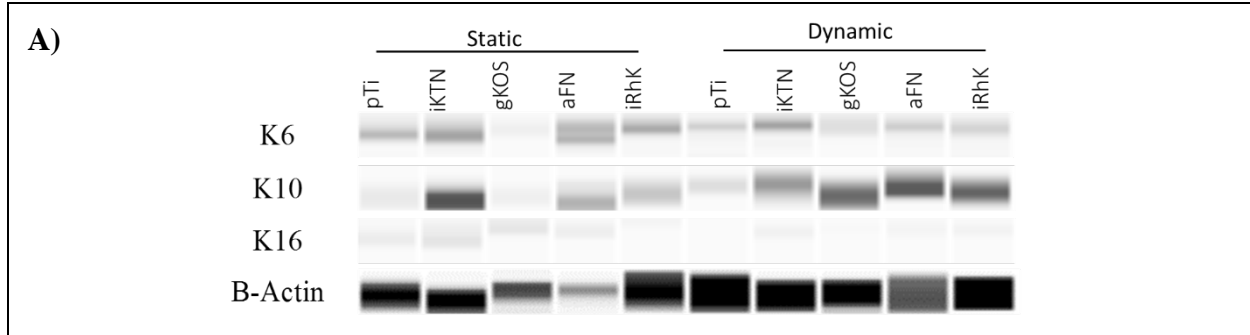


Figure 4.8. Western Blot of K6, K10, K16, and B-Actin. HaCaT cells were seeded for 72 hours and exposed to static (0 dynes/cm²) and dynamic (10 dynes/cm²), cells were probed for K6, K10, K16, and B-Actin using the WesTM Western blot instrument.

In wound healing, K6 and K16 are considered markers of hyperproliferating cells and/or keratinocyte activation as keratin filaments reorganize in cells along the wound edges⁴⁸. Cells progressing toward the suprabasal layer contain a higher expression of K1 and K10, and so these proteins are considered to be indications of terminal differentiation. In one study, mechanical stretching of HaCaT cells was examined⁴⁹. It was discovered that cells seeded onto collagen-coated silicone chambers and stretched had an upregulation of K6, whereas the un-stretched exhibited a normal K10 expression, with no K6 expression.

The mechanism by which mechanical stress translates into keratin filaments is unknown, but it is postulated to have a dependence on nitric oxide synthase⁵⁰. In our study, we observed a low expression level for K16 across all substrates. K6 is only expressed within the suprabasal layers *in vivo* and it has been suggested that keratinocytes displaying K6 are differentiating into the next layer of stratified epithelium⁴⁸. For HaCaT cells seeded on gKOS and iKTN, the keratin expression seems to be mixed, with cells terminally differentiated, but also migrating or reorganizing their keratin filaments⁴⁸. The aFN also has a mixture of K6 and K10 positive cells, which may be related to the role it plays in the fibronectin-rich eschar present in normal wound healing.

Interestingly, HaCaT cells on the iRhK substrate have a mixture of K6 and K10 of relatively equal amounts. A possible explanation maybe the stiffness or roughness of the underlying titanium substrate. Tissue culture (3-5Gpa), glass (50-90GPa), and titanium alloys (105-120GPa) have various stiffnesses⁵¹. Having HaCaT cells on the stiff substrate for 72 hours may cause expression of K6 cells under static conditions. In one study, HaCaT cells seeded on substrates with the stiffness of 16kPa (similar to skin) and polydimethylsiloxane (PDMS) with a 200 kPa stiffness showed wider spreading on the stiffer stubstrate⁵². Single cell keratinocytes themselves have been observed to have a stiffness between 124 kPa to 240kPa⁵³. It is possible that cells might react favorably to substrates with a stiffness closer to that or normal skin. Cells seeded on pTi express majority of, with limited expression of K10 and K16, which suggests these cells are in a continual migratory state. Although K6 is a primary marker of migratory keratinocytes, it is also expressed in the palms of the hand and soles of the feet, so it is plausible that the expression is due to the heighten mechanical loading to which these cells were exposed⁴⁹. From this study, it was observed that cells possess the ability to maintain focal adhesions after exposure to dynamic conditions, but the cells show inconsistencies in adherence after shear. For further observation, single cell analysis might provide more detailed information about the cell-substrate bond strength without the influence of cell-cell adhesion.

4.5 Conclusions

The response of cells seeded onto substrates, including KN coatings, was observed under fluid shear stress. The data suggest that a coating made from recombinant keratin dimers, comprised of keratins K31 and K81, may be suitable for fibroblast and keratinocyte cell adhesion. We speculate that this may be suggestive of improve adhesion between implants coated with this material and skin and that this system represents a biomimetic technology that emulates the skin-

fingernail interface. We postulate that the observed upregulation of K6 could be influenced by the 72-hour incubation time on a stiff substrate, resulting in unexpected expression in the static condition. Identifying the strength by which skin cells adhere to KN will provide insights into the development of future engineered coatings for medical device applications, particularly implants that are required to pass through the skin and maintain a stable skin-implant interface for extended periods.

4.6 Acknowledgements

The authors would like to thank the following funding sources: Department of Defense Congressionally Directed Medical Research Programs (CDMRP), grant number W81XWH-15-1-0343; and Virginia Tech-Initiative for Maximizing Student Development (IMSD), grant number R25GM072767-10. We thank the undergraduate Kyle Brown for assisting on this project.

4.7 References

1. Wang, N. Mechanotransduction at a distance: mechanically coupling the extracellular matrix with the nucleus. at <[http://biology.hunter.cuny.edu/cellbio/Feinstein Cell bio 2014/Melendez-Vasquez Lectures/Reviews/MechanicalCoupling.pdf](http://biology.hunter.cuny.edu/cellbio/Feinstein%20Cell%20bio%202014/Melendez-Vasquez%20Lectures/Reviews/MechanicalCoupling.pdf)>
2. Wang, N., Hu, S. & Butler, J. P. in *Methods in cell biology* (eds. Yu-Li, W. & Dennis, E. D.) **Volume 83**, 179–198 (Academic Press, 2007).
3. Jaalouk, D. E. & Lammerding, J. Mechanotransduction gone awry. *Nat. Rev. Mol. Cell Biol.* **10**, 63–73 (2009).
4. Dudek, N. L., Marks, M. B., Marshall, S. C. & Chardon, J. P. Dermatologic conditions associated with use of a lower-extremity prosthesis. *Arch. Phys. Med. Rehabil.* **86**, 659–663 (2005).
5. Mak, A. F. T., Zhang, M. & Boone, D. A. State-of-the-art research in lower-limb prosthetic biomechanics-socket interface. *J Rehabil Res Dev* **38**, 161–173 (2001).
6. Farrell, B. J., Prilutsky, B. I., Kistenberg, R. S., Dalton, J. F. & Pitkin, M. An animal model to evaluate skin-implant-bone integration and gait with a prosthesis directly attached to the residual limb. *Clin. Biomech.* **29**, 336–349 (2014).
7. von Recum, A. F. Applications and failure modes of percutaneous devices: a review. *J. Biomed. Mater. Res.* **18**, 323–336 (1984).
8. Sanders, J. E. & Daly, C. H. Normal and shear stresses on a residual limb in a prosthetic socket during ambulation: comparison of finite element results with experimental measurements. *J. Rehabil. Res. Dev.* **30**, 191–204 (1993).
9. Sanders, J. E., Goldstein, B. S. & Leotta, D. F. Skin response to mechanical stress: adaptation rather than breakdown--a review of the literature. *J. Rehabil. Res. Dev.* **32**, 214–26 (1995).
10. Yerneni, S., Dhaher, Y. & Kuiken, T. A. A computational model for stress reduction at the skin-implant interface of osseointegrated prostheses. *J. Biomed. Mater. Res. Part A* **100A**, 911–917 (2012).
11. Sanders, J. E., Daly, C. H. & Burgess, E. M. Interface shear stresses during ambulation with a below-knee prosthetic limb. *J. Rehabil. Res. Dev.* **29**, 1–8 (1992).
12. Stenlund, P. *et al.* Effect of load on the bone around bone-anchored amputation prostheses. *J. Orthop. Res.* **35**, 1113–1122 (2017).
13. Ku, Y., Chung, C., Biomaterials, J. J.- & 2005, undefined. The effect of the surface modification of titanium using a recombinant fragment of fibronectin and vitronectin on cell behavior. *Elsevier* at <<http://www.sciencedirect.com/science/article/pii/S0142961205001109>>
14. Middleton, C. A., Pendegrass, C. J., Gordon, D., Jacob, J. & Blunn, G. W. Fibronectin silanized titanium alloy: a bioinductive and durable coating to enhance fibroblast attachment in vitro. *J. Biomed. Mater. Res. Part A* **83**, 1032–1038 (2007).
15. Keselowsky, B. & Collard, D. Surface chemistry modulates fibronectin conformation and directs integrin binding and specificity to control cell adhesion. *J. Biomed.* (2003). at <<http://onlinelibrary.wiley.com/doi/10.1002/jbm.a.10537/full>>
16. Rammelt, S. *et al.* Coating of titanium implants with type-I collagen. *J. Orthop. Res.* **22**, 1025–1034 (2004).
17. Nagai, M. In vitro Study of Collagen Coating of Titanium Implants for Initial Cell

- Attachment. *Dent. Mater. J.* **21**, 250–260 (2002).
18. Ma, L. *et al.* Collagen/chitosan porous scaffolds with improved biostability for skin tissue engineering. *Biomaterials* **24**, 4833–4841 (2003).
 19. Gordon, D. J., Bhagawati, D. D., Pendegrass, C. J., Middleton, C. A. & Blunn, G. W. Modification of titanium alloy surfaces for percutaneous implants by covalently attaching laminin. *J. Biomed. Mater. Res. Part A* **9999A**, NA-NA (2010).
 20. Sierpinski, P. *et al.* The use of keratin biomaterials derived from human hair for the promotion of rapid regeneration of peripheral nerves. *Biomaterials* **29**, 118–128 (2008).
 21. Fearing, B. & Dyke, M. Van. In vitro response of macrophage polarization to a keratin biomaterial. *Acta Biomater.* (2014). at <http://www.sciencedirect.com/science/article/pii/S1742706114001603>
 22. Pace, L. A. *et al.* A Human Hair Keratin Hydrogel Scaffold Enhances Median Nerve Regeneration in Nonhuman Primates: An Electrophysiological and Histological Study. *Tissue Eng. Part A* 131115063659000 (2013). doi:10.1089/ten.tea.2013.0084
 23. Ledford, B. T. *et al.* Keratose Hydrogels Promote Vascular Smooth Muscle Differentiation from C-kit-Positive Human Cardiac Stem Cells. *Stem Cells Dev.* **26**, 888–900 (2017).
 24. Parker, R. N. *et al.* Homo- and heteropolymer self-assembly of recombinant trichocytic keratins. *Biopolymers* **107**, e23037 (2017).
 25. Burnett, L. R. *et al.* Hemostatic properties and the role of cell receptor recognition in human hair keratin protein hydrogels. *Biomaterials* **34**, 2632–40 (2013).
 26. Hill, P. S. *et al.* Repair of Peripheral Nerve Defects in Rabbits Using Keratin Hydrogel Scaffolds. *Tissue Eng. Part A* **17**, 1499–1505 (2011).
 27. Apel, P. J. *et al.* Peripheral Nerve Regeneration Using a Keratin-Based Scaffold: Long-Term Functional and Histological Outcomes in a Mouse Model. *J. Hand Surg. Am.* **33**, 1541–1547 (2008).
 28. Sierpinski, P. *et al.* The use of keratin biomaterials derived from human hair for the promotion of rapid regeneration of peripheral nerves. *Biomaterials* **29**, 118–128 (2008).
 29. Lele, T. P. *et al.* in *Methods in cell biology* (eds. Yu-Li, W. & Dennis, E. D.) **Volume 83**, 441–472 (Academic Press, 2007).
 30. Tanase, M., Biais, N. & Sheetz, M. in *Methods in cell biology* (eds. Yu-Li, W. & Dennis, E. D.) **Volume 83**, 473–493 (Academic Press, 2007).
 31. Haase, K. & Pelling, A. E. Investigating cell mechanics with atomic force microscopy. *J. R. Soc. Interface* **12**, 20140970 (2015).
 32. Neuman, K. C. & Nagy, A. Single-molecule force spectroscopy: optical tweezers, magnetic tweezers and atomic force microscopy. *Nat. Methods* **5**, 491–505 (2008).
 33. Eldridge, W. J., Sheinfeld, A., Rinehart, M. T. & Wax, A. Imaging deformation of adherent cells due to shear stress using quantitative phase imaging. *Opt. Lett.* **41**, 352 (2016).
 34. Levesque, M. J. & Nerem, R. M. The Elongation and Orientation of Cultured Endothelial Cells in Response to Shear Stress. *J. Biomech. Eng.* **107**, 341 (1985).
 35. García, A. J., Ducheyne, P. & Boettiger, D. Quantification of cell adhesion using a spinning disc device and application to surface-reactive materials. *Biomaterials* **18**, 1091–1098 (1997).
 36. Goldstein, A. S. & DiMilla, P. A. Application of fluid mechanic and kinetic models to

- characterize mammalian cell detachment in a radial-flow chamber. *Biotechnol. Bioeng.* **55**, 616–629 (1997).
37. DePaola, N., Gimbrone Jr, M. A., Davies, P. F. & Forbes Dewey Jr, C. Vascular Endothelium Responds to Fluid Shear Stress Gradients. at <<http://atvb.ahajournals.org/content/atvbaha/12/11/1254.full.pdf>>
 38. You, L., Temiyasathit, S., Coyer, S. R., García, A. J. & Jacobs, C. R. Bone cells grown on micropatterned surfaces are more sensitive to fluid shear stress. *Cell. Mol. Bioeng.* **1**, 182–188 (2008).
 39. Van Dyke, M. & Rahmany, M. Keratin Nanomaterials and Methods of Production. (2015). at <<https://www.google.com/patents/US20170051027>>
 40. Boettiger, D. in 1–25 (2007). doi:10.1016/S0076-6879(07)26001-X
 41. Edelman, G. M. Cell adhesion molecules. *Science* **219**, 450–7 (1983).
 42. Parsons, J. T., Horwitz, A. R. & Schwartz, M. A. Cell adhesion: integrating cytoskeletal dynamics and cellular tension. *Nat. Rev. Mol. Cell Biol.* **11**, 633–643 (2010).
 43. Gallant, N. D. & García, A. J. Model of integrin-mediated cell adhesion strengthening. *J. Biomech.* **40**, 1301–1309 (2007).
 44. Michael, K. E. & García, A. J. in *Methods in cell biology* (eds. Yu-Li, W. & Dennis, E. D.) **Volume 83**, 329–346 (Academic Press, 2007).
 45. Bourget, I. *et al.* Cross-Talk Between RhoGTPases and Stress Activated Kinases for Matrix Metalloproteinase-9 Induction in Response to Keratinocytes Injury. *J. Invest. Dermatol.* **121**, 1291–1300 (2003).
 46. White, C. R. & Frangos, J. A. The shear stress of it all: the cell membrane and mechanochemical transduction. *Philos. Trans. R. Soc. Lond. B. Biol. Sci.* **362**, 1459–67 (2007).
 47. Gallant, N. D., Capadona, J. R., Frazier, A. B., Collard, D. M. & García, A. J. Micropatterned Surfaces to Engineer Focal Adhesions for Analysis of Cell Adhesion Strengthening. *Langmuir* **18**, 5579–5584 (2002).
 48. Luo, S. *et al.* Differential keratin expression during epiboly in a wound model of bioengineered skin and in human chronic wounds. *Int. J. Low. Extrem. Wounds* **10**, 122–9 (2011).
 49. Yano, S., Komine, M., Fujimoto, M., Okochi, H. & Tamaki, K. Mechanical Stretching In Vitro Regulates Signal Transduction Pathways and Cellular Proliferation in Human Epidermal Keratinocytes. *J. Invest. Dermatol.* **122**, 783–790 (2004).
 50. Toivola, D. M., Strnad, P., Habtezion, A. & Omary, M. B. Intermediate filaments take the heat as stress proteins. *Trends Cell Biol.* **20**, 79–91 (2010).
 51. Pompe, W., Rödel, G., Weiss, H.-J. (Physicist) & Mertig, M. *Bio-nanomaterials : designing materials inspired by nature*. at <[https://books.google.com/books?id=LRGGzzlefB0C&pg=PT148&lpg=PT148&dq=titanium+stiffness+kPa&source=bl&ots=Dd9uUr0H5r&sig=PROxTXb17IdjBEu4Oy1DJttG2hA&hl=en&sa=X&ved=0ahUKEwik3I2bpMfZAhVnuVkkHVyTD5kQ6AEIVTAE#v=onepage&q=titanium stiffness kPa&f=false](https://books.google.com/books?id=LRGGzzlefB0C&pg=PT148&lpg=PT148&dq=titanium+stiffness+kPa&source=bl&ots=Dd9uUr0H5r&sig=PROxTXb17IdjBEu4Oy1DJttG2hA&hl=en&sa=X&ved=0ahUKEwik3I2bpMfZAhVnuVkkHVyTD5kQ6AEIVTAE#v=onepage&q=titanium%20stiffness%20kPa&f=false)>
 52. Wang, Y., Wang, G., Luo, X., Qiu, J. & Tang, C. Substrate stiffness regulates the proliferation, migration, and differentiation of epidermal cells. *Burns* **38**, 414–420 (2012).
 53. Lulevich, V., Yang, H., Rivkah Isseroff, R. & Liu, G. Single cell mechanics of keratinocyte cells. *Ultramicroscopy* **110**, 1435–1442 (2010).

Chapter 5. Investigation of Keratin Nanomaterials as Coatings for Polymeric Medical Device Applications

Alexis Trent¹, Kyle Brown², Mark E. Van Dyke³

1. Department of Materials Science and Engineering, Virginia Tech, Blacksburg, VA 24060

2. Department of Biochemistry and Department of Nanoscience, Virginia Tech, Blacksburg,
VA 24060

3. Department of Biomedical Engineering and Mechanics, Virginia Tech, Blacksburg, VA
24060

5.1 Abstract

Implantable devices have faced biocompatibility issues that degrade the function of the device. Brain interfacing implants and neural electrodes are devices used to measure or stimulate neural impulses within the central nervous system. Use of these devices have been limited due to biocompatibility issues in the soft tissue immediately adjacent to the implantation site. The foreign body response from host tissue can cause post-surgery complications, including excessive scarring, creating long-term problems for device performance. This is particularly true for electrodes where intimate contact with the tissue relies on close proximity to neural cells, and where even a modest foreign body response can increase these distances with unwanted fibrous tissue and reduce signal strength. Recent attempts to prevent this issue have involved coating the device with polymers such as parylene C to help increase electrical performance stability. Parylene C is useful for device stability because of its low dielectric constant, conformity, uniform thickness and ability to be produced at room temperature, but it is perceived by the body as a foreign substance. The topography of parylene C can also be modified easily. Proteins such as keratin can increase device biocompatibility without negatively affecting the performance, but methods showing robust attachment of keratins to polymers like parylene C are current lacking. In this study, we first modified parylene C-coated substrates with oxygen plasma etching, which allowed for coating through covalent bonds with silane couplings. Using silane-coupling chemistry, KN were attached and the substrates tested for surface roughness and observation of topography. Results showed uniform coatings of KN on a chlorine silane coupling. We confirmed the feasible of a KN coating on a polymeric surface to be further used for biomimetic testing.

5.2 Introduction

All implantable medical devices suffer from some level of foreign body response, which result from a combination of inflammation and encapsulation, and results in scar tissue formation around an implant or varying severity¹. Polymers such as silicone elastomers (e.g. poly(dimethylsiloxane or PDMS), and poly(chloro-p-xylylene) (parylene C) have been used for medical devices and biological applications due to their biocompatibility, chemical and biological inertness, low toxicity, relatively low cost, and variety of adjustable polymer characteristics that suit multiple areas in the body²⁻⁴. For example, PDMS and other polymers have been used in vascular stents⁵, as well as other medical devices. Oxygen plasma has been used to oxidize the surface by removing hydrogen from the polymer chain to create radicals. Although this creates a hydrophilic surface, this is momentary due to the hydrophobicity effect caused by low molecular weight PDMS diffusing to the surface of the bulk material^{2,6}. Surface modification such as silanization has been used on plasma etched PDMS to try to help maintain protein attachment when the application calls for it. The silane coupling is able to attach to the oxygen species and create a covalent bond to ensure a permanent attachment. The functional group of the silane then attaches to amines, carboxyl, and other reactive group in the complementary coating compound, which in some cases may be a protein. Silicone elastomers similar to PDMS are used for continuous glucose monitoring devices^{7,8} and catheters⁹.

The same method of plasma etching and silanization can be used on parylene C, which is an electrically insulating material that has been used to coat neural implants¹⁰⁻¹². Parylene C is a transparent, mechanically strong polymer with a carbon backbone that is impervious to bacterial and fungal growth⁴. It is used to encapsulate electrode arrays for neural implants but suffers from a foreign body response, mediated by glial cells in the central nervous tissue, which results in glial

scarring that inhibits electrical transmission to/from cells out of/into the electrodes. When inserted, the parylene-C coated electrode elicits a response from reactive brain cells that encapsulate the electrode, a process known as gliosis. It is hypothesized this causes a reduction of the neural electrode's intended function¹⁵. Intracortical electrodes are an integral part of acquisition and communication within the brain to stimulate nerves and cause muscle movement for motorized prosthetic limbs¹³. Although neural sensors could provide advanced brain interfacing technology, electrodes suffer from the foreign body response, similar to percutaneous osseointegrated prosthetics¹⁴⁻¹⁶. Using a protein coating to modulate and reduce gliosis may be beneficial and extend the life of neural electrodes *in vivo*. Keratin coatings have been implemented in other medical applications (hemostasis^{17,18}, nerve^{19,20} and bone²¹ regeneration) and could possibly provide a means to reduce the foreign body response to neural electrodes. In this study, we use silane coupling to attach keratin nanomaterials (KNs) to a parylene C coated silicon wafer to create a surface that may be more compatible with neural tissue.

5.3 Methods

5.3.1 Keratin Extraction

A proprietary method was used to extract keratin nanomaterials³⁸. In brief, human hair was treated with either peracetic acid (keratose or KOS) or thioglycolate (kerateine or KTN) to cleave the disulfide bonds present. A buffer solution containing 100mM of 2-amino-2-(hydroxymethyl)-1,3-propanediol was used to extract cortical proteins. The solution was centrifuged and filtered to remove any residual solids, and, using a custom built, recirculating tangential flow filtration system, dimeric keratin complexes (hereafter called “keratin nanomaterials” or KN) were isolated from the crude extract using a 100 kDa low molecular weight cutoff membrane and buffer. After isolation, the TFF system was used to concentrate the KN, which was frozen and lyophilized.

5.3.2 *Protein Deposition*

Silicon wafers (University Wafers, Boston, MA, USA) were coated with parylene C by Specialty Coating Systems (Indianapolis, IN, USA). Parylene C was oxygen plasma etched (PE) in a Harrick Plasma's Plasma Cleaner system (Ithaca, NY, USA) for 2 minutes before they were coated with either 10% 3-Aminopropyltriethoxysilane (a; APTES; TCI America, Portland, OR, USA), 10% 3-Chloropropyltriethoxysilane (c;CPTES; Acros Organics, Geel, Belgium), 5%Glycidoxypropyltrimethoxysilane (g;GPTES; Acros Organics, Geel, Belgium), or 10% 3-Isocyanatopropyltriethoxysilane (I;ICPTES; Acros Organics, Geel, Belgium) dissolved in 100% ethanol. Substrates were coated with silane coupling solutions for three hours at room temperature (RT). They were then rinsed with ethanol followed by water three times and placed into an oven for 30 minutes at 110°C. 1% kerateine (KTN) and 1% keratose (KOS) solutions in 10 mM sodium phosphate at pH 7.4 were then placed over the substrates overnight at room temperature (RT). After protein incubation substrates were rinsed with purified water and air dried.

5.3.3 *Atomic Force Microscope*

Air dried samples were observed on a Veeco BioScope II (Oyster Bay, NY) at RT under tapping mode. Three 2 μ m by 2 μ m fields were analyzed on each substrate using silicon tips (Nanosensors, Switzerland) with force constants between 10 -130 N/m. The surface roughness (RMS) and digitized images were collected and analyzed with the Bruker's Nanoscope software.

5.3.4 *Statistics*

Replicates are identified on graphs for each substrate. GraphPad Prism 5 was used to complete an analysis of variance (ANOVA), and Tukey's post-hoc test was used to determine significant differences in cross-group comparisons. Graphs show mean \pm standard deviation.

5.4 Results and Discussion

Although silicon wafers are considered highly smooth, and parylene C is a conformal coating method, AFM images show apparent roughness (**Figure 5.1**). The various keratin coatings appear to coat the etched parylene C, as evidenced by different features in the AFM images and reduce the roughness compared to bare parylene C (**Figure 5.2**). Some of the keratin surfaces appear “patchy,” which is demonstrated by discontinuities in the AFM images and a higher amount of surface roughness, as well as a larger standard deviation in these measurements. This is particularly true for the gKOS coating, although none of the keratin coatings were statistically different from each other.

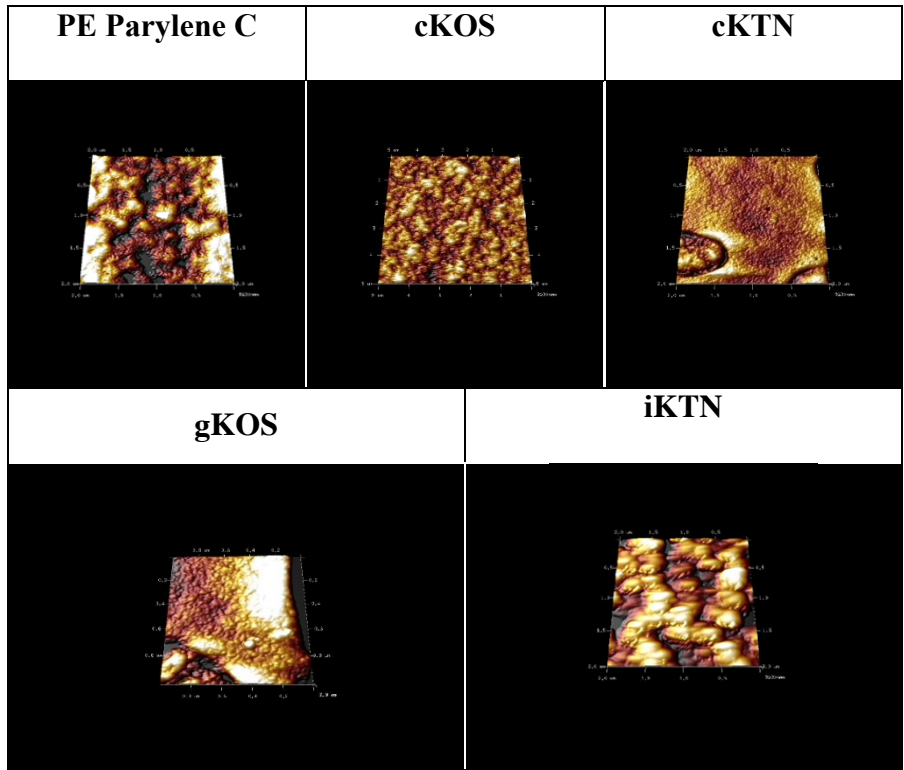


Figure 5.1 The topography of KN on parylene C substrates.

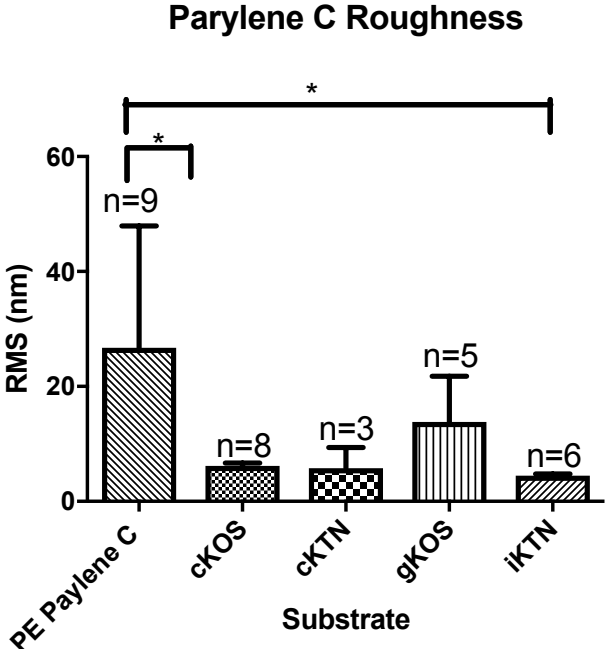


Figure 5.2. Graphical representation of KN RMS

5.5 Conclusion

A KN coating was created onto a model parylene C substrate using a combination of oxygen plasma etching and silane coupling chemistry. The surface appeared to be able to be coated with a variety of silane/keratin combinations, which created apparent uniformity in some cases. Further investigation of the biocompatibility and electrical properties may reveal the ability for these coatings to create intimate contact with neural cells and collect signals with acceptable sensitivity. Other in vitro studies with glial cells may be useful for determining a potential scarring response. Ultimately, animal testing will be necessary to determine if the foreign body response could be mitigated to the level necessary for maintaining device performance, and for how long. A keratin coating system may also be able to be implemented on other polymer substrates, provided they are compatible with the plasma etching/silane coupling processes.

5.6 Acknowledgments

The authors would like to thank the following funding sources: Department of Defense Congressionally Directed Medical Research Programs (CDMRP), grant number W81XWH-15-1-0343; and Virginia Tech-Initiative for Maximizing Student Development (IMSD), grant number R25GM072767-10 to Alexis Trent and Luther Hamlett Undergraduate Research Scholarship to Kyle Brown.

5.7 References

1. Stroncek, J. D. & Reichert, W. M. *Overview of Wound Healing in Different Tissue Types. Indwelling Neural Implants: Strategies for Contending with the In Vivo Environment* (CRC Press/Taylor & Francis, 2008). at <<http://www.ncbi.nlm.nih.gov/pubmed/21204404>>
2. Wu, M.-H. Simple poly(dimethylsiloxane) surface modification to control cell adhesion. *Surf. Interface Anal.* **41**, 11–16 (2009).
3. Pinto, S. *et al.* Poly(dimethyl siloxane) surface modification by low-pressure plasma to improve its characteristics towards biomedical applications. *Colloids Surfaces B Biointerfaces* **81**, 20–26 (2010).
4. Tracy Y. Chang, †, # *et al.* Cell and Protein Compatibility of Parylene-C Surfaces. (2007). doi:10.1021/LA7017049
5. Melchiorri, A. & Hibino, N. Development and assessment of a biodegradable solvent cast polyester fabric small-diameter vascular graft. ... *Res. Part A* (2014). at <<http://onlinelibrary.wiley.com/doi/10.1002/jbm.a.34872/full>>
6. Fritz, J. L. & Owen, M. J. Hydrophobic Recovery of Plasma-Treated Polydimethylsiloxane. *J. Adhes.* **54**, 33–45 (1995).
7. Nichols, S. P., Koh, A., Storm, W. L., Shin, J. H. & Schoenfisch, M. H. Biocompatible Materials for Continuous Glucose Monitoring Devices. doi:10.1021/cr300387j
8. Kros, A. *et al.* Silica-based hybrid materials as biocompatible coatings for glucose sensors. *Sensors Actuators B Chem.* **81**, 68–75 (2001).
9. Helm, R. E., Klausner, J. D., Klemperer, J. D., Flint, L. M. & Huang, E. Accepted but unacceptable: peripheral IV catheter failure. *J. Infus. Nurs.* **38**, 189–203 (2015).
10. Hassler, C., von Metzen, R. P., Ruther, P. & Stieglitz, T. Characterization of parylene C as an encapsulation material for implanted neural prostheses. *J. Biomed. Mater. Res. Part B Appl. Biomater.* **9999B**, NA-NA (2010).
11. Ortiz-Catalan, M., Håkansson, B. & Brånemark, R. An osseointegrated human-machine gateway for long-term sensory feedback and motor control of artificial limbs. *Sci. Transl. Med.* **6**, 257re6-257re6 (2014).
12. Xie, X. *et al.* Long-term reliability of Al₂O₃ and Parylene C bilayer encapsulated Utah electrode array based neural interfaces for chronic implantation. *J. Neural Eng.* **11**, 26016 (2014).
13. Lee, C. *et al.* Drug eluting coating for 3D Parylene sheath electrode. in *2013 6th International IEEE/EMBS Conference on Neural Engineering (NER)* 839–842 (IEEE, 2013). doi:10.1109/NER.2013.6696065
14. Grill, W. M., Norman, S. E. & Bellamkonda, R. V. Implanted Neural Interfaces: Biochallenges and Engineered Solutions. *Annu. Rev. Biomed. Eng.* **11**, 1–24 (2009).
15. Lewitus, D., Smith, K. L., Shain, W. & Kohn, J. Ultrafast resorbing polymers for use as carriers for cortical neural probes. *Acta Biomater.* **7**, 2483–2491 (2011).
16. McConnell, G. C. *et al.* Implanted neural electrodes cause chronic, local inflammation that is correlated with local neurodegeneration. *J. Neural Eng.* **6**, 56003 (2009).
17. Burnett, L. R. *et al.* Hemostatic properties and the role of cell receptor recognition in human hair keratin protein hydrogels. *Biomaterials* **34**, 2632–40 (2013).
18. Rahmany, M. B., Hantgan, R. R. & Van Dyke, M. A mechanistic investigation of the effect of keratin-based hemostatic agents on coagulation. *Biomaterials* **34**, 2492–2500 (2013).

19. Pace, L. A. *et al.* A Human Hair Keratin Hydrogel Scaffold Enhances Median Nerve Regeneration in Nonhuman Primates: An Electrophysiological and Histological Study. *Tissue Eng. Part A* 131115063659000 (2013). doi:10.1089/ten.tea.2013.0084
20. Apel, P. J. *et al.* Peripheral Nerve Regeneration Using a Keratin-Based Scaffold: Long-Term Functional and Histological Outcomes in a Mouse Model. *J. Hand Surg. Am.* **33**, 1541–1547 (2008).
21. de Guzman, R. C. *et al.* Bone regeneration with BMP-2 delivered from keratose scaffolds. *Biomaterials* **34**, 1644–1656 (2013).

Chapter 6. Conclusions, Limitations, and Future Work

Alexis R. Trent

6.1 Overall Project Conclusion

Applying surface modifications to implantable medical devices could help create a cohesive interface between the surrounding soft tissue, and a reduction of the foreign body response. This dissertation explores keratin nanomaterials' ability to create a coating for percutaneous devices with extracted and recombinant keratin proteins. Keratin nanomaterials or "KN" describe a specific dimeric complex of a type I and type II trichocytic keratin that can be obtained by extraction from keratin-containing materials (e.g. hair, wool, feathers) or made recombinantly. Our work demonstrates that KN can be used for percutaneous prosthetics (POPs), and perhaps other implantable device applications where soft tissue interfaces are important for proper function. With the addition of recombinant proteins, KN can easily be modified to improve biological and mechanical characteristics that may aid in translation into clinical studies.

6.2 Characterization of Extracted Keratin Nanomaterials Biomimetic Coating

The first aim of this dissertation was to create an extracted KN biomimetic coating for percutaneous medical devices, specifically POPs. The coating is biomimetic in that it is expected to emulate the skin-fingernail interface, as some of the same keratins found in human fingernail are also found in the hair cortex. Keratin coatings have previously been explored through passive attachment to tissue culture substrates (i.e. polystyrene), but in our study, silane coupling chemistry was used to reinforce KNs' attachment to the underlying titanium surface, which has yet to be studied until now. The results show that extracted KN can form uniform coatings that contain primary structural features that appear to act as ligands for integrin receptors, and that support cell adhesion through such integrins. It was further established that epithelial and connective tissue cells can also adhere to the KN-titanium substrate, an important aspect for POP applications. Enzyme degradation of the KN coating was also explored to assess whether the coating could

withstand the *in vivo* environment. We concluded that extracted KN possesses several important characteristics for a POP device, and are currently testing the extracted form of KN in animal studies.

6.3 Exploration of Recombinant Keratin Nanomaterials Biomimetic Coating

Recombinant keratins may facilitate clinical translation of a KN coating system for POP and other implanted medical devices for two reasons: 1) Recombinant production offers greater control over manufacturing, and 2) modifications at the amino acid level provide recombinant keratins with an additional means of optimization. Extracted hair keratins have been studied in a multitude of applications with some success, but due to the nature of the extraction process, these materials may not be ideal for human medical applications. Production of recombinant keratin eliminates any extraneous human components and allows for additional modifications to the KN at the primary amino acid level. In this work, a comparative study between extracted and recombinant keratin was undertaken. A recombinant keratin coating was created on a silanized titanium surface and compared to the extracted reduced keratin, kerateine. Characterization of both coatings, in the form of a dimeric complex or “keratin nanomaterial” (KN), was performed using a variety of analytical techniques, as well as cell adhesion assays in both static and dynamic conditions. We concluded that both forms of KN could serve as a biomimetic coating for POP devices, but that recombinant keratins have distinct performance-related advantages.

6.4 Importance of Research and Future Work

A surface made from covalently-bonded keratin may serve as an effective biomimetic coating system and enable stable interfaces between POP devices and skin. Moreover, other cell types have shown an affinity for binding to keratin biomaterial surfaces, so the technology may be transferable to other device-soft tissue interfaces. These KN coatings could improve the

functionality of current and future devices such as motorized prosthetics, brain-interfacing electrodes, continuous glucose monitors, and catheters. Cell studies on KN coatings for polymeric interfaces will allow for further progression of polymer devices. Tailoring recombinant keratin with adhesion ligands or other biomolecular components may enhance cell adhesion and strength in percutaneous applications where the mechanical loads are significant.

In vivo studies with extracted KN have been implemented and have shown success in stabilizing the implant-skin interface in a non-load bearing environment. Other studies investigating additional enzyme degradation and thickness of the keratin coating could be conducted to understand the mechanical integrity of the coating's attachment to the underlying titanium. Furthermore, load bearing POP *in vivo* studies will be necessary to advance the coatings on POPs as well as investigate failure mechanisms. Studies complying with the Food and Drug Administration will need to be conducted to move a silane-KN coated substrate toward clinical application. KN coating optimization of polymeric medical device applications could be the next application to consider. In total, this dissertation provided the groundwork for the future of KN coatings and for percutaneous device integration in particular.